VŠB – Technical University of Ostrava
University Study Programmes
Nanotechnology Centre

Optical activity measurement using Mueller matrix ellipsometry

Měření optické aktivity elipsometrií Muellerovy matice

2020

Author: Bc. Daniel Vala
Supervisor: doc. Dr. Mgr. Kamil Postava

VŠB - Technical University of Ostrava
University Study Programmes
CNT - Nanotechnology Centre

Diploma Thesis Assignment

Student:	**Bc. Daniel Vala**
Study Programme:	N3942 Nanotechnology
Study Branch:	3942T001 Nanotechnology
Title:	Optical activity measurement using Mueller matrix ellipsometry Měření optické aktivity elipsometrií Muellerovy matice
The thesis language:	English

Description:

Mueller matrix ellipsometry and polarimetry is broadly used non-destructive highly sensitive technique for optical characterization of samples with general optical anisotropy, gyrotropy, and depolarization.
The main goals of the thesis are:
1. General description of the optical activity in liquids and solid samples including effects of crystal symmetry.
2. Theoretical description of the optical activity influence in Mueller matrices of various samples; separation of this effect using matrix decomposition and fitting by rigorous model.
3. Temperature-dependent measurements and model development of chiral solutions of different concentrations.
4. Mueller matrix ellipsometry analysis of optically active quartz composed waveplates.

References:

R. M. A. Azzam, and N. M. Bashara. Ellipsometry and Polarized Light. New York: sole distributors for the USA and Canada, Elsevier North-Holland, 1977.

F. I. Fedorov. Theory of gyrotropy, Nauka i Technika, Minsk, 1976.

J. J. Gil Pérez and R. Ossikovski, Polarized light and the Mueller matrix approach, Series in Optics and Optoelectronics, CRC Press, 2016.

O. Arteaga, A. Canillas, G. E Jellison Jr., Determination of the components of the gyration tensor of quartz by oblique incidence transmission two-modulator generalized ellipsometry, Appl. Opt. 48, 5307-5317, 2009.

L. Barron, Molecular light scattering and optical activity, 2nd ed. Cambridge University Press, 2004.

A. F. Konstantinova, T. G. Golovina, and K. K. Konstantinov. Manifestation of optical activity in different materials. Cryst. Reports, 59, 447–465, 2014.

Extent and terms of a thesis are specified in directions for its elaboration that are opened to the public on the web sites of the faculty.

Supervisor: **doc. Dr. Mgr. Kamil Postava**

Date of issue: 02.12.2019

Date of submission: 08.05.2020

prof. Ing. Jaromír Pištora, CSc.
Head of Department

Ing. Zdeňka Chmelíková, Ph.D.
Vice-rectress for Study Affairs

P R O H L Á Š E N Í

Prohlašuji, že

- jsem byl(a) seznámen(a) s tím, že na moji diplomovou práci se plně vztahuje zákon č. 121/2000 Sb. – autorský zákon, zejména §35 – užití díla v rámci občanských a náboženských obřadů, v rámci školních představení a užití díla školního (§60 – školní dílo);

- beru na vědomí, že Vysoká škola báňská – Technická univerzita Ostrava (dále jen VŠB – TUO) má právo nevýdělečně ke své vnitřní potřebě diplomovou práci užít (§35 odst. 3);

- souhlasím s tím, že diplomová práce bude archivována v elektronické formě v databázi Ústřední knihovny VŠB – TUO a jeden výtisk bude uložen u vedoucího diplomové práce. Souhlasím s tím, že údaje o diplomové práci budou zveřejněny v informačním systému VŠB-TUO;

- bylo sjednáno, že s VŠB – TUO, v případě zájmu z její strany, uzavřu licenční smlouvu s oprávněním užít dílo v rozsahu §12 odst. 4 autorského zákona;

- bylo sjednáno, že užít své dílo – diplomovou práci nebo poskytnout licenci k jejímu využití mohu jen se souhlasem VŠB – TUO, která je oprávněna v takovém případě ode mne požadovat přiměřený příspěvek na úhradu nákladů, které byly VŠB – TUO na vytvoření díla vynaloženy (až do jejich skutečné výše);

- beru na vědomí, že odevzdáním své diplomové práce souhlasím s jejím zveřejněním podle zákona č. 111/1998Sb., o vysokých školách a o změně a doplnění dalších zákonů (Zákon o vysokých školách) bez ohledu na výsledek její obhajoby.

Místopřísežně prohlašuji, že jsem celou diplomovou práci vypracoval(a) samostatně.

V Ostravě . . . .

podpis (jméno a příjmení studenta)

I hereby declare that this Master's thesis was written by myself. I have quoted all the references I have drawn upon.

In Ostrava, 5. 6. 2020

Bc. Daniel Vala

At this point, I would like to thank all those, who have helped in writing this thesis in any way. The greatest gratitude belongs to my supervisor doc. Dr. Mgr. Kamil Postava for his unwavering patience, warm approach, countless suggestive and his precious time-consuming consultations, without which this work would not be brought to its present form. I thank Ing. Martin Mičica, PhD., for the development of the temperature control system involved in the specific rotatory power measurements. Also, I would like to thank to Prof. Dr. Alisa Fedorovna Konstantinova from Russian Academy of Science for sharing her published articles, which exist in the printed form only.

Last but not least, many and many thanks belongs to my family, friends, colleagues, and especially my beloved girlfriend Nikola ♡ for their patience, all the support and moral help in writing this thesis.

Abstrakt

Tato diplomová práce se zabývá měřeními opticky aktivních materiálů prostřednictvím spektroskopické elipsometrie Muellerovy matice. První část práce je věnována rigoróznímu teoretickému popisu optické aktivity za použití Condonova-Fedorovova přístupu. V práci je diskutován vliv materiálové symetrie na optickou aktivitu. V práci byla dále navržena unikátní metoda měření chirálních roztoků sacharidů užitím elipsometrie Muellerovy matice v spektrálním rozsahu od 193 nm do 1700 nm. Z těchto měření byly s vysokou přesností stanoveny mutarotační konstanty. Za účelem teplotně závislých měření roztoků sacharidů, standartní elipsometr Muellerovy matice byl inovován námi navrženým systémem pro cílené řízení teploty chirálního roztoku. Pro popis optické aktivity křemenných fázových destiček byl odvozen teoretický model Muellerovy matice, který zahrnuje efekt optické aktivity v těchto destičkách.

Klíčová slova: chiralita, elipsometrie Muellerovy matice, mutarotace, optická aktivita, optická aktivita roztoků sacharidů, specifická optická stáčivost, optická aktivita křemene

Abstract

This master thesis is focused on the Mueller matrix spectroscopic ellipsometry measurements of the optically active materials. The first part is devoted to the rigorous theoretical description of the optical activity using Condon-Fedorov approach. The effect of material symmetry on the optical activity is discussed. We propose a novel Mueller matrix ellipsometry method of the saccharide solution optical activity measurement within the spectral range from 193 nm to 1700 nm. The mutarotation rate constants are obtained with high accuracy. We extend the standard Woollam RC2 Mueller matrix ellipsometer using a homemade temperature control system. The theoretical description of the optical activity in quartz waveplate including the model of Mueller matrix is proposed.

Key Words: chirality, Mueller matrix ellipsometry, mutarotation, optical activity, optical activity of saccharide solutions, specific rotatory power, optical activity of quartz

Contents

1 Introduction

Nowdays, the Mueller matrix spectroscopic ellipsometry is a very widespread optical and nondestructive method of the optical characterization of matter [1]. Every material has its own and unique physical and chemical properties, therefore each material interacts with the electromagnetic radiation in a different way. This effect is particularly interesting in the case of the interaction with polarized light [2]. The Mueller matrix ellipsometers analyze the change of the polarized light after the interaction with the particular sample. The measurement technique is fast, very sensitive, and can describe various non-trivial effects such as anisotropy and depolarization [3]. Therefore, Mueller matrix spectroscopic ellipsometry is a very powerful method, how to describe broad variety of the samples, from very simple isotropic thin films [4], through anisotropic crystals [5], or scattering phenomena [6], to complex biological structures [7]. The Mueller matrix ellipsometry and polarimetry is sensitive method enough to determine, if the particular human tissue is cancerous of the lowest grades, or even cancer *in situ* (CIS grade) [8], which is normally not observable until time-consuming and destructive histology analyses are performed [9]. The very high sensitivity of the Mueller matrix ellipsometry therefore enables to study the polarization effects with low optical response. One of these effects is the *optical activity*, which has typically low optical response in particular materials.

It is rather difficult to find the example of the optical activity in the everyday routine of an average man in the World around us. On the other hand, we are very well familiarized with something, what is strongly related with the optical activity phenomenon. The parity. Take your hands as an example. We can fairly distinguish between the left and right hand, as there exists a mirror symmetry between them. Very similar logic applies on the phenomenological description of the optically active molecules. And if we go further, we can apply this logic even on the microscopic scale of the crystalline materials. However, on the microscopic level, those ideas are rather abstract and they become insufficient and misleading. The need of the more rigorous description of this phenomenon is evident. This is very important, because the optical activity has various effects with the impact on the daily life: It is the determining effect in the field of biochemistry. It defines the properties of given molecule and it predicts, if such a molecule is for example biocompatible, harmless or poisonous [10], if it undergo various organic syntheses, etc. The human body is constructed from the variety of complex optically active biomolecules [11]. Optical activity plays an important role in the various naturally occuring crystals and minerals. Also, the optical activity has an important role in the area of artificial man made structures, which gives a possibility of e.g. rising a novel optical polarization elements [12]. The tissue polarimetry of cancer surely also include the effect of the optical activity. However, to fully understand the effect of the optical activity in various complicated materials and samples, it is crucial to understand the effect in the simplier ones.

The goal of this diploma thesis is to bring a new characterization techniques of various optically active media including biisotropic media; to extend the standard techniques of the

Mueller matrix ellipsometry measurements; to model the effect of the optical activity using rigorous physical models; and to bring a new insight into the field of the optically active media of various crystal symmetries.

The organization of the thesis and the contribution of each Chapter is as follows:

In Chapter 2, the basic formalisms (Jones and Mueller) used for the description of the polarized light are derived. The great emphasis is put on the interpretation of the phenomena and observable quantities of the Mueller matrix. In order to do it, the connection between theoretical Mueller algebra and real experiment is offered and discussed.

Chapter 3 is in the frame of an introductory to the optical activity phenomenon. A comprehensive historical overview is given and the effect of the optical activity is described mainly from the chemical perspective. The nomenclature of the optically active chemical compounds is defined, and standard single-wavelength techniques of optical activity measurement are described. Optical activity in the living Nature is discussed. To expound the effect of the optical activity out of the Mueller matrix ellipsometry scope, a few notes on the optical activity in the terahertz (THz) spectral region and optically active metamaterials are given.

Chapter 4 describes the rigorous approach of modelling the optical activity based on the Fedorov covariant method. The method is connected with various material constitutive relations. The symmetries between the Condon-Fedorov and Born-Landau approach is showed. The optical activity is described also in the context of all crystal systems. Using the results from this Chapter are used in the following Chapters involving the experimental measurements.

In Chapter 5, the measurement of optical activity of saccharides solutions is presented. On the contrary to simple chemical spectrometers, which are using monochromatic source only, we propose a novel method, how to efficiently measure the optical activity parameters in the spectral range from 193 nm to 1700 nm using the Woollam RC2 Mueller matrix spectroscopic ellipsometer. The great advantage of our method is the ability to measure the mutarotation effects and the reaction kinetics and to determine the related forward and reverse rate constants with a high precision. We also show the stability of the temperature-dependent measurements using an experimental system developed in our laboratories, which works as an extension of the standard sample holder of the Woollam RC2 Mueller matrix ellipsometer.

Chapter 6 shows the effect of the optical activity in the quartz waveplates. The eigenmodes propagating in the direction parallel and perpendicular to the optic axis are derived. To connect the optical activity of quartz waveplates, related Mueller matrix is derived and the effect of the optical activity is theoretically discussed.

2 Mueller calculus: Basics and Insights

The first part of this Chapter introduces the basic concept of the polarized light, and the basics of the Jones and Mueller calculus. The second part of the Chapter focuses on the deeper interpretation of particular phenomena, which arise from the Mueller algebra. There is an extensive description of various Mueller matrix algebra quantities accros the literature, uncluding Mueller matrix decompositions, differential Mueller algebra, depolarization effects, etc. Despite the fact, that those quantites are often experimentally observable, there is usually not provided any connection with the experimental data in the literature. Therefore, the main intention of this Chapter is to select some of the interesting parts of the Mueller calculus, and offer the connection and discussion with the real experimental data measured by the author of this thesis. We hope, that this will help understanding and interpreting the Mueller matrices.

2.1 Maxwell equations

Following equations represent the Maxwell equations in the differential form [13]:

$$\nabla \cdot \boldsymbol{D} = \rho, \tag{2.1a}$$

$$\nabla \cdot \boldsymbol{B} = 0, \tag{2.1b}$$

$$\nabla \times \boldsymbol{H} = \boldsymbol{j} + \frac{\partial \boldsymbol{D}}{\partial t}, \tag{2.1c}$$

$$\nabla \times \boldsymbol{E} = -\frac{\partial \boldsymbol{B}}{\partial t}, \tag{2.1d}$$

where $\boldsymbol{D}$ is the vector of the electrical displacement, $\boldsymbol{B}$ is the magnetic flux density, ρ is the free charges volume density, $\boldsymbol{j}$ is the current density. The relation between $\boldsymbol{D}$, $\boldsymbol{B}$ and the electric field $\boldsymbol{E}$ and the magnetic field $\boldsymbol{H}$, respectively, is given by the set of equations,

$$\boldsymbol{D} = \varepsilon \boldsymbol{E} = \varepsilon_0 \, \boldsymbol{E} + \boldsymbol{P}, \tag{2.2}$$

$$\boldsymbol{B} = \mu \boldsymbol{H} = \mu_0 \, \boldsymbol{H} + \boldsymbol{M}, \tag{2.3}$$

where the polarization $\boldsymbol{P}$ and the magnetization $\boldsymbol{M}$ volume densities, respectively, and the permitivitty ε_0 and the permeability μ_0 of a free space are introduced [14].

Now, the intention is to derive the wave equation of homogenous, isotropic, linear media with no free charge and without conductivity in order to construct the quantites introducing the polarization properties of the light. With preset constraints, the Maxwell equations (2.1) may

be rewriten in the simplified form:

$$\nabla \cdot \boldsymbol{D} = 0, \tag{2.4a}$$

$$\nabla \cdot \boldsymbol{H} = 0, \tag{2.4b}$$

$$\nabla \times \boldsymbol{H} = \frac{\partial \boldsymbol{D}}{\partial t}, \tag{2.4c}$$

$$\nabla \times \boldsymbol{E} = -\mu \frac{\partial \boldsymbol{H}}{\partial t}. \tag{2.4d}$$

Using the substitution of (2.4d) into (2.4c), $\boldsymbol{H}$ is eliminated. After performing some algebra and with help of basic vector identities, we obtain the wave equation for homogenous, isotropic, linear media without free charge carriers and conductivity [15],

$$\nabla^2 \boldsymbol{E} - \mu\varepsilon \frac{\partial^2 \boldsymbol{E}}{\partial t^2} = 0. \tag{2.5}$$

2.2 Jones calculus

The polarization state of the light is described by a superposition of two electric fields, which are oscillating parallel to the x and y axes. Assuming, that the electromagnetic wave is propagating along the z axis, from the principle of the superposition we have

$$\boldsymbol{E}\,(z,t) = \boldsymbol{E}_x(z,t) + \boldsymbol{E}_y(z,t). \tag{2.6}$$

This equation can be expanded as

$$\boldsymbol{E}\,(z,t) = \{E_{0,x}\,\mathrm{e}^{\mathrm{i}(\omega t - kz + \delta_x)}\}_x + \{E_{0,y}\,\mathrm{e}^{\mathrm{i}(\omega t - kz + \delta_y)}\}_y, \tag{2.7}$$

where $E_{0,x,y}$ are the amplitudes of the wave in the x, y direction, ω is the frequency, t is the time, k is the wavenumber, and $\delta_{x,y}$ are the absolute phases of the wave. Now, we can rewrite this equation into the vector form

$$\boldsymbol{E}\,(z,t) = \begin{bmatrix} E_{0,x}\,\mathrm{e}^{\mathrm{i}(\omega t - kz + \delta_x)} \\ E_{0,y}\,\mathrm{e}^{\mathrm{i}(\omega t - kz + \delta_y)} \end{bmatrix} = \begin{bmatrix} E_{0,x}\,\mathrm{e}^{\mathrm{i}\delta_x}\,\mathrm{e}^{\mathrm{i}(\omega t - kz)} \\ E_{0,y}\,\mathrm{e}^{\mathrm{i}\delta_y}\,\mathrm{e}^{\mathrm{i}(\omega t - kz)} \end{bmatrix}. \tag{2.8}$$

Because the wave frequency is invariant with time, and the polarization state of the wave is space-invariant, the factor $\mathrm{e}^{\mathrm{i}(\omega t - kz)}$ can be supresed. The resulting vector

$$\boldsymbol{J} = \begin{bmatrix} |E_x|\,\mathrm{e}^{\mathrm{i}\delta_x} \\ |E_y|\,\mathrm{e}^{\mathrm{i}\delta_y} \end{bmatrix} = \begin{bmatrix} E_x \\ E_y \end{bmatrix}, \tag{2.9}$$

is called the **Jones vector** [16], and it determines the polarization state of the plane monochromatic wave [2]. Note, that only positive values of $E_{0,x,y}$ were used. The intensity of the wave is

given by the equation

$$I = \boldsymbol{J}^{\dagger}\boldsymbol{J}. \tag{2.10}$$

Every pair of orthogonal Jones vectors is a basis-set of two-dimensional space. Therefore, every linear combination of these vectors forms an element of the space itself. Mathematically speaking, if a pair of the $\boldsymbol{J}$ vectors is orthonormal, it must exists a linear transformation of them, which is called the Jones matrix $\mathbf{J}$,

$$\boldsymbol{J}^{\text{out}} = \mathbf{J}\boldsymbol{J}^{\text{in}}. \tag{2.11}$$

As a simple example, transformation of the Jones vector upon rotation in xy-plane by the angle φ is expressed as follows:

$$\begin{bmatrix} E_{\text{x}+\varphi} \\ E_{\text{y}+\varphi} \end{bmatrix} = \begin{bmatrix} \cos\varphi & \sin\varphi \\ -\sin\varphi & \cos\varphi \end{bmatrix} \begin{bmatrix} E_{\text{x}} \\ E_{\text{y}} \end{bmatrix} \tag{2.12}$$

2.3 Mueller calculus

Altough the Jones calculus is a very effective and elegant mathematical way, how to describe totally polarized states of light and its transformations, it is impossible to use this formalism when one wants to treat with unpolarized light. Beside this extremes of totally polarized and totally unpolarized light, and partially polarized light. In order to do so, we have to implement more complex formalism and define the Stokes[1] vector $\boldsymbol{S}$

$$\boldsymbol{S} = \begin{bmatrix} I_x - I_y \\ I_x + I_y \\ I_{45} - I_{-45} \\ I_{\text{LCP}} - I_{\text{RCP}} \end{bmatrix}, \tag{2.13}$$

where I_x, I_y, $I_{\pm 45}$ denotes the wave intensities along x, y, ± 45 directions, respectively. $I_{\text{LCP/RCP}}$ stands for the intensity of left circular and right circular polarized light, respectively [1].

To find a propper mathematical and physicaly meaningful transformation between input and output Stokes vectors, we have to introduce statistical properties of the light [18]. Let us define the coherence vector $\boldsymbol{C} = \left[\langle E_x E_x^* \rangle, \left\langle E_x E_y^* \right\rangle, \langle E_y E_x^* \rangle, \left\langle E_y E_y^* \right\rangle\right]^{\text{T}}$. The relation between $\boldsymbol{C}$ and $\boldsymbol{S}$ is given below introducing the transformation matrix $\mathbf{A}$,

$$\begin{bmatrix} S_0 \\ S_1 \\ S_2 \\ S_3 \end{bmatrix} = \begin{bmatrix} 1 & 0 & 0 & 1 \\ 1 & 0 & 0 & -1 \\ 0 & 1 & 1 & 0 \\ 0 & -i & i & 0 \end{bmatrix} \begin{bmatrix} \langle E_x E_x^* \rangle \\ \left\langle E_x E_y^* \right\rangle \\ \langle E_y E_x^* \rangle \\ \left\langle E_y E_y^* \right\rangle \end{bmatrix}. \tag{2.14}$$

[1] Contemporary matrix notation is based on the work of George Gabriel Stokes [17].

Now, having the $\boldsymbol{S}$ vector defined statistically in terms of the $\boldsymbol{J}$ vector, it is possible to find a direct transformation between input and output Stokes vectors using the 4×4 coherence matrix $\mathbf{F}$:

$$\boldsymbol{C}^{\text{out}} = \mathbf{F}\boldsymbol{C} = \langle \mathbf{J} \otimes \mathbf{J}^* \rangle \, \boldsymbol{C}^{\text{in}}, \tag{2.15}$$

where the symbol $\otimes$ stands for the Cronecker product. Substituting into (2.14), we get

$$\boldsymbol{S}^{\text{out}} = \underbrace{\mathbf{A} \, \langle \mathbf{J} \otimes \mathbf{J}^* \rangle \, \mathbf{A}^{-1}}_{\mathbf{M}} \, \boldsymbol{S}^{\text{in}}. \tag{2.16}$$

The transformation matrix $\mathbf{M}$ of the system is called the **Mueller matrix**[2] [19] and contains the most comprehensive description of the polarization properties of the sample including all possible depolarization effects. For absolute clarity, we explicitly show the transformation as follows

$$\boldsymbol{S}^{\text{out}} = \begin{bmatrix} S_0^{\text{out}} \\ S_1^{\text{out}} \\ S_2^{\text{out}} \\ S_3^{\text{out}} \end{bmatrix} = \begin{bmatrix} m_{11} & m_{12} & m_{13} & m_{14} \\ m_{21} & m_{22} & m_{23} & m_{24} \\ m_{31} & m_{32} & m_{33} & m_{34} \\ m_{41} & m_{42} & m_{43} & m_{44} \end{bmatrix} \begin{bmatrix} S_0^{\text{in}} \\ S_1^{\text{in}} \\ S_2^{\text{in}} \\ S_3^{\text{in}} \end{bmatrix} \equiv \mathbf{M}\boldsymbol{S}^{\text{in}}. \tag{2.17}$$

The matrix is usually presented and measured in its normalized form, in which all elements are divided by m_{11}.

2.4 Poincaré sphere

Henri Poincaré proposed, that any polarization state of the light given by the Stokes vector can be represented on a complex-plane, and stereographically projected onto a point on a spherical surface – Poincaré sphere $\mathbb{P}$, see Fig. (2.1). The sphere of the radius S_0 is defined in a space with the basis vectors given by Stokes parameters $S_{1,2,3}$, which are related to latitude (azimuth) φ and to longitude (ellipticity) χ as follows:

$$S_1 = \cos 2\chi \cos 2\varphi, \tag{2.18a}$$

$$S_2 = \cos 2\chi \sin 2\varphi, \tag{2.18b}$$

$$S_3 = \sin 2\chi. \tag{2.18c}$$

Comparing equations (2.18a)–(2.18c) with (2.13) gives us following observations: The equator of the sphere ($\chi = 0$) represents linear polarizations. South and north poles are the only points, which represent totally LCP and RCP light, respectively ($2\chi = 90$). The lower and upper hemispheres (excluding the poles and the equator) stand for the left-handed and right-

[2] For curious readers, a historical revision of Jones-Stokes-Mueller formalism was published in [20].

handed elliptical polarizations, respectively. For totally polarized light, the polarization states are located at the spherical surface given by radius S_0. A depolarization effect affects each axis separately, therefore $\mathbb{P}$ is mapped to any subspace of itself, $\mathbb{E} \subset \mathbb{P} \wedge \min \dim \mathbb{E} = 1$. Subspace $\mathbb{E}$ is generally eliptical surface. Completely unpolarized light is represented by a point at the centre of the coordinate system. Other types of the subspace dimensionality reduction are possible due to various effects, which will be discussed later.

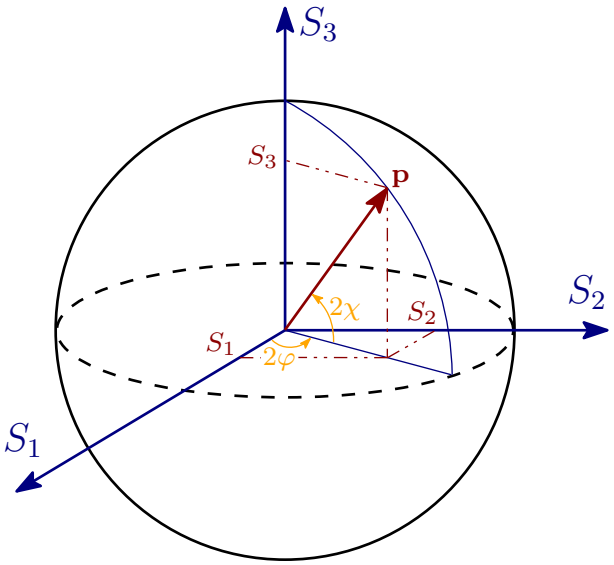

Figure 2.1: Poincaré sphere $\mathbb{P}$. The polarization state of the Stokes vector $\boldsymbol{S}$ is given by a point given by the tip of the vector $\boldsymbol{p}\,(\varphi,\, \chi)$ on the spherical surface.

The quantification of the depolarization effects is given by the degree of polarization [21]

$$S_{\mathrm{p}} = \frac{\sqrt{S_1^2 + S_2^2 + S_2^2}}{S_0}. \tag{2.19}$$

The depolarization effects of a Mueller matrix are given by the depolarization index as [22]

$$P_\Delta = \frac{\sqrt{\sum_{i,j=1}^{4} m_{ij}^2 - m_{11}^2}}{\sqrt{3}\, m_{11}}. \tag{2.20}$$

2.5 Mueller matrix decompositions

Mueller matrix decompositions are one of the suitable tools, which may help in the interpretation of Mueller matrices. The Mueller matrix decompositions can be devided into two cathegories: Sum and product decompositions.

2.5.1 Sum decompositions

The most famous is the Cloude decomposition [23]. Cloud showed, that an arbitrary experimental Mueller matrix can be decomposed into the sum of four Jones-Mueller[3] matrices, each multiplied by the eigenvalue λ_i of corresponding Coherency matrix $\mathbf{C}$,

$$\mathbf{M} = \lambda_1\mathbf{M}_1 + \lambda_2\mathbf{M}_2 + \lambda_3\mathbf{M}_3 + \lambda_4\mathbf{M}_4. \tag{2.21}$$

This decomposition is sometimes called as the *noise filtering*, because it is recommended for slightly depolarizing[4] systems, $P_\Delta \leq 5\,\%$. For these experimental Mueller matrices the decomposition results in

$$\mathbf{M} \approx \lambda_1\mathbf{M}_1, \tag{2.22}$$

while $\lambda_{2,3,4} \approx 0$. They are usually negligibly small, and equal to zero for non-depolarizing systems. Corresponding Mueller matrices are therefore related to the noise or the experimental errors only and can be dropped. The Mueller matrix $\lambda_1\mathbf{M}_1$ is therefore nondepolarizing and contains only relevant response from the sample. For highly depolarizing samples, the eigenvalues are arbitrary ($0 < \lambda_i \leq 1$) and the system more likely remains in its full form as shows Eq. (2.21). Note, that each eigenvalue λ_i must not be negative, otherwise, calculated Mueller matrix is non-physical[5].

Let's suppose an example: We have measured the gold thin film on the glass substrate using Mueller matrix ellipsometry in the reflection configuration. This particular sample was manufactured for the surface plasmon resonance (SPR) measurements [24], therefore it can be considered as the ideal sample with perfect optical response. Figure 2.2 shows the relation between P_Δ, λ_i and the condition number of the matrix, given by

$$(\text{cond. number})_i = \frac{\max \lambda_i}{\min \lambda_i}. \tag{2.23}$$

First, the shadowed part of the ultraviolet region can be neglected due to an experimental noise. Second, there is an inverse proportion between P_Δ and λ_1. This supports the fact, that only $\mathbf{M}_1$ significantly contributes to the summation (2.21). As long as $P_\Delta \approx 0$, the condition numbers remain acceptable. However, for slightly depolarizing regions (red shadowing), the matrix becomes ill-conditioned. On other hand, the right-end of the blue region shows better

[3] Jones-Mueller matrix is a special case of Mueller matrix, which represents a nondepolarizing system. This is the only case, for which a physically meaningful Jones matrix can be found. If the Mueller matrix represents a depolarizing system, related Jones matrix can be always calculated, however it will stand for an unphysical description of given system.

[4] The decomposed matrices are constructed from the eigenvectors of the related coherency matrix, however related eigenvalues are close to zero for slightly depolarizing systems. Caluclated Mueller matrices are therefore poorly conditioned and the calculation is numericaly unstable.

[5] Theory is strict, however it can be shown, that for almost perfect system depolarizing less then 1 %, it is common to have at least one eigenvalue slightly negative. This raises from the experimental noise and numerical artifacts, and as long as the negative eigenvalue is close to zero, we omit it.

conditioning as the depolarization raises. For the case of $\lambda_1 \neq \lambda_{1,2,3} = 0$, the fraction in (2.23) diverges to infinity. The calculations were performed using algorithm presented in [25].

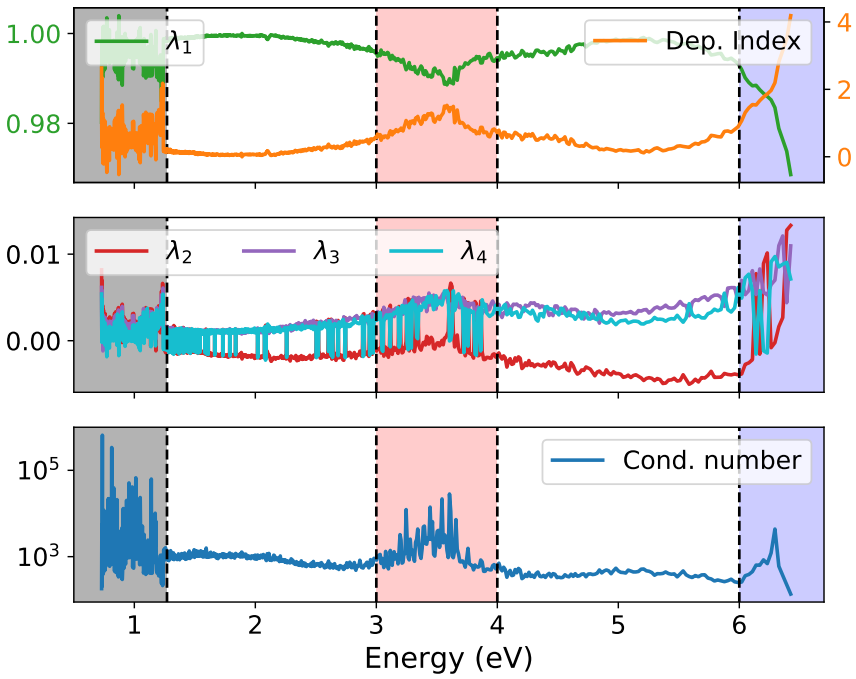

Figure 2.2: Quantities obtained during Cloud decomposition in relation with the depolarization of the sample. Noisy UV shadowed region is neglectable. Blue region: With increasing depolarizations, the Mueler matrix gets well-conditioned. Red region: Ill-conditioned matrix for depolarizations just around 1 %.

Depolarizing samples can be treated well with Le Roy-Bréhonnet decomposition [26]. The interpretation of this another type of the noise-filtering is rather straightforward, because resulting sum of the matrices is represented only with two matrices, representing the non-depolarizing contribution and the depolarizing contribution, respectively,

$$\mathbf{M} = \mathbf{M}_{\Delta=0} + \mathbf{M}_{\Delta=1}, \tag{2.24}$$

where the signal is typically contained in $\mathbf{M}_{\Delta=0}$ and is independent from $\mathbf{M}_{\Delta=1}$, which stands for an ideal depolarizer.

2.5.2 Product decompositions

Second cathegory of the Mueller matrix decompositions contains the product decompositions. The interpretation of the decomposed matrices is completely different. Regarding the sum decompositions, each Mueller matrix in the summations was containing relative part of the

intensity (signal). Due to this reason, for a general depolarizing system, each of the addend must be taken into account to process the matrices further. On the other hand, product decompositions provide products of Mueller matrices, which differ in the type of polarization property or quantity they describe, therefore it is possible to treat with each of the decomposed matrices separately, without concern for losing the physically reliable response, resulting in the numerical instability or misinterpretations, eventually.

The most common product decomposition is the Lu-Chipman decomposition. They proposed [27] the following decomposition:

$$\mathbf{M} = \mathbf{M}_{\Delta}\mathbf{M}_{\mathrm{R}}\mathbf{M}_{\mathrm{D}}. \tag{2.25}$$

Each of the decomposed matrices describe only one polarization property. Depolarization matrix

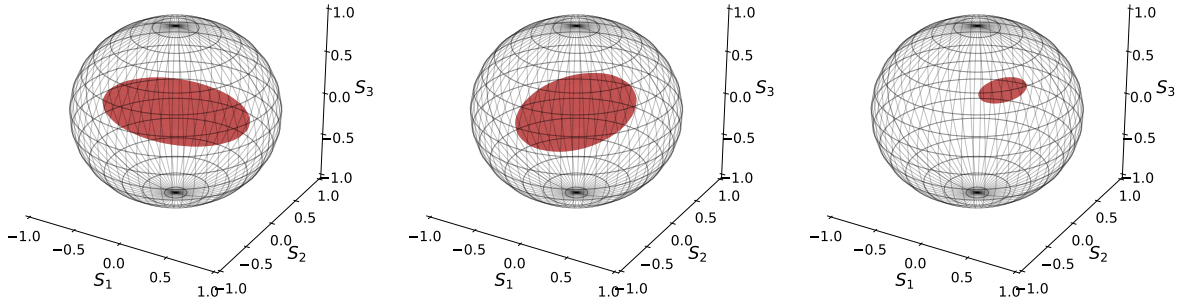

Figure 2.3: Poincaré sphere of output Stokes vector transformed by **Left**: a pure depolarizer, $\mathbf{M} = \mathbf{M}_{\Delta}$. **Centre**: retarder followed by depolarizer, $\mathbf{M} = \mathbf{M}_{\Delta}\mathbf{M}_{\mathrm{R}}$. **Right**: diattenuator followed by depolarized retarder $\mathbf{M} = \mathbf{M}_{\Delta}\mathbf{M}_{\mathrm{R}}\mathbf{M}_{\mathrm{D}}$.

$\mathbf{M}_{\Delta}$ contains information about the depolarization of the sample only. Retardation matrix $\mathbf{M}_{\mathrm{R}}$ represent the general (elliptical) retardation of the sample and diattenuation matrix $\mathbf{M}_{\mathrm{D}}$ is affected by the absorptions of the sample. Figure 2.3 summarizes the geometrical interpretation of the Stokes vector transformed by each of the decomposed matrices successively. Matrix $\mathbf{M}_{\Delta}$ maps the input polarization states (represented by a sphere) onto ellipsoid. The interpretation of the $\mathbf{M}_{\mathrm{R}}$ transformation is the rotation of the Poincaré surface[6] around the coordinate system origin. Finally, the form of $\mathbf{M}_{\mathrm{D}}$ is affected by the absorptions and the transformation result is a corresponding subspace of the input Stokes vector.

Because the matrix multiplication is not commutative, the change in the matrix multiplication order in Eq. (2.25) causes different results, thus there is no certainty, that the particular form of Eq. (2.25) reflects the real system correctly. Ossikovski [29] proposed reversed variation on the Lu-Chipman (forward) decomposition, which was experimentaly validated [30] and to completely avoid the multiplication order dependency, the symmetric decomposition was sug-

[6]More examples of the geometrical interpretation of the Poincaré sphere transformation are discussed in detail in [28].

gested [31],

$$\mathbf{M} = \mathbf{M}_{\mathrm{D2}}\mathbf{M}_{\mathrm{R2}}\mathbf{M}_{\mathrm{d}\Delta}\mathbf{M}_{\mathrm{R1}}^{\mathrm{T}}\mathbf{M}_{\mathrm{D1}}, \tag{2.26}$$

where diagonal depolarizer is encapsulated by pairs of diattenuators and retarders.

Beside discussed decomposition, several other types of Mueller matrix decompositions exist, for example differential decomposition [32] or integral decomposition [33]. Kindhearted reader can find a detailed overview in the purely theoretical excellent textbook [34].

Please, note the final remark on the Mueller matrix decompositions: They are not necessary for not complicated and isotropic samples, however they are quite essential in the description regarding strongly depolarizing, rough, non-ideal samples with unclear physical inerpretation – typically biological structures [7, 35]. For those structures, rigorous physically meaningful models are extremely cumbersome to obtain, therefore it is advantageous to separate the complex information from the sample, and model each of the polarization property individually using mathematical models, for example Monte-Carlo simulations [36, 37].

2.6 Mueller matrix: Theory versus Experiment

Mueller matrix contains complete information about the polarization properties of the sample, however, for particularly complicated sample, the useful information could be accursed in the overwhelming complexity of the corresponding Mueller matrix. Thus, the particular form of the measured matrix could be extremely complex and really challenging to understand, and can cause several difficulties with proper interpretation. This Chapter offers a basic insight into the problematics, and shows, how the polarimetric calculus and Mueller matrix theory are connected with the experiment and standard physical models.

2.6.1 Ideal Mueller matrix

Mueller matrix in the block-diagonal form

$$\mathbf{M}_{\mathrm{NCS}} = \begin{bmatrix} 1 & -N & 0 & 0 \\ N & 1 & 0 & 0 \\ 0 & 0 & C & S \\ 0 & 0 & -S & C \end{bmatrix}, \tag{2.27}$$

which is dependent only on two parameters ψ and Δ,

$$N = \cos 2\psi, \tag{2.28a}$$

$$C = \sin 2\psi \cos \Delta, \tag{2.28b}$$

$$S = \sin 2\psi \sin \Delta, \tag{2.28c}$$

which are connected with the p and s- refflection coefficients $r_{\mathrm{p,s}}$ through the ellipsometric equation

$$\frac{r_{\mathrm{p}}}{r_{\mathrm{s}}} = \tan\psi\, \mathrm{e}^{i\Delta}, \tag{2.29}$$

is called the NCS Mueller matrix. NCS matrices are easy to understand and model, but within given boundaries. Physically speaking, a NCS-type sample must be perfectly smooth, nonabsorbing, in theory composed of an infinite half-plane (thin-film structure allowed) and nondepolarizing. The absence of the depolarization in the NCS system could be mathematically verified using the necessary, but sufficient depolarization criterion [22],

$$\mathrm{Tr}\left(\mathbf{M}^{\mathrm{T}}\mathbf{M}\right) = 4m_{11}^2. \tag{2.30}$$

Applied on Eq. (2.27), we get

$$\mathbf{M}_{\mathrm{NCS}}^{\mathrm{T}}\mathbf{M}_{\mathrm{NCS}} = m_{11}^2 \begin{bmatrix} 1+N^2 & 0 & 0 & 0 \\ 0 & 1+N^2 & 0 & 0 \\ 0 & 0 & C^2+S^2 & 0 \\ 0 & 0 & 0 & C^2+S^2 \end{bmatrix}, \tag{2.31}$$

and finally,

$$\mathrm{Tr}\left(\mathbf{M}_{\mathrm{NCS}}^{\mathrm{T}}\mathbf{M}_{\mathrm{NCS}}\right) = 2m_{11}^2\left(N^2+S^2+C^2+1\right) = 4m_{11}^2, \tag{2.32}$$

which is a true proposition and the criterion (2.30) is fulfilled. The concept of the Mueller matrix ideality will be discussed into more detail next.

2.6.2 Mueller matrix purity

The depolarizing properties of every $\mathbf{M}$ can be quantified. An arbitrary normalized Mueller matrix (2.17) can be rewriten into the partitioned form [27] as

$$\mathbf{M} = m_{11} \begin{bmatrix} 1 & \boldsymbol{D}^{\mathrm{T}} \\ \boldsymbol{P} & \mathbf{m} \end{bmatrix}, \tag{2.33}$$

where $\mathbf{m}$ is 3×3 matrix. This convinient expression introduces the polarizance vector $\mathbf{P}$ and diattenuation vector $\mathbf{D}$. Their magnitudes are defined, respectively, as follows,

$$P \equiv |\boldsymbol{P}| = \sqrt{m_{21}^2 + m_{31}^2 + m_{41}^2}\,, \tag{2.34a}$$

$$D \equiv |\boldsymbol{D}| = \sqrt{m_{12}^2 + m_{13}^2 + m_{14}^2}\,. \tag{2.34b}$$

The alternative definition of the depolarization index (2.20) P_Δ (or the degree of polarimetric purity) of a system characterized by $\mathbf{M}$ was defined in [38] and further modified in [39] as,

$$P_\Delta^2 = \frac{1}{3}P^2 + \frac{1}{3}D^2 + \left[\frac{\sqrt{3}}{3}\|\mathbf{m}\|_2\right]^2 \in \langle 0,\, 1\rangle\,, \tag{2.35}$$

where the label $\|...\|_2$ is the Frobenius norm. P_Δ^2 represents a global measure of the system in terms of the depolarizations (or the ability to polarize). If $P_\Delta = 1$, the system is called *pure* and exhibits no effects leading to depolarizations. In order to analyze the depolarization effects into more detail, the degree of polarimetric purity P_P and the degree of spherical purity P_S are defined [39], respectively,

$$P_\mathrm{P} \equiv \left[\frac{1}{2}\left(P^2 + D^2\right)\right]^{1/2}, \tag{2.36a}$$

$$P_\mathrm{S} \equiv \frac{\sqrt{3}}{3}\|\mathbf{m}\|_2. \tag{2.36b}$$

P_P is a global quantity characterizing polarizing and diattenuation properties of the system (dichroism properties), while P_S stands for the complemetary contribution to P_Δ due to nonpolarizing attributes of the system (birefrigence properties). Therefore, the quantites P_P, P_S are independent of each other and form the two-dimensional *purity space*. Substituting (2.36) into (2.35), we obtain the equation of the purity space

$$\frac{2}{3}\frac{P_\mathrm{P}^2}{P_\Delta^2} + \frac{P_\mathrm{S}^2}{P_\Delta^2} = 1, \tag{2.37}$$

which stands for an equation of an ellipse. Physically meaningful is only the first quadrant of the ellipse. Moreover, if we set $P_\mathrm{S} = 0$, we get $P_\mathrm{P} = \frac{\sqrt{6}}{2}$, but it violates Eq. (2.37) in the form $P_\Delta^2 = \frac{2}{3}P_\mathrm{P}^2 + P_\mathrm{S}^2$, and a restriction must be evaluated. The restriction holds

$$P_\mathrm{P}^2 \leq \frac{1}{2}\left(1 + 3P_\mathrm{S}^2\right), \tag{2.38}$$

which is an equation of the hyperbole. The intersection of the areas given by (2.37) and (2.38) defines physically feasable region of the purity space.

Figure 2.4 shows the purity space. Edge BC (including points B and C) represent pure systems ($P_\Delta = 1$). Points B and C stand for an ideal retarder, and ideal polarizer, respectively. Vertex A represents an ideal depolarizer. Edge AB corresponds to depolarizing retarder, edge AD to partial polarizers. Hyperbolic segment CD represents nonpure polarizing systems, with its maximum polarizance lowered (from the ideal state at vertex C) by the presence of the complementary birefrigence effects. For a detailed analysis, see [34].

To connect the theory with the reality, we have performed the transmission Mueller matrix ellipsometry measurements on the commercialy available Agilent wire-grid polarizer (P) and the

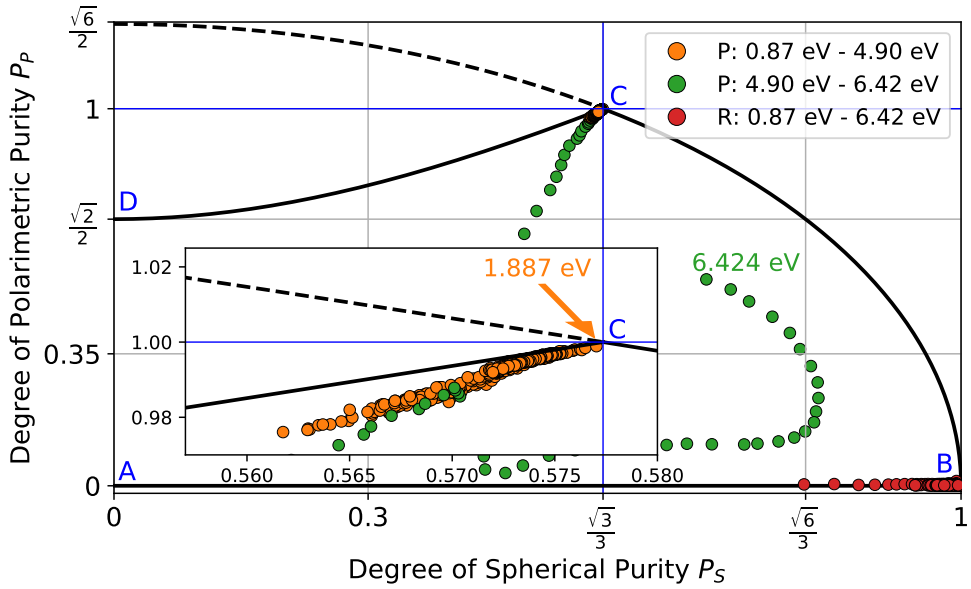

Figure 2.4: Feasable region ABCD of the purity space. The wire-grid polarizer (P) is not an ideal component for any of the measured wavelengths (orange points). The best performance was achieved for the energy of 1.887 eV. It exhibits strong birefrigence (green points) for higher energies. The waveplate (R) is an ideal component for a broad span of energies, but exhibits depolarization effects for particular wavelenghts.

experimental sample of compound quartz quarter-waveplate (R) from Meopta. Those samples should represent an ideal polarizing or retarding samples. The orange points represents the wavelengths for which the polarizer was designed to operate. The inset figure shows, that the polarizer is not ideal for any of the measured wavelengths. Nevertheless, the best performance is achieved at the energy of 1.887 eV – vertex C was marked for the clarity. The green points represent the wavelengths, for which the polarizer works outside from its designated region and transmits both s and p-polarized waves. Red points shows the performance of the measured waveplate. Apart of a few points, the waveplate can be concidered the ideal retarder, or slightly depolarizing retarder.

2.6.3 Note on the relation between Mueller matrices with $P_\Delta = 0$ and $P_\Delta = 1$

Consider two pure (with no depolarizations) Mueller matrices. Their summation produces *depolarizing* Mueller matrix [1].

Let us show you an example. Figure 2.5 shows the experimental configuration of our expeiment. There is an compound optical component, which is cut in half, where each of the halves represents ideal polarizer with its fast-axis perpendicular to the second polarizer axis. The axes orientations are $\varphi = 0°, 90°$, respectively. The totally polarized collimated beam with defined diameter of the spot size passes through the polarizers in such a manner, that the intensity

transmitted through each half is complemetary to the intensity trasmitted through the second half ($p + [1 - p] = 1$). The polarization of the incident light beam is transformed differently and

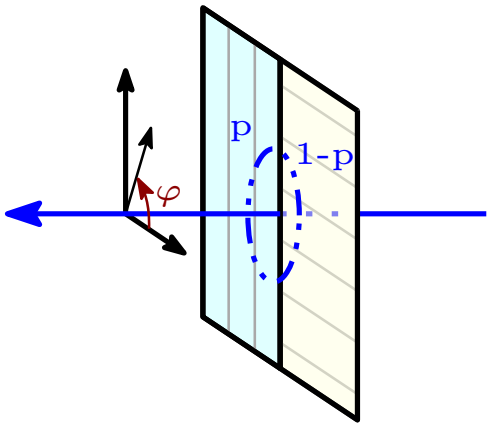

Figure 2.5: The scheme of the mental experiment. The collimated light beam is transmistted through the couple of ideal polarizers with its fast axes aligned at 0° and 90°, respectively. The depolarization index P_Δ of the transmitted beam is the function of p.

independently (incoherently) for each side of the component. The resulting Mueller matrix for the horizontal-vertical component is given by the weighted summation of both Mueller matrices [40]. The whole system is represented by the matrix $\mathbf{M}$

$$\mathbf{M} = p\,\mathbf{M}_{\mathrm{P}}(0) + (1 - p)\,\mathbf{M}_{\mathrm{P}}(90), \tag{2.39}$$

where p is the intensity fraction. Using Eq. (B.2), each polarizer is described with according Mueller matrix with respect to the particular value of φ, which leads to

$$\mathbf{M} = \begin{bmatrix} 1 & 2p-1 & 0 & 0 \\ 2p-1 & 1 & 0 & 0 \\ 0 & 0 & 0 & 0 \\ 0 & 0 & 0 & 0 \end{bmatrix}. \tag{2.40}$$

Using Eq. (2.35), the depolarization index takes the form of

$$P_\Delta^2 = \frac{1}{3}\left(4p^2 - 4p + 3\right), \tag{2.41}$$

with the global minimum (see Fig. 2.6) at the point $p = 1/2$. For this value, the system shows the strongest depolarizations. For the values of $p = \{0,\, 1\}$, the transmitted beam is horizontally or vertically polarized, respectively. For values $p \in (0,\, 1)$, the Mueller matrix (2.40) takes the

particular form of non-ideal depolarizer

$$\mathbf{M}\,(p=0.5) = \begin{bmatrix} 1 & 0 & 0 & 0 \\ 0 & 1 & 0 & 0 \\ 0 & 0 & 0 & 0 \\ 0 & 0 & 0 & 0 \end{bmatrix} = \mathbf{M}_{\Delta}. \tag{2.42}$$

According to Eq. (B.1), this Mueller matrix represents the partial ideal depolarizer.

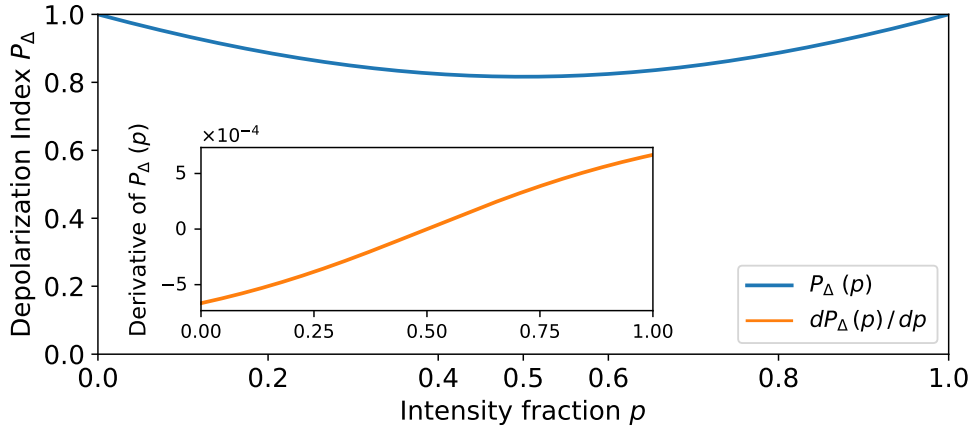

Figure 2.6: Depolarization index P_Δ of $\mathbf{M}(p)$ and its derivative as the function of p.

2.6.4 Ellipsometric instrumentation

The last aspect we would like to mention is an influence of the ellipsometer construction on the form of the measured Mueller matrix. There are several ellipsometer construction types, which differs depending on types and position of the optical components used in the particular device. Here, our scope will be limited to the rotating-elements ellipsometers only.

The rotating-elements ellipsometers are composed of polarization state generator (PSG), polarization state analyzer (PSA), light source and detector. Samples S are placed between PSA and PSG. PSG generates the polarization states of the light. It interacts with the measured sample, the polarization state is adequately changed and finally it is decoded in PSA. PSA and PSG in rotating-element ellipsometers are composed of polarizers P, analyzers A, and rotating waveplates (which are called compensators due to the historical reasons) C. Figure 2.7 shows graphical interpretation of Eq. (2.17) expressing measurable elements of the Mueller matrix in comparison to the ellipsometer construction type. [41]. Full Mueller matrix is obtainable only in the case of double-rotating compensator ellipsometer known as Mueller matrix ellipsometer, Fig. 2.7d. Other types of ellipsometers are not able to measure (red squares) last row and/or last column elements of the Mueller matrix. Those matrix elements contain the information about circular light transformation. Depending on which elements are missing, corresponding

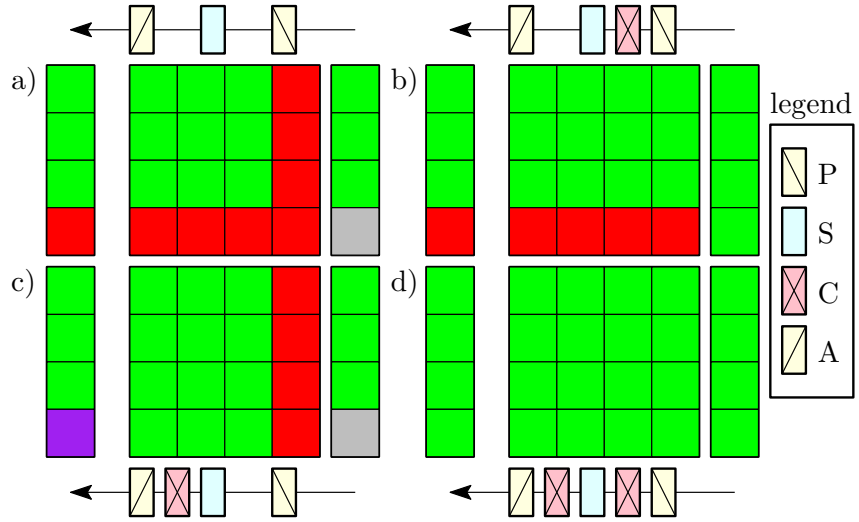

Figure 2.7: Graphical representation of the equation $\boldsymbol{S}^{\text{out}} = \mathbf{M}\boldsymbol{S}^{\text{in}}$ with respect to the ellipsometer construction type. The green squares represent measurable elements of the Mueller matrix (Stokes vector). The red squares are completely undetectable. Gray elements exist, but has no contribution to the signal. Purple element of case **c)** exists, however it does not bear any information about transformation of pure circular polarizations.

Stokes vector is obtained, but none of them (apart from 2.7d) contains the information about transformation of pure circular polarizations.

3 Introduction to Molecular optical activity

From our point of view, the optical activity phenomenon is absolutely textbook example of an interdisciplinary problem. It originates partly in Physics, partly in Chemistry, and the consequences are growing taller into Biochemistry and other sciences. Therefore, very special approach has to be choosed for the explanation. Sometimes, the rigorous theories full of juicy equations (purely physical approach) can be almost indigestible in its rare form. On the other hand, purely molecular (chemistry) approach can lead to the improper understanding of some phenomena arising from the optical activity. Therefore, this Chapter offers to a reader a gentle, illustrative, and explanatory way of understanding the basics of the optical activity phenomenon to build up the picture as clear as possible, stainless and smudgeless.

3.1 Historical overview

> No other chemical characteristic is as distinctive of living organisms as is optical activity.
>
> *George Wald (1957)*

We started this Chapter somewhat more ceremonially – with a quote. This sentence is written at the very begining of the famous George Wald's article [42]. The article offers very detailed description of important chemical experiments and observations which took place in history and were crucial in understanding phenomenon of the optical activity. We must not disregard authors personal insight into the problematics, everything spiced up with numerous rhetorical questions and author's brief flashbacks to the past. Now, let us start from the begining. As we proceed further, we will see, why George Wald's words are so true.

The pioneer of the optical activity phenomenon is considered Jean-Baptiste Biot. In his article [43] he observed, that when polarized light passes through optically active substance, it could be rotated clockwise or counterclockwise. After that, he continued with his research on various chemical compounds, both organic and inorganic. As a result, he formulated and defined the constancy of specific (or molecular) rotatory power [44], nowdays known as the specific rotatory power, as

$$[\alpha] = \frac{\alpha_{\text{obs}}}{l\,\sigma\,\rho}, \tag{3.1}$$

where α_{obs} is observed rotation in degrees, l is the length of the cell for liquid, σ is the fraction by weight of the optically-active compound and ρ is the density of the liquid. The meaning of the (3.1) will be discussed later, for now, note, that this equation is used until nowdays practically in the same form.

In the very same Mémoir [44] he proved the optical activity of the tartaric acid. The chemicals, which Biot choosed for his experiments were completely arbitrary, nearly randomly picked,

because the origin of the polarized-light plane rotation wasn't clear. The most crucial observation was made by Louis Pasteur in 1848 [45]. He studied physical and chemical properties of the tartaric acid, which involved crystallization experiments. He noticed, that in the tartarate solution, two forms of the tartaric crystals can be found. They were almost the same, they "differed only as an image in a mirror differs in its symmetry of position from the object which produces it" [45]. Based on this observations[7], he formulated terms of the Molecular Hemihedrism and the Molecular disymmetry. The later is according to International Union of Pure and Applied Chemistry (IUPAC) the obsolescent synonym for *chirality* [46]. Detailed explanation of these terms together with thorough historical overview can be found in the excellent textbook [47].

From this point further, the scope of the optical activity has to be devided into two main fields of interest. The goal of the chemists was to understand what is the origin of the optical activity at the atomic scale. The proposed theories and laws laied the foundations of the modern stereochemistry. On other hand, physicists were much more into quantification of the optical activity. The main questions were how to measure the polarization rotation of the optically active chemical solutions and to create physically meaningful mathematical models next [47]. Both of the branches, chemical and physical, are described in the following chapters into more detail.

Now, let us skip several decades of history and let us land in middle 1950's, when brand new medicine was introduced. Commericaly available medicine *Contergan* was advertised as a great treatment of morning sickness and nausea in pregnant women [48]. Very soon after Contergan was launched to the market, disturbing increase in amount of newborners with severe limb malignities was registered. It took almost 5 years and it cost thousands of children lifes and tenths of thousand of handicapped children until the scope of investigation was aimed to Contergan. Several researches were conducted and it was pointed out, that the Contergan's active ingredient – thalidomide – is the perpetrator [49]. Thalidomide exists in two forms. While its R-form is a completely harmless molecule, which treats the nausea well, the S-thalidomide is strongly teratogenic. The fundamentals of its mechanism can be summed up as rapid interconversion between R and S-form in physiological pH [10]. Thalidomide was banned for pregnant woman in 1961, however in several countries it continues to be used for leprosy or specific cancer types treatment [50].

Thalidomide tragedy showed us the importance of the optical activity. Before Contergan was released, the optical activity phenomenon was sort of trapped between nowhere and somewhere, it appeared in theories concerning molecular symmetry, in crystallography, but nobody actually paid attention to its biochemical aspect. On the other hand, as a consequence of the tragedy, precise laboratory tests and protocols of every single potentional medicine must be carried out,

[7] Pasteur's experiment with tartaric acid is very well-known, therefore Pasteur can be sometimes misunderstood as the first researcher who encountered the phenomenon of optical activity, which is not true. He can be considered as the pioneer of this field quite justifiably anyway.

so one can be absolutely sure, which compound form is treating with and what effects it causes[8]. This is only the one characteristics of the opticaly active compounds in the relation with life. George Wald's quote is going much further.

3.2 Stereochemistry of chiral compounds

Let us consider organic compounds first. The main principles, which manage the manifestation of optical activity in such a compounds were formulated by Le Bel [51]. He summarized his observations into a set of general principles, which must be fulfilled if the molecule possesses optical activity. They are explained rather lenghtily, but valid generally. Le Bel worked with molecules as if they were planar structures, which is not sufficient approach, when treating with optical activity. Van't Hoff noticed that, and he upgraded Le Bel's rules and generalized them to three-dimensional space [47, 52, 53].

Consider a molecule of tartaric acid with condensed chemical formula HOOC-C*(OH)H–C*(OH)H-COOH. The C atoms labeled with star are called the *asymmetric carbon atoms*. It is possible to illustrate the spatial strucure of tartaric acid using van't Hoff's polygons, see Fig. 3.1. Two assymetric carbons linked together with a single bond are represented by two tetrahedrons linked to the apex of each other. If we place planar mirror between the tetrahedrons, we can see, that the first two cases exhibits no symmetry even upon the tetrahedra rotation. These structures are called *chiral* and each represents stand-alone chemical individuum. The last example at Fig. 3.1 shows, that the tetrahedrons are mirror images of each other, which correpospond to *achiral* molecule – without optical activity. Van't Hoff extended his theory to molecules with double

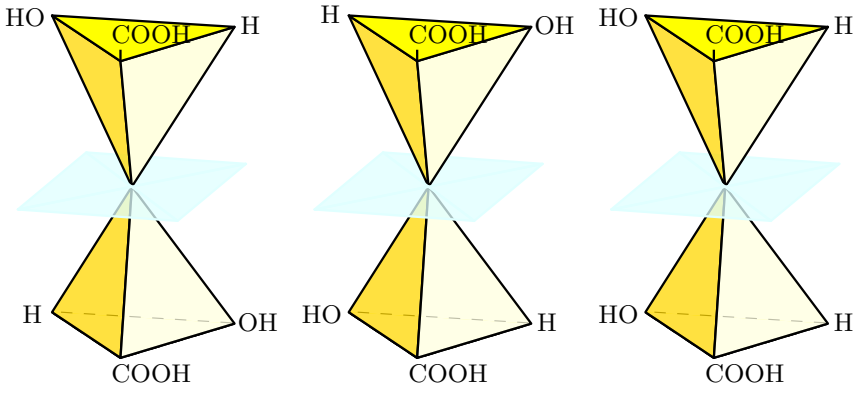

Figure 3.1: Van't Hoff representation of tartaric acid [52]. Assymetric carbons linked with a single bond are represented by apex-connected tetrahedra. If the tetrahedra are not their own mirror images, the molecule is chiral. Therefore, we distinguish between L and D-tartaric acid. Meso-tartaric acid is symmetric along the horizontal symmetry plane.

and triple-bonded asymmetric carbons, which are represented by two tetrahedrons connected

[8] Another interesting example is methamphetamine. R-form is well-known central nervou system stimulant, while S-form acts as a mild hypertension relieve.

with common edge, and common face, respectively [47, 52]. The polyhedral representation of molecules is no longer used, because it was replaced with cleaner and simplier Fisher representation [54], despite the fact they are equal. Figure 3.2 shows the transition between each representation. Fisher's notation is a simple inplane projection of Van't Hoff's polyhedrons. From now on, we will use Fisher projection only[9].

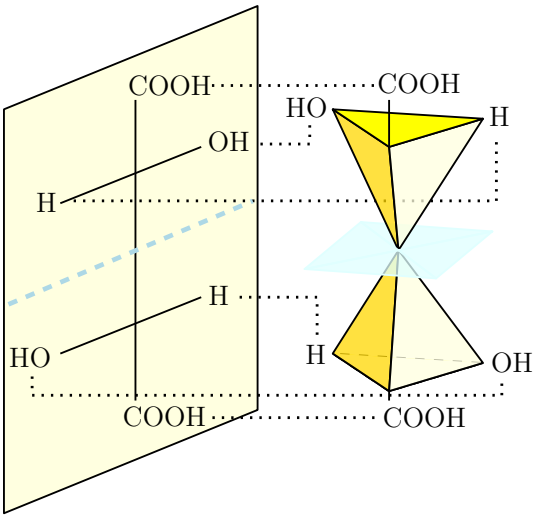

Figure 3.2: Fisher graphical representation of molecule is the inplane projection of Van't Hoff representation. While Fisher projection is simple and clean, Van't Hoff is more explanatory.

Now, having the visualization established, we can make the description more abstract. First, the asymmetric atom is not limited to carbons only, it can be almost arbitrary asymmetric atom, for example quaternary N, tetravalet P or sulfoxidic S [56]. We call these atoms to be the *chirality centres*. The most simple chiral molecule contain only one chirality centre. Obviously, this molecule is always chiral. Voluntary exercise for a reader: It can be demonstrated using your hands (similarly to Fig. 3.1). If you arrange your hands (each representing the same chiral molecule) opossitely to each other, then rotate one hand by 180° and superimpose them, you will find out, that your hands are chiral. Therefore, we sometimes talk about the *handedness* of molecules. However, chiral molecules, which contains two or more chirality centers, does not have to be necessarily always chiral. To understand this, we need to introduce formal nomenclatures.

The most general Cahn-Ingold-Prelog nomenclature (priority rules) [57] distinguishes between R and S chirality centres and is based on the determination of the direction, in which bonded groups molar mass increases and with respect to their chemical priority. The R, S descriptors are related only with given chirality centre of a molecule. Together with E, Z descriptors, it uniquely determines the absolute conformation of particular enantiomer, whether or not it is chiral. However, RS nomenclature describes the chirality centre itself, one by one, and it does not take into account the effective characteristics of the molecule. In practice, D and L

[9]For eager readers we can recommend Ronald Bentley's article [55] *Are Fischer Projection Formulas Really Necessary?*

relative conformation descriptors are used, because they directly reffer to the spatial structure of the molecule and its handedness. To be more precise, by further investigation it was shown, that D-form and L-form may not correspond to the side, in which the plane of the polarized light is rotated. To describe also this phenomenon, signs (+) for clockwise rotation and (–) for counterclockwise rotation were added as correction prefices.

3.3 Chiral molecules in the living Nature

First, let us take a closer look on the nomenclatures. The descriptors D and L are derived from Latin and their meaning is *Dexter* (right-sided) and *Laevus* (left-sided), respectively[10]. The E and Z have come from German, and stand for *Entgegen* (opposite to) and *Zusammen* (together), respectively (correspondence with *cis* and *trans* conformations). Finally, R and S prefices have its roots in Latin words *Rectus* and *Sinister*. Let the reader be aware of possible incorrect translation as *Right(-sided) and Left(-sided)*, which is quite common especially in popular scientific texts. The correct meanings for Rectus and Sinister are, respetively, *proper (right)*, and *improper*[11].

The essential chemical compounds for the living organisms is the triad of proteins, saccharides, and fats. The structure of proteins is scalable [58]. In context of the optical activity, the tertiary and quaternary structure is not that important as the primary and secondary structure. Primary structure of the protein is a sequence of aminoacids in a polypeptide chain. Each of the aminoacids has its own chirality centres, and is therefore optically active. It was investigated, that the vast majority of the aminoacids in living organisms exists in the L-form exclusively [11]. The handedness of each molecule preserves whether it participates on some biochemical reaction or remains intact at the moment. The chain of the aminoacids forms spatial secondary structures: α-helix or β-sheet. The spatial structure arrangement of proteins contributes to the optical activity with its own handedness and changes the measurable quantities (e.g. specific rotatory power (3.1)) with respect to the secondary structure disorder [59].

On the other hand, saccharides in living matter exist exclusively in the D-form. DNA and RNA nucleic acids contains D-Deoxyribose (sugar) as one of its main structural components [60]. From the chirality point of view, those acids can be considered as hybrids between proteins on the secondary level and simple saccharides[12].

The absence of the complementary enantiomer of particular chemical within living organisms is called the *homochirality* [61]. Following observations were done: First, every thermodynamical

[10] It corresponds with the obsolete name for Glucose (Dextrose) and Fructose (Levulose), respectively. Glucose rotates the polarization plane to the right side (clockwise), while Fructose to the left side (counterclockwise).

[11] The incorrect translation have possibly come from the medicine terminology. In medicine, the parity is given by latin words *sinister* (for *leftside*) and *dexter* (for *rightside*). In the context of the optical activity, the word *sinister* is connected with historical collocations, because it was understood as a pejorative term for something being wrong, evil, akward or left-handed (left-handed people were considered to be against Nature and God during the Middle Ages).

[12] For following purposes of the thesis, the chirality of saccharides will be discussed in the following Chapter into more detail.

system drives toward the racemic composition (equimolar ammount of D and L isomers) [11]. Second, it is not possible to achieve an absolute asymmetric synthesis (a synthesis without the aid of an asymmetric molecule as a reactant or catalyst) in the laboratory conditions [62]. How it is possible, that living organisms preserved the ability of this synthesis and the products do not tend to racemic mixtures? Organic molecules have the ability to autocatalysis (self-reproduce). This implies, that it must exists a mechanism for homochirality preservation in *prebiotic* systems (complex organic molecules before RNA existence). Various mechanisms, how to introduce an enantiomorphic excess (purity of chiral compounds) into assymetric catalysis were proposed [66], including photochemical catalysis [63], or the influence of the circular polarized light [64, 65]. As it is difficult to unambiguously prove one or other theory, this field yields open questions, what are the prerequisities for the life, and what is the actual possible origin of the life (in the physical-chemical point of view) [66]. Nice review on the optical activity manifestation in different materials was published in [67].

By now, I hope, that the true meaning of George Wald's quote from the Chapter beggining is crystal clear.

3.4 Rotatory power dispersion: Phenomenological approach, history

Specific rotatory power $[\alpha]$ is considered the optical response of an optical system. Therefore, we expect a dispersion in $[\alpha]$ over the wavelength λ. Moreover, the value of $[\alpha]$ is temperature-dependent, as we know from the reaction kinetics (equilibrum constant shifting with temperature T changes). Therefore, for a particular wavelength λ and constant temperature T, the system is responding with corresponding value of $[\alpha]$, which should be therefore labeled as $[\alpha]^T_\lambda$.

Contemporaneously with Le Bel and Van't Hoff research on theory of asymmetric carbon, the effort for quantifying the rotary disperson was in process [47]. First dispersion models were developed by Cauchy [47] and von Lang [68], but their form originated from the mathematical basis and empirical observations based on experiments. The requirement of chiraly isotropic medium (all chirality centres are identical) was presumed by Drude [69]. He noticed, that absorbing media contains natural vibrations. Assuming the vibrations of the chirality centres, he proposed an equation

$$[\alpha] = \sum_i \frac{k_i}{\lambda^2 - \lambda_i^2}, \tag{3.2}$$

where constant k_m is connected with the number of vibrations in unit volume and other medium parameters. The summation can be ommited in most cases, as only one i-th vibration is dominant. Drude's concept was used further by Sellmeier, who pointed out, that the vibration wavelength region differs widely from the measured transparent region of the dispersion. Therefore, the normal dispersion of the non-absorbing medium can be expressed by Sellmeier's equation

$$n^2 = 1 + \sum_i \frac{A_i \lambda^2}{\lambda^2 - \lambda_i^2}. \tag{3.3}$$

One of the main scopes of the biochemists in the middle of 20th century were proteins. Proteins are usually very complex structures with many chirality centres, therefore Drude's assumption was no longer valid. Moffitt and Yang proposed [70], that instead of $[\alpha]$, new quantity of effective molecular rotations $[m]$ is needed. The physical meaning of $[m]$ is effective residue of monomer rotation – the contribution of $[\alpha]$ of chiral monomers in polymeric achiral structures after polymerization. Based on the quantum theories, following equation was derived:

$$[m] = \sum_i \frac{a_i \lambda_i^2}{\lambda^2 - \lambda_i^2} + \sum_i \frac{b_i \lambda_i^4}{\left(\lambda^2 - \lambda_i^2\right)^2}, \tag{3.4}$$

where the first term reflects the rotary dispersion of the molecules, and the second term is connected with the protein secondary helical structure. The summation can be neglected, as a dominant vibration is accounted only. Based on various experiments (overview in [71]), highly disordered systems possess values of $b_i \to 0$. This is useful for example in a description of protein denaturation[13].

3.5 Simple measurements of rotatory power

Each of proposed model of rotatory power dispersion was either empirically deducated based on the experimental data or was experimentally validated afterwards.

The first polarimeters used for the measurements of chiral solutions were based on eye detection if the optical response is present. Thus, they were only able to answer the question whether a solution is chiral or not. The very first visual polarimeter was consructed by Nörrenberg. The sunlight was polarized by a reflection from a glass plate aligned at Brewster angle. The analyzer glass plate was tilted at Brewster angle. When the horizontal axes of glass plates are mutually perpendicular, the ray is extinguished. If a chiral solution was placed between the glass plates, the plane of the polarized light was rotated, the Brewster law was violated and visible light beam was spoted. The polarization optics was gradually replaced with more effective prism polarizer and analyzer, and the sunlight was changed by monochromatic sodium light sources. The detection was however based on the manual reading of the polarized plane azimuth inclination. Note, that polarimeters constructed for sugar solution measurements were called saccharimeters. Instead of rotating analyzer, the quartz compensator was used. Rotating the compensator, the concentration of sugar in solution could be determined using the scale, when the compensator was set to give a zero total rotation.

With a development of electronic detectors, the basic construction of either polarimeters and saccharimeters is composed of a light source (mostly sodium lamps with D spectral line of $\lambda = 589\,\mathrm{nm}$), fixed polarizer, adjustable analyzer, long tube (reservoir for a chiral solution, usually up to a few dm long) and a light intensity detector. The scheme of a single wavelenghth polarimeter (saccharimeter) is shown in Fig. 3.3. The calculations of rotatory power are based on the Malus law.

[13] The most common example of the protein denaturation is the heat-induced albumen denaturation (fried eggs).

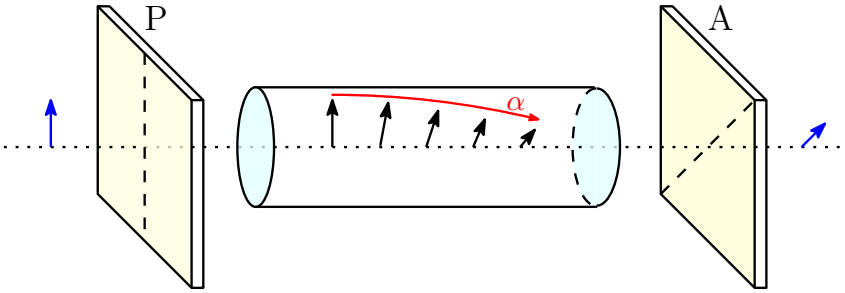

Figure 3.3: Scheme of the tube polarimeter for rotatory power measuements. The (centimeters up to a few decimeters long) tube is filled with chiral solution. The light emmited by a monochromatic source is linearly polarized with a polarizer P. The polarization plane is rotated as the wave propagates through the chiral solution. The angle of the polarization plane rotation is calculated according to Malus law.

3.6 Optical activity: Perspective of the phenomenon

The physical foundations of the simple polarimetric and saccharimetric measurements have remained practically intact over decades. The main improvements of the measurement technique are based on more precise polarization optics and more sensitive detectors. However, it is convenient to extend the frequency range outside the visible spectrum of the light or to introduce a new experimental method, which brings the optical activity phenomenon in a new light (literally!).

In the following Chapters, we introduce the optical activity of liquid and solid media in the frame of Mueller matrix ellipsometry, therefore, we will not discuss this method here. Each experimental technique is suitable for measurement of different physical property of the sample. For example, Raman optical activity together with Vibrational optical activity are great approaches for the determination of the absolute configuration of organic [72, 73], biochemical [74], or organometallic [75] compounds, because it combines the structural sensitivity of vibrational spectroscopy with the stereochemical sensitivity of an optical activity itself [76]. From nature of those measurement techniques, the experiments upon those techniques are involved among the variety of natural materials. The proper description of the optical activity on the molecular level is far beyond the scope of the thesis. The detailed description of microscopic optical activity is given in [77].

Now, let us extend the frequency region further, and comment on the terahertz (THz) optical activity briefly. THz radiation [78] is nowdays very rapidly developing area with many fields of interests and applications including security [79], biomedical imaging [80] or ultra-short THz pulses [81]. The THz measurements of natural optical activity in natural materials is not in the scope of the contemporary research, mainly because the optical response of the optical activity in THz region is very small or below the detection limit [82]. However, there is an extensive effort to incorporate the THz spectral range into the optical activity phenomenon

using artificially prepared structures or metamaterials[14]. The term *optical activity* is connected rather with natural materials, therefore we will use term *chirality* instead, when speaking about artificial structures or metamaterials.

The connection between THz radiation and metamaterials is advantageous, because the wavelength of the THz radiation, together with the dimensionality of the prepared structures, exhibits various effects as a result. In other words, THz waves are long enough to be able to interact with the chiral metamaterial, which dimensionallity is given by the limits of the manufacturing process.

To control the polarization properties of the THz wave, various designs of polarization state modulators and active manipulation polarization components exist: Transmission THz polarization rotator was proposed [12] for the polarization and phase control of the incident wave. The schemes of all proposed optical components are shown in Fig. 3.4. Note, that the figure is shown for the illustration purpose only. The metamaterial was based on the double metasurface, with anisotropic rectangular-shaped silicon pillars etched into the substrates. The relative rotation between two metasurfaces controls the polarization properties of the transmitted wave Fig. 3.4a. Choi et al. [85] proposed parylene (polymer with high transparency across the THz spectrum) polarization modulators with Au deposited Herringbone structure for the ellipticity control of transmitted wave, which can be used for THz circular dichroism spectroscopy Fig. 3.4b. Parylene substrates were used also in structures proposed in [86], Fig. 3.4e. Ellipticity control was achieved also using THz chiral metasurface based on multi-layered graphene [87] or single graphene layer [88], see Fig. 3.4d. The metasurfaces based on Fresnel nonlinear zone plates were introduced in [89], and are used for the conversion of near-infrared (NIR) wave to THz wave. Other designs are shown only for the illustration [90, 82].

We believe, that in time, and maybe with the help of the metamateral-based devices, we will have better THz generators, precise dynamic polarization control, and more sensitive detection, and we will be able to fully characterize the chirality in natural materials with low response in THz range.

[14]Metamaterials are man-made composite structured materials with unique electromagnetic properties. The *father* of the metamaterials was Veselago [83], who created the concept of the materials with both negative permittivity and permeability. Those materials were hugely developed and made famous by Pendry [84].

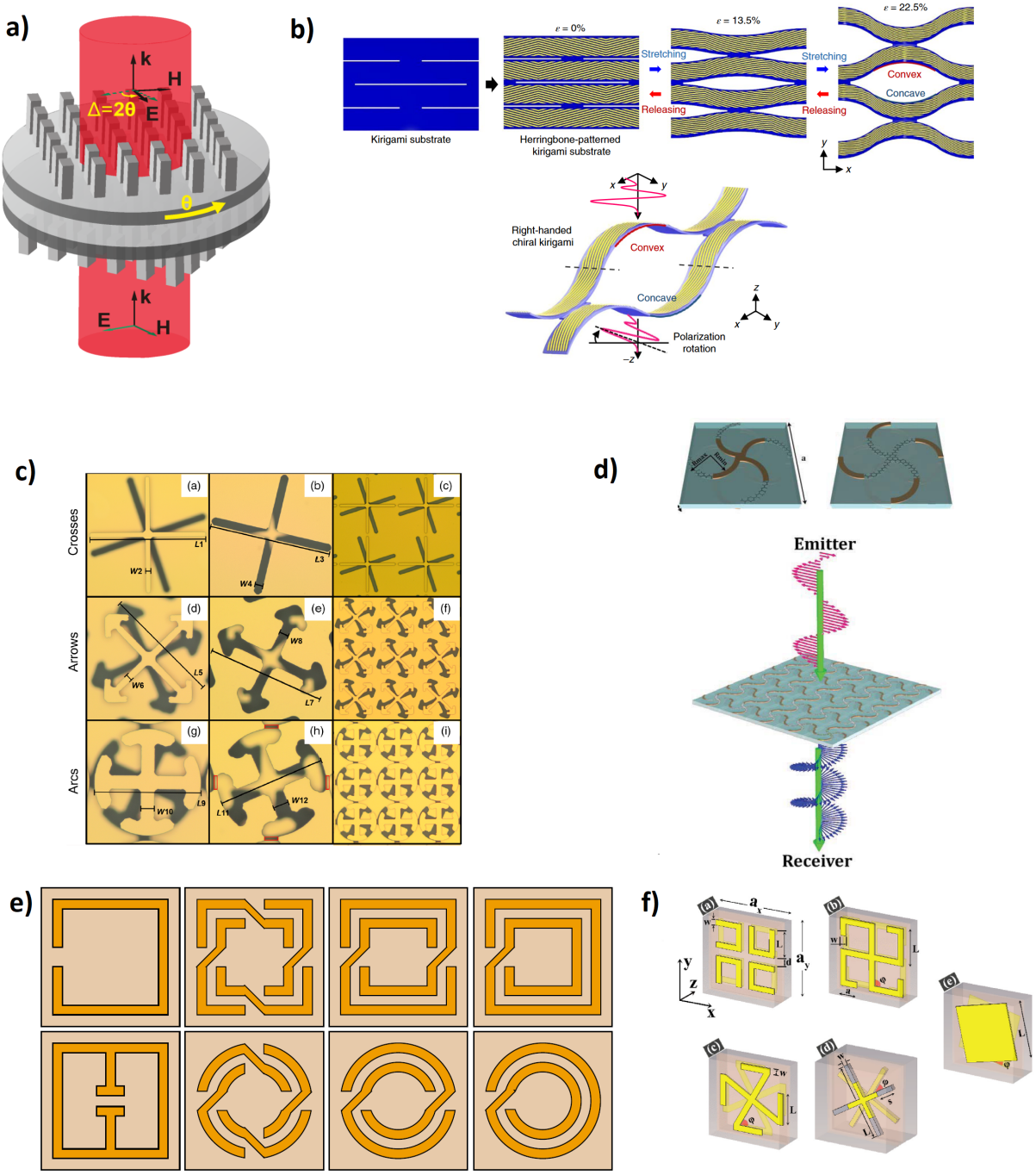

Figure 3.4: **a)** The polarization plane rotation is controled by a rotation of the metasurface [12]. **b)** Kirigami parylene polarization modulators with Au Herringbone structure for the circular polarization light generation. The control is produced by stretching of the structure [85]. **d)** Single layer graphene meta-surface for the circular polarized THz light generation [88]. **e)** Parylene based metastructures [86]. **c, f)** Examples of other designes for control of the THz polarized light properties [90, 82].

4 The concept of Chirality: Rigorous approach

The goal of this Chapter is to calculate the eigenmodes propagating in various anisotropic media. In order to do this, the effect of optical activity (or the gyration) must be evaluated correctly, and the material equations (2.2) must have incorporated the contribution of that phenomenon. Various constitutive relations [91] have been proposed until nowdays, and altough they are equivalent to each other, it may be beneficial to use one or other approach depending on a situation. For example, while Berreman's method is perfectly suitable for numerical calculations, Fedorov's covariant method[15] stands for an elegant and efficient way for analytical derivations.

- Born-Landau [92] constitutive relations (commonly used in Yeh's 4×4 matrix approach of eigenvalue problem):

$$\boldsymbol{D} = \varepsilon \boldsymbol{E} + \mathrm{i}\boldsymbol{G} \times \boldsymbol{E}, \tag{4.1a}$$

$$\boldsymbol{B} = \boldsymbol{\mu} \boldsymbol{H}, \tag{4.1b}$$

  where $\boldsymbol{G}$ is the gyration vector.

- Berreman-Drude constitutive relations [93] (6×6 Berreman's matrix method):

$$\boldsymbol{D} = \varepsilon \boldsymbol{E} + \mathrm{i}\gamma \boldsymbol{H}, \tag{4.2a}$$

$$\boldsymbol{B} = \boldsymbol{\mu} \boldsymbol{H}, \tag{4.2b}$$

  where $\boldsymbol{\gamma}$ is the optical rotation tensor.

- Condon-Fedorov constitutive relations [94, 95] (Fedorov's covariant method):

$$\boldsymbol{D} = \varepsilon \boldsymbol{E} + \mathrm{i}\boldsymbol{\alpha} \boldsymbol{H}, \tag{4.3a}$$

$$\boldsymbol{B} = \boldsymbol{\mu} \boldsymbol{H} - \mathrm{i}\boldsymbol{\alpha}^{\mathrm{T}} \boldsymbol{E}, \tag{4.3b}$$

where $\boldsymbol{\alpha}$ is the gyration tensor. In the following text, we will use Condon-Fedorov notation mainly.

4.1 Onsager-Casimir principle

In a broad variety of literature, the derivation of Condon-Fedorov constitutive relations is disregarded. The basis of the Eqs. (4.3) is given by a definition of Tellegen's constitutive relations

[15] The Fedorov covariant (coordinate-free) method has some algebraic specifics. Probably the best overview on covariant linear algebra was introduced in his book [95] in Chapter IV: Elements of Linear Algebra and Direct Tensor Calculations. (Глава IV: Элементы линейной алгебры и прямого тензорного истчисления.) Unfortunately, the book was never translated from Russian.

[96] of general bianisotropic media:

$$\boldsymbol{D} = \boldsymbol{\varepsilon}\boldsymbol{E} + \boldsymbol{\alpha}\boldsymbol{H}, \tag{4.4a}$$

$$\boldsymbol{B} = \boldsymbol{\mu}\boldsymbol{H} + \boldsymbol{\beta}\boldsymbol{E}, \tag{4.4b}$$

where $\boldsymbol{\varepsilon}$, $\boldsymbol{\mu}$, and $\boldsymbol{\alpha}$, $\boldsymbol{\beta}$ are general second-rank tensors and coupling tensors, respectively. The coupling terms express, that when medium is exposed to an electric field $\boldsymbol{E}$, it will become magnetically polarized and vice versa. The constitutive relations can be rewriten into the matrix form as

$$\begin{bmatrix} \boldsymbol{D} \\ \boldsymbol{B} \end{bmatrix} = \begin{bmatrix} \boldsymbol{\varepsilon} & \boldsymbol{\alpha} \\ \boldsymbol{\beta} & \boldsymbol{\mu} \end{bmatrix} \begin{bmatrix} \boldsymbol{E} \\ \boldsymbol{H} \end{bmatrix}. \tag{4.5}$$

Because all fields are time-dependent, we can use the Onsager theory [97, 98]. Onsager developed a general theory of irreversible thermodynamical systems. He assumed, that if the system is exposed to arbitrary affinities a_k it responds with associated flux j_i. He further assumed, that the flux-affinity relation[16] is linear and that each flux is not dependent only of its associated affinity, but also of every other affinities. The relation is given by the coefficients of a linear response (or kinetic coefficients) L_{ik},

$$j_i = \sum_k L_{ik} a_k. \tag{4.6}$$

The Eq. (4.5) can be therefore rewriten[17] as

$$F_i = \sum_{k=1}^{6} L_{ik} Y_k. \tag{4.7}$$

The theory was enhanced by Casimir [100] and the main result of the Onsager-Casimir theory is the proof of following symmetry of kinetic coefficients:

$$L_{ik}(\boldsymbol{B}) = L_{ki}(-\boldsymbol{B}). \tag{4.8}$$

The proof is based on the time-reversal symmetry of motion equations. Time-reversed motion equations remains the same in the presence of $\boldsymbol{B}$ (or $\boldsymbol{D}$), but not if the sign of the fields is changed. The time-reversal symmetry applied on (4.5) and (4.8) gives following symmetries

[16] In other words, Onsager theory describes the behaviour of a linear thermodynamical systems describing any irreversible process near the state of the thermodynamic equilibrium. The affinities can be understood as forces, which drive the irreversible system out from its equilibrium state. The system responds with related flux, which are linearly dependent of the related affinity. Onsager reciprocal relations are sometimes considered the fourth thermodynamic law [99].

[17] Here, the forces (affinities) shifting the irreversible thermodynamic process out of the equilibrium state are the field intensities, and the system is responding by generating the associated displacements.

between the tensors in (4.4).

$$\boldsymbol{\varepsilon} = \boldsymbol{\varepsilon}^{\mathrm{T}},\ \boldsymbol{\mu} = \boldsymbol{\mu}^{\mathrm{T}},\ \boldsymbol{\alpha} = -\boldsymbol{\beta}^{\mathrm{T}}. \tag{4.9}$$

The electromagnetic energy conservation law[18] with no energy dissipation ($\boldsymbol{j} = 0$) takes the form

$$\underbrace{\left[\boldsymbol{E}\,\frac{\partial \boldsymbol{D}}{\partial t} + \boldsymbol{H}\,\frac{\partial \boldsymbol{B}}{\partial t}\right]}_{\partial w/\partial t} + \mathrm{div}\,\underbrace{(\boldsymbol{E} \times \boldsymbol{H})}_{\boldsymbol{S}} = 0, \tag{4.10}$$

where $\boldsymbol{S}$ is the Stokes vector and w is the density of electromagnetic energy. The first term can be rewriten with respect to (4.7) as

$$\boldsymbol{E}\,\frac{\partial \boldsymbol{D}}{\partial t} + \boldsymbol{H}\,\frac{\partial \boldsymbol{B}}{\partial t} = \sum_{k}^{6} Y_k \frac{\partial F_i}{\partial t}. \tag{4.11}$$

Supposing monochromatic waves only, this equation can be rewriten as

$$\boldsymbol{E}\boldsymbol{D}^* + \boldsymbol{H}\boldsymbol{B}^* - \boldsymbol{E}^*\boldsymbol{D} - \boldsymbol{H}^*\boldsymbol{B} = \sum_{k}^{6} \left(Y_i F_i^* - Y_i^* F_i\right). \tag{4.12}$$

Assuming (4.7), the expression becomes

$$\sum_{i,k=1}^{6} \left(Y_i L_{ik}^* Y_k^* - Y_i^* L_{ik} Y_k\right). \tag{4.13}$$

The Eq. (4.13) must be satisfied for any possible affinity (field). From Onsager-Casimir theory can be shown, that this is satisfied, if

$$L_{ik}^* = L_{ki}. \tag{4.14}$$

Therefore, following symmetries are valid:

$$\boldsymbol{\varepsilon} = \boldsymbol{\varepsilon}^{\dagger},\ \boldsymbol{\mu} = \boldsymbol{\mu}^{\dagger},\ \boldsymbol{\alpha} = \boldsymbol{\beta}^{\dagger}. \tag{4.15}$$

If a medium is non-dissipating,

$$\boldsymbol{\varepsilon} = \boldsymbol{\varepsilon}^{\mathrm{T}},\ \boldsymbol{\mu} = \boldsymbol{\mu}^{\mathrm{T}},\ \boldsymbol{\alpha}^{\dagger} = -\boldsymbol{\alpha}. \tag{4.16}$$

The constitutive relations between $\boldsymbol{D}$, $\boldsymbol{B}$ and $\boldsymbol{H}$, $\boldsymbol{E}$ for monochromatic waves are obtained

[18]The derivation of the electromagnetic energy conservation law is based on the curl Maxwell equations. We must expand them by $\boldsymbol{H}$, $\boldsymbol{E}$ and subtract them. The law is then derivated with the help of the vector identity $\mathrm{div}\,(\boldsymbol{E} \times \boldsymbol{H}) = \boldsymbol{H}\,\mathrm{rot}\boldsymbol{E} - \boldsymbol{E}\,\mathrm{rot}\boldsymbol{H}$.

from the time-reversal symmetry theorem. It is convenient to use the pseudotensor $\mathrm{i}\boldsymbol{\alpha}$ [101]:

$$\boldsymbol{D} = \boldsymbol{\varepsilon}\boldsymbol{E} + \mathrm{i}\boldsymbol{\alpha}\boldsymbol{H}, \tag{4.17a}$$

$$\boldsymbol{B} = \boldsymbol{\mu}\boldsymbol{H} - \mathrm{i}\boldsymbol{\alpha}^{\mathrm{T}}\boldsymbol{E}, \tag{4.17b}$$

Further, we showed, that for non-dissipative media and monochromatic waves, following constitutive relations are valid:

$$\boldsymbol{D} = \boldsymbol{\varepsilon}\boldsymbol{E} + \mathrm{i}\boldsymbol{\alpha}\boldsymbol{H}, \tag{4.18a}$$

$$\boldsymbol{B} = \boldsymbol{\mu}\boldsymbol{H} - \mathrm{i}\boldsymbol{\alpha}\boldsymbol{E}, \tag{4.18b}$$

Note, that these constitutive equations are valid for non-dissipative media [102] and monochromatic waves only. This fact is almost always disregarded across the literature.

4.2 General eigenvalue solution

The curl Maxwell equations (2.1c) and (2.1d) for a monochromatic plane wave can be in CGS[19] units rewriten as

$$\mathbf{m}^{\times}\boldsymbol{E}_0 = \boldsymbol{B}, \tag{4.19a}$$

$$\mathbf{m}^{\times}\boldsymbol{H}_0 = -\boldsymbol{D}, \tag{4.19b}$$

where

$$\mathbf{m}^{\times} = \begin{bmatrix} 0 & -m_3 & m_2 \\ m_3 & 0 & -m_1 \\ -m_2 & m_1 & 0 \end{bmatrix}. \tag{4.20}$$

We say, that tensor $\mathbf{m}^{\times}$ is dual to the associated refraction vector $\boldsymbol{m}$, which is defined as

$$\boldsymbol{m} = n\boldsymbol{n} = n \begin{bmatrix} n_1 \\ n_2 \\ n_3 \end{bmatrix} = \begin{bmatrix} m_1 \\ m_2 \\ m_3 \end{bmatrix}, \tag{4.21}$$

and which determines the direction $\boldsymbol{n}$ of the wavector $\boldsymbol{k}$ of the light propagating in the medium. Assuming the normal incidence, $\boldsymbol{n} = [0,\ 0,\ 1]^{\mathrm{T}}$. In the case of non-normal incidence, the tangential component of the wavevector (and of the refraction vector) must be conservated. In terms of $\boldsymbol{m}$, its tangential component is expressed as $n \sin\varphi_1$. From the Snell law we have $n \sin\varphi_1 = n_0 \sin\varphi_0$, where n_0 is the refractive index of the ambient medium and φ_0 is the angle of incidence (defined in $13\,(xz)$ plane from the $3\,(z)$-axis.)

[19] The main reason, why choose the Fedorov covariant method (coordinate free method) is its elegancy and simplicity. However, the elegancy would disappear if the Maxwell equations were not in CGS system. Nevertheless, it has no impact on the quality of the physics, nor on the final form of the solution of eigenmodes propagating in particular medium.

By substitution of Equations (4.17) into (4.19) we obtain

$$\mathbf{m}^{\times}\boldsymbol{E}_0 = \boldsymbol{\mu}\boldsymbol{H}_0 - \mathrm{i}\boldsymbol{\alpha}^{\mathrm{T}}\boldsymbol{E}_0, \tag{4.22a}$$

$$\mathbf{m}^{\times}\boldsymbol{H}_0 = \boldsymbol{\varepsilon}\boldsymbol{E}_0 + \mathrm{i}\boldsymbol{\alpha}\boldsymbol{H}_0. \tag{4.22b}$$

From Eq. (4.22a), $\boldsymbol{H}$ can be expressed as

$$\boldsymbol{H}_0 = \boldsymbol{\mu}^{-1}\left(\mathbf{m}^{\times}\boldsymbol{E}_0 + \mathrm{i}\boldsymbol{\alpha}^{\mathrm{T}}\boldsymbol{E}_0\right), \tag{4.23}$$

and by a substitution into (4.22b), $\boldsymbol{H}$ is eliminated. Following set of equations is therefore derivated:

$$\left[\boldsymbol{\varepsilon} + \mathbf{m}^{\times}\boldsymbol{\mu}^{-1}\mathbf{m}^{\times} + \mathrm{i}\left(\boldsymbol{\alpha}\boldsymbol{\mu}^{-1}\mathbf{m}^{\times} + \mathbf{m}^{\times}\boldsymbol{\mu}^{-1}\boldsymbol{\alpha}^{\mathrm{T}}\right) - \boldsymbol{\alpha}\boldsymbol{\mu}^{-1}\boldsymbol{\alpha}^{\mathrm{T}}\right]\boldsymbol{E}_0 \equiv \mathbf{X}\boldsymbol{E}_0 = 0. \tag{4.24}$$

Fedorov proved [95] following identity:

$$\boldsymbol{\alpha}\boldsymbol{\mu}^{-1}\mathbf{m}^{\times} + \mathbf{m}^{\times}\boldsymbol{\mu}^{-1}\boldsymbol{\alpha}^{\mathrm{T}} \equiv (\mathbf{g}\boldsymbol{m})^{\times}, \tag{4.25}$$

or alternatively [95, 101, 103]

$$\boldsymbol{G} = \left[\mathrm{tr}\left(\boldsymbol{\mu}^{-1}\alpha^{\mathrm{T}}\right)\mathbf{I} - \boldsymbol{\mu}^{-1}\alpha^{\mathrm{T}}\right]\boldsymbol{m} = \mathbf{g}\boldsymbol{m}, \tag{4.26}$$

where $\mathbf{I}$ is the identity matrix, $\mathbf{g}$ is the gyration tensor, and $\boldsymbol{G}$ is the gyration vector introduced in Born-Landau (Yeh) formalism (4.1). The gyration vector is in a relation with gyration scalar parameter G:

$$\boldsymbol{G} = G\boldsymbol{n} \tag{4.27}$$

The Eq. (4.24) can be therefore rewriten as

$$\left[\boldsymbol{\varepsilon} + \mathbf{m}^{\times}\boldsymbol{\mu}^{-1}\mathbf{m}^{\times} + \mathrm{i}\,(\mathbf{g}\boldsymbol{m})^{\times} - \boldsymbol{\alpha}\boldsymbol{\mu}^{-1}\boldsymbol{\alpha}^{\mathrm{T}}\right]\boldsymbol{E}_0 \equiv \mathbf{X}\boldsymbol{E}_0 = 0. \tag{4.28}$$

To obtain a nontrivial solution of (4.24) [or equivalently (4.28)], the determinant of $\mathbf{X}$ must be equal zero. If we consider nonmagnetic media only, and we apply the tensor symmetries (4.9), the components of the determinant

$$\det(\mathbf{X}) = \begin{vmatrix} X_{11} & X_{12} & X_{13} \\ X_{21} & X_{22} & X_{23} \\ X_{31} & X_{32} & X_{33} \end{vmatrix}, \tag{4.29}$$

can be derived as follows:

$$
\begin{aligned}
X_{11} &= \varepsilon_{11} - \left(m_2^2 + m_3^2\right) + \left(\alpha_{11}^2 + \alpha_{12}^2 + \alpha_{13}^2\right), \\
X_{12} &= \varepsilon_{12} + (m_1 m_2) + \mathrm{i}\,[\alpha_{13} m_1 + \alpha_{22} m_2 + (\alpha_{21} - \alpha_{11}) m_3] + (-\alpha_{11}\alpha_{12} + \alpha_{12}\alpha_{22} + \alpha_{13}\alpha_{23}), \\
X_{13} &= \varepsilon_{13} + (m_1 m_3) + \mathrm{i}\,[-\alpha_{12} m_1 + (\alpha_{11} + \alpha_{33}) m_2 + \alpha_{23} m_3] + (-\alpha_{11}\alpha_{13} - \alpha_{12}\alpha_{23} + \alpha_{13}\alpha_{33},) \\
X_{21} &= \varepsilon_{21} + (m_1 m_2) + \mathrm{i}\,[-\alpha_{13} m_1 - \alpha_{23} m_2 + (\alpha_{11} + \alpha_{22}) m_3] + (-\alpha_{11}\alpha_{12} - \alpha_{12}\alpha_{22} + \alpha_{13}\alpha_{23}), \\
X_{22} &= \varepsilon_{22} - \left(m_1^2 + m_3^2\right) + \left(\alpha_{12}^2 + \alpha_{22}^2 + \alpha_{23}^2\right), \\
X_{23} &= \varepsilon_{23} + (m_2 m_3) - \mathrm{i}\,[(\alpha_{22} + \alpha_{33}) m_1 + \alpha_{12} m_2 + \alpha_{13} m_3 +] + (\alpha_{12}\alpha_{13} - \alpha_{22}\alpha_{23} + \alpha_{23}\alpha_{33}), \\
X_{31} &= \varepsilon_{13} + (m_1 m_3) + \mathrm{i}\,[\alpha_{12} m_1 - (\alpha_{11} + \alpha_{33}) m_2 - \alpha_{23} m_3] + (-\alpha_{11}\alpha_{13} - \alpha_{12}\alpha_{23} + \alpha_{13}\alpha_{33}), \\
X_{32} &= \varepsilon_{23} + (m_2 m_3) + \mathrm{i}\,[(\alpha_{22} + \alpha_{33}) m_1 + \alpha_{12} m_2 + \alpha_{13} m_3] + (\alpha_{12}\alpha_{13} - \alpha_{22}\alpha_{23} + \alpha_{23}\alpha_{33}), \\
X_{33} &= \varepsilon_{33} - \left(m_1^2 + m_2^2\right) + \left(\alpha_{13}^2 + \alpha_{23}^2 + \alpha_{33}^2\right).
\end{aligned}
$$

Solving the quartic equation

$$X_{11}X_{22}X_{33} + X_{13}X_{21}X_{32} + X_{12}X_{23}X_{31} - (X_{13}X_{22}X_{31} + X_{11}X_{23}X_{32} + X_{12}X_{21}X_{33}) = 0, \quad (4.30)$$

in terms of n leads to the solution of eigenmodes n_k, $k = \{1, 2, 3, 4\}$, propagating in particular media defined by tensors in (4.22). Note, that the analytical solution of the quartic equation for general media and arbitrary angle of incidence is very cumbersome. Therefore, it is convinient to solve the problem in a simplified form (e.g. normal incidence) and for a given symmetry of the media.

4.3 Effects of material symmetry

To classify the crystal lattice, 7 crystallographic (crystal) system are defined. The crystallographic systems are based on the fact, that every crystal is symmetric in some manner. The description is given by the symmetry elements: Symmetry axes (two, three, four and six-fold – labeled as 2, 3, 4, and 6, respectively), symmetry (mirror) plane m, inversion centre C and inversion symmetry axes labeled as a number with bar. The external shape of the crystal is called the *habit* and is given by a combination of basic crystal habits [104, 105]:

- **Pedion** – formed by one, unique plane.
- **Pinacoid** – two equivalent parallel and opposite faces symmetrical to 2-fold axis, symmetry plane or inversion cenre.
- **Sfenoid** – two nonparallel equivalent faces symmetrical to 2-fold symmetry axis.
- **Doma** – two nonparallel equivalent and opposite faces symmetrical to symmetry plane or 2-fold axis and symmetry plane.
- **Prism** – three or more equivalent planes intersecting in parallel edges.

- **Pyramid** – three or more equivalent planes intersecting in coomon apex.

All possible combinations of microscopic parameters form 230 space groups, without translation components 32 point groups, see Tab. 4.1.

The particular crystal symmetry affects the shape of the tensors in the constitutive relations (4.1)–(4.4). The crystallographic symmetry elements can be mathematically described using transformation matrix formalism. Every crystallographic symmetry operation can be uderstood as an operation, that transforms a set of points or a single point on itself. According to the Neumann's principle [106], *if any crystal is invariant to certain symmetry operations according to the crystal symmetry it belongs to, any physical property must also be invariant with respect to these symmetry operations.*

Here is an example: Consider the crystal class m (m is perpendicular to z). One possibility of the tensor transformation is using the rotation and mirror matrices. First, we take the most general form of tensor and apply the mirror matrix transforming z-axis into $-z$-axis. Comparing the resulting tensor with the most general form with respect to the Neumann's principle and tensor symmetries (4.16) we obtain the tensor for a particular crystal point group. This method requires matrix multiplication and is therefore lengthy.

Much more convenient way is to use the direct inspection method [107] introduced by Fumi [108]. Considering the same example of the crystal symmetry m. The transformation axes are

$$1 \to 1,\ 2 \to 2,\ 3 \to -3. \tag{4.31}$$

From the tensor symmetries (4.16) we have

$$\varepsilon_{ij} = \varepsilon_{ij},\ \mu_{ij} = \mu_{ij},\ \alpha_{ij} = -\alpha_{ji},\ g_{ij} = -g_{ji}. \tag{4.32}$$

Tensors $\boldsymbol{\varepsilon}$ and $\boldsymbol{\mu}$ are both transformed according to logic below:

$$\begin{bmatrix} \varepsilon_{11} & \varepsilon_{12} & \varepsilon_{13} \\ \varepsilon_{21} & \varepsilon_{22} & \varepsilon_{23} \\ \varepsilon_{31} & \varepsilon_{32} & \varepsilon_{33} \end{bmatrix} \xrightarrow{m\perp z,\, \varepsilon_{ij}=\varepsilon_{ji}} \begin{bmatrix} \varepsilon_{11} & \varepsilon_{12} & -\varepsilon_{13} \\ \varepsilon_{21} & \varepsilon_{22} & -\varepsilon_{23} \\ -\varepsilon_{31} & -\varepsilon_{32} & \varepsilon_{33} \end{bmatrix} \xrightarrow{\text{Neumann}} \begin{bmatrix} \varepsilon_{11} & \varepsilon_{12} & 0 \\ \varepsilon_{21} & \varepsilon_{22} & 0 \\ 0 & 0 & \varepsilon_{33} \end{bmatrix}. \tag{4.33}$$

Tensors $\boldsymbol{\alpha}$ and $\mathbf{g}$ are transformed in a following way:

$$\begin{bmatrix} g_{11} & g_{12} & g_{13} \\ g_{21} & g_{22} & g_{23} \\ g_{31} & g_{32} & g_{33} \end{bmatrix} \xrightarrow{m\perp z,\, g_{ij}=-g_{ji}} \begin{bmatrix} -g_{11} & -g_{12} & g_{13} \\ -g_{21} & -g_{22} & g_{23} \\ g_{31} & g_{32} & -g_{33} \end{bmatrix} \xrightarrow{\text{Neumann}} \begin{bmatrix} 0 & 0 & g_{13} \\ 0 & 0 & g_{23} \\ g_{31} & g_{32} & 0 \end{bmatrix}. \tag{4.34}$$

Using the same logic, the transformation of point group $\bar{4}$ is given:

$$1 \to 2,\ 2 \to -1,\ 3 \to -3, \tag{4.35}$$

and corresponding tensors are obtained:

$$\begin{bmatrix} \varepsilon_{11} & \varepsilon_{12} & \varepsilon_{13} \\ \varepsilon_{21} & \varepsilon_{22} & \varepsilon_{23} \\ \varepsilon_{31} & \varepsilon_{32} & \varepsilon_{33} \end{bmatrix} \xrightarrow{\bar{4},\, \varepsilon_{ij}=\varepsilon_{ji}} \begin{bmatrix} \varepsilon_{22} & -\varepsilon_{12} & -\varepsilon_{13} \\ -\varepsilon_{21} & \varepsilon_{11} & -\varepsilon_{23} \\ -\varepsilon_{31} & -\varepsilon_{32} & \varepsilon_{33} \end{bmatrix} \xrightarrow{\text{Neumann}} \begin{bmatrix} \varepsilon_{11} & 0 & 0 \\ 0 & \varepsilon_{11} & 0 \\ 0 & 0 & \varepsilon_{33} \end{bmatrix}, \tag{4.36}$$

$$\begin{bmatrix} g_{11} & g_{12} & g_{13} \\ g_{21} & g_{22} & g_{23} \\ g_{31} & g_{32} & g_{33} \end{bmatrix} \xrightarrow{\bar{4},\, g_{ij}=-g_{ji}} \begin{bmatrix} -g_{22} & g_{12} & -g_{23} \\ g_{12} & -g_{11} & -g_{13} \\ g_{32} & g_{31} & -g_{33} \end{bmatrix} \xrightarrow{\text{Neumann}} \begin{bmatrix} g_{11} & g_{12} & 0 \\ g_{12} & -g_{11} & 0 \\ 0 & 0 & 0 \end{bmatrix}. \tag{4.37}$$

Tensors for every other symmetry are obtained analogically. The summarization is given in Tab. 4.2.

The rotation of a crystal in a laboratory coordinate system xyz is given by a set of Euler angles φ, θ, ψ, which completely determines the orientation of rotated $x'y'z'$ system relative to xyz [109]. The rotation matrix is understood as a three consecutive transformation. First, rotation in xy-plane by the angle φ produces new coordinate system XYz, in which the rotation in Yz-plane about the angle φ is performed. In resulting XYZ system, last rotation in XY-plane about the angle ψ produces the resulting $x'y'z'$ coordinate system. The rotation matrix $\mathbf{R}$ is then

$$\mathbf{R} = \begin{bmatrix} \cos\psi\cos\varphi - \cos\theta\sin\varphi\sin\psi & \cos\psi\sin\varphi + \cos\theta\cos\varphi\cos\psi & \sin\psi\sin\theta \\ -\sin\psi\cos\varphi - \cos\theta\sin\varphi\cos\psi & -\sin\psi\sin\varphi + \cos\theta\cos\varphi\cos\psi & \cos\psi\sin\theta \\ \sin\theta\sin\varphi & -\sin\theta\cos\varphi & \cos\theta \end{bmatrix}, \tag{4.38}$$

and since $\mathbf{R}$ is Hermitean, $\mathbf{R}^{-1} = \mathbf{R}^{\mathrm{T}}$.

Now, having the symmetries defined, we can define a general expression for the gyration scalar parameter G introduced in (4.27) with respect to the gyration tensor $\boldsymbol{g}$, which is defined for every crystal symmetry in Tab. 4.2:

$$G = g_{11}\boldsymbol{\theta}_{\mathbf{1}}^2 + g_{22}\boldsymbol{\theta}_{\mathbf{2}}^2 + g_{33}\boldsymbol{\theta}_{\mathbf{3}}^2 + (g_{12}+g_{21})\boldsymbol{\theta}_{\mathbf{1}}\boldsymbol{\theta}_{\mathbf{2}} + (g_{13}+g_{31})\boldsymbol{\theta}_{\mathbf{1}}\boldsymbol{\theta}_{\mathbf{3}} + (g_{23}+g_{32})\boldsymbol{\theta}_{\mathbf{2}}\boldsymbol{\theta}_{\mathbf{3}}, \tag{4.39}$$

where $\boldsymbol{\theta}_{\mathbf{1,2,3}}$ are direction cosines in 123 coordinate system. For example, if we choose Cartesian coordinate system, we obtain $1 \to x$, $2 \to y$, and $3 \to z$.

Table 4.1: 32 crystal symmetry classes. Every crystal belongs to one of these.

Crystal system	Hermann-Maugin symbol	Dominant habit	Chirality
Triclinic	1	Pedial	Yes
	$\bar{1}$	Pinacoidal	No
Monoclinic	2	Sphenoidal	Yes
	m	Domatic	Yes
	$2/m$	Prismatic	No
Orthorombic	222	Rhombic-Disphenoidal	Yes
	$mm2$	Rhombic-Pyramidal	Yes
	$2/m\,2/m\,2/m\,(mmm)$	Rhombic-Dipyramidal	No
Tetragonal	4	Tetragonal-Pyramidal	Yes
	$\bar{4}$	Tetragonal-Disphenoidal	Yes
	$4/m$	Tetragonal-Dipyramidal	No
	422	Tetragonal-Trapezoidal	Yes
	$4mm$	Ditetragonal-Pyramidal	No
	$\bar{4}2m$	Tetragonal-Scalenohedral	Yes
	$4/m\,4/m\,4/m\,(4/mmm)$	Ditetragonal-Dipyramidal	No
Trigonal	3	Trigonal-Pyramidal	Yes
	$\bar{3}$	Rhombohedral	No
	32	Trigonal-Trapezohedral	Yes
	$3m$	Ditrigonal-Pyramidal	No
	$4\bar{3}\,2/m\,(\bar{3}m)$	Hexagonal-Scalenohedral	No
Hexagonal	6	Hexagonal-Pyramidal	Yes
	$\bar{6}$	Trigonal-Dipyramidal	No
	$6/m$	Hexagonal-Dipyramidal	No
	622	Hexagonal-Trapezohedral	Yes
	$6mm$	Dihexagonal-Pyramidal	No
	$\bar{6}2m$	Ditrigonal-Dipyramidal	No
	$6/m\,2/m\,2/m\,(6/mmm)$	Dihexagonal-Dipyramidal	No
Cubic	23	Tetaroidal	Yes
	$2/m\bar{3}$	Diploidal	No
	432	Gyroidal	Yes
	$\bar{4}3m$	Hextetrahedral	No
	$4/m\,\bar{3}\,2/m$	Hexoctahedral	No

Table 4.2: Tensor symmetries of every point group. Note, that $\boldsymbol{\mu}$ and $\boldsymbol{\varepsilon}$, and $\mathbf{g}$ and $\boldsymbol{\alpha}$ symmetries are, respectively, equal.

Crystal symmetry	Dielectric tensor $\boldsymbol{\varepsilon}$	Point group	Gyration tensor $\mathbf{g}$
Triclinic	$\begin{bmatrix} \varepsilon_{11} & \varepsilon_{12} & \varepsilon_{13} \\ \varepsilon_{21} & \varepsilon_{22} & \varepsilon_{23} \\ \varepsilon_{31} & \varepsilon_{32} & \varepsilon_{33} \end{bmatrix}$	$\bar{1}$	$\begin{bmatrix} g_{11} & g_{12} & g_{13} \\ g_{21} & g_{22} & g_{23} \\ g_{31} & g_{32} & g_{33} \end{bmatrix}$
Monoclinic	$\begin{bmatrix} \varepsilon_{11} & \varepsilon_{12} & 0 \\ \varepsilon_{21} & \varepsilon_{22} & 0 \\ 0 & 0 & \varepsilon_{33} \end{bmatrix}$	2	$\begin{bmatrix} g_{11} & g_{12} & 0 \\ g_{21} & g_{22} & 0 \\ 0 & 0 & g_{33} \end{bmatrix}$
		m	$\begin{bmatrix} 0 & 0 & g_{13} \\ 0 & 0 & g_{23} \\ g_{31} & g_{32} & 0 \end{bmatrix}$
Orthorombic	$\begin{bmatrix} \varepsilon_{11} & 0 & 0 \\ 0 & \varepsilon_{22} & 0 \\ 0 & 0 & \varepsilon_{33} \end{bmatrix}$	222	$\begin{bmatrix} g_{11} & 0 & 0 \\ 0 & g_{22} & 0 \\ 0 & 0 & g_{33} \end{bmatrix}$
		$mm2$	$\begin{bmatrix} 0 & g_{12} & 0 \\ g_{21} & 0 & 0 \\ 0 & 0 & 0 \end{bmatrix}$
Tetragonal	$\begin{bmatrix} \varepsilon_{11} & 0 & 0 \\ 0 & \varepsilon_{11} & 0 \\ 0 & 0 & \varepsilon_{33} \end{bmatrix}$	4, 422	$\begin{bmatrix} g_{11} & 0 & 0 \\ 0 & g_{11} & 0 \\ 0 & 0 & g_{33} \end{bmatrix}$
		$\bar{4}$	$\begin{bmatrix} g_{11} & g_{12} & 0 \\ g_{12} & -g_{11} & 0 \\ 0 & 0 & 0 \end{bmatrix}$
		$4mm$	$\begin{bmatrix} 0 & g_{12} & 0 \\ -g_{12} & 0 & 0 \\ 0 & 0 & 0 \end{bmatrix}$
		$\bar{4}2m$	$\begin{bmatrix} g_{11} & g_{12} & 0 \\ g_{12} & -g_{11} & 0 \\ 0 & 0 & 0 \end{bmatrix}$
Trigonal and Hexagonal	$\begin{bmatrix} \varepsilon_{11} & 0 & 0 \\ 0 & \varepsilon_{11} & 0 \\ 0 & 0 & \varepsilon_{33} \end{bmatrix}$	3, 32, 6, 622	$\begin{bmatrix} g_{11} & 0 & 0 \\ 0 & g_{11} & 0 \\ 0 & 0 & g_{33} \end{bmatrix}$
		$3m$, $6mm$	$\begin{bmatrix} 0 & g_{12} & 0 \\ -g_{12} & 0 & 0 \\ 0 & 0 & 0 \end{bmatrix}$
Cubic	$\begin{bmatrix} \varepsilon_{11} & 0 & 0 \\ 0 & \varepsilon_{11} & 0 \\ 0 & 0 & \varepsilon_{11} \end{bmatrix}$	23	$\begin{bmatrix} g_{11} & 0 & 0 \\ 0 & g_{11} & 0 \\ 0 & 0 & g_{33} \end{bmatrix}$
		432	$\begin{bmatrix} g_{11} & 0 & 0 \\ 0 & g_{11} & 0 \\ 0 & 0 & g_{11} \end{bmatrix}$

5 Chirality in non-crystalline biisotropic media: liquids

In Chapter 3 we have seen, that the measurements of optically active solutions in order to obtain specific rotatory powers have been always in the scope of the scientist. Those measurements have a huge imperfection, because they are still being performed using polarimeters operating at a single wavelength. In this Chapter, we present a novel technique of rotatory power measurements using Mueller matrix ellipsometry. The advantages and capabilities of this method will be demonstrated on water solutions of simple saccharides.

5.1 Eigenmodes propagating in chiral liquids

The constitution equations (4.17) are generally valid for an arbitrary bianisotropic medium. It is not surprising, that the liquids possess no crystal symmetry. However, optically active solutions exhibit the additional effect of the chirality and thus, they can not be characterized as a classic isotropic media. We call these media *biisotropic* [110]. The constitutive relations for biisotropic non-magnetic media have the form

$$\boldsymbol{D} = \varepsilon \boldsymbol{E}_0 + \mathrm{i}\alpha \boldsymbol{H}_0, \tag{5.1a}$$

$$\boldsymbol{B} = \boldsymbol{H}_0 - \mathrm{i}\alpha \boldsymbol{E}_0, \tag{5.1b}$$

where tensors $\boldsymbol{\varepsilon}$ and $\boldsymbol{\alpha}$ from (4.17) are substituted by scalars ε, α, respectively, and permeability tensor becomes a unit matrix ($\boldsymbol{\mu} = \mathrm{diag}\,[1\ 1\ 1]^{\mathrm{T}}$).

If we choose transmission straighthrough measurements in the Cartesian coordinate system, the incoming wave is propagating along the z-axis, therefore $\boldsymbol{n} = [0\ 0\ 1]^{\mathrm{T}}$. The determinant of Eq. (4.24) can be rewriten as

$$\left| \begin{bmatrix} \varepsilon & 0 & 0 \\ 0 & \varepsilon & 0 \\ 0 & 0 & \varepsilon \end{bmatrix} + \begin{bmatrix} 0 & -2\mathrm{i}n\alpha & 0 \\ 2\mathrm{i}n\alpha & 0 & 0 \\ 0 & 0 & 0 \end{bmatrix} + \begin{bmatrix} -n^2 & 0 & 0 \\ 0 & -n^2 & 0 \\ 0 & 0 & 0 \end{bmatrix} - \begin{bmatrix} \alpha^2 & 0 & 0 \\ 0 & \alpha^2 & 0 \\ 0 & 0 & 0 \end{bmatrix} \right| = 0, \tag{5.2}$$

leading to the biquadratic equation in terms of n with solutions

$$n_{1,2} = \sqrt{\varepsilon} \pm \alpha = n \pm \alpha. \tag{5.3}$$

The eigenmodes refractive indices n_1 and n_2 are related with the left-circular and right-circular polarized light, respectively, propagating in the chiral liquid. Refractive index n is the refraction index of the soution without the effect of chirality.

Note, that using constitutive relations (4.1) and Yeh's matrix formalism, given eigenvalue problem is leading to the equation [111]

$$\left(n^2 - n_1^2\right)\left(n^2 - n_2^2\right) = G^2, \tag{5.4}$$

with solution

$$n_{1,2} = n \pm \frac{G}{2n}. \tag{5.5}$$

Comparing the results obtained using Fedorov approach and Yeh approach, we immediately obtain equality

$$\alpha = \frac{G}{2n}. \tag{5.6}$$

This result is consistent with Eq. (4.25), because

$$\left(\boldsymbol{\alpha}\mathbf{m}^{\times} + \mathbf{m}^{\times}\boldsymbol{\alpha}^{\mathrm{T}}\right) = \begin{bmatrix} 2\alpha & 0 & 0 \\ 0 & 2\alpha & 0 \\ 0 & 0 & 2\alpha \end{bmatrix} \begin{bmatrix} 0 \\ 0 \\ n \end{bmatrix} = \begin{bmatrix} 0 \\ 0 \\ 2n\alpha \end{bmatrix} = \begin{bmatrix} 0 \\ 0 \\ G \end{bmatrix} = \mathbf{g}\boldsymbol{m}. \tag{5.7}$$

The gyration tensor $\boldsymbol{\alpha}$ is not very commonly used across the Western literature. Since those tensors are mutually convertible, the following models will be expressed in terms of $\mathbf{g}$ or equivalently in terms of G instead.

5.2 Chirality of simple saccharide diastereoisomers

The basic building block of every (complex) saccharide is a monosacharide. Molecule of a monosaccharide (monosugar) is formed by six-membered (pyranose) or five-membered (furanose) rings. Those rings can be attached together forming gradually a disaccharide, trisaccharide, attaching n rings together will form general polysaccharide. Note, that lower monosaccharides and lower forms of oligosaccharides (usually up to disaccharides) are loosely called sugars. Every molecule of a monosaccharide exists in three forms: α, open-chain, and β. The open-chain form of sugar contains carbonyl group (=O) attached to a carbon, which is called the *anomeric* carbon [46]. The absolute configuration of a molecule (see Fig. 5.1) is given by the position of the hydroxyl (OH) group attached to anomeric carbon with respect to $C^{5/6}$ (C^5 for fructofuranose, C^6 for glucopyranose) hydroxyl group. Antiperiplanar configuration of hydroxyl groups gives an α-anomer, while synperiplanar configuration stands for a β-anomer. The anomeric carbon is therefore asymmetric, and constitutes the chirality centre of a molecule. The role of the achiral open-chain form is the transition between α and β forms, which are chiral and its rotatory powers are different [112].

The reaction kinetics of sugars in solutions diametrically differs from the sugar kinetics in living organisms. For example, by melting (dissolving) of five-membered D-fructose, we get equilibrum solution of all other anomers, even the six-membered ones. For example, the equilibrum state of D-fructose water solution is 70 % of β-pyranose, 2 % α-pyranose, 23 % β-furanose, 5 % α-furanose and 0.7 % of an open-chain form [113]. However, solution of pure n-ring α-anomer will tend to the racemic mixture of n-ring α and β-anomers only. This effect is called the *mutarotation*, it was discovered in 1846 by Dubrunfaut on a glucose [114], and is temperature-dependent. For example, melting α-lactose at temperature higher then 93.5 °C, the

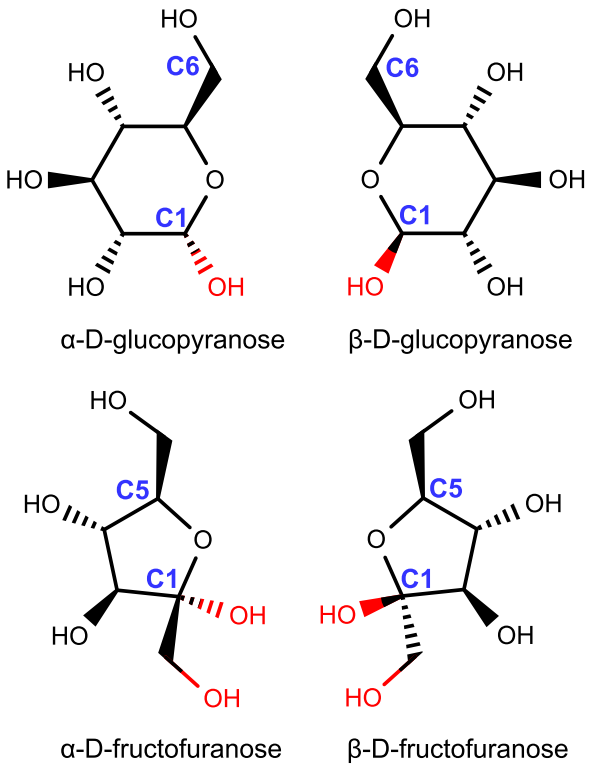

Figure 5.1: Diastereoisomers of glucose (glucopyranose) and fructose (fructofuranose). The difference between α and β forms is given by synperiplanaraity or antiperiplanarity of hydroxylic OH groups on anomeric carbon with respect to hydroxylic group on C^6 (glucose) or C^5 (fructose). The bold lines represent bonds facing towards the reader, dashed bonds opposite to reader. The two corresponding forms are arranged as their own mirror images. It is obvious, that those structures are chiral.

equilibrum of the solution is strongly shifted, and the resulting solution is composed mainly of lactose β-anomers [115].

5.3 Modelling the chiral liquids

The Mueller matrix spectroscopic ellipsometer (Woollam RC2-DI) with the spectral range from 193 nm to 1700 nm was set to the transmission configuration at normal angle of incidence for all experiments involving the optically active liquids. The measurement technique involves the solution of some optically active chemical compound poured in the glass cuvette with a cap. The cuvette is placed between PSG and PSA to the sample holder, and as the light beam passes through the optically active solution, the polarization plane rotation is detected.

The optical response is given by a Mueller matrix. If we take the rotation Jones matrix from Eq. (2.12), and apply transformation (2.16), the transmission Mueller matrix for optically active

solution is derived

$$\mathbf{M} = \begin{bmatrix} 1 & 0 & 0 & 0 \\ 0 & \cos 2\alpha_{\text{obs}} & \sin 2\alpha_{\text{obs}} & 0 \\ 0 & -\sin 2\alpha_{\text{obs}} & \cos 2\alpha_{\text{obs}} & 0 \\ 0 & 0 & 0 & 1 \end{bmatrix}. \tag{5.8}$$

The angle α_{obs} represents the observed angle of the polarization plane rotation. This quantity is dependent on the ammount of the chemical dissolved (represented by a concentration c) and on the length of the cuvette d – the longer the cuvette, the greater the observed rotation. Therefore, the quantity *specific rotatory power* (comp. to Eq. [3.1]) is defined for each compound as

$$[\alpha]_\lambda^T = \frac{\alpha_{\text{obs}}}{l\, c} \tag{5.9}$$

at given wavelength λ and temperature T. The spectral dependence of α_{obs} is given by

$$\alpha_{\text{obs}} = \frac{2\pi}{\lambda}\left(n_2 - n_1\right), \tag{5.10}$$

where the refractive indices $n_{1,2}$ are defined in Eq. (5.5). Substituting from (5.5), the measured quantities $2\alpha_{\text{obs}}$ in Mueller matrix (5.8) are given:

$$\alpha_{\text{obs}} = \frac{\pi G}{2n\lambda}, \tag{5.11}$$

where G is the scalar gyration parameter for a particular chiral liquid and n is the refraction index of the non-chiral solution. The dispersion model of solvent can be generally described using Sellmeier dispersion model (comp. [3.3]),

$$n^2(\lambda) = 1 + \sum_{i=1}^{N} \frac{A_i \lambda^2}{\lambda^2 - B_i^2}. \tag{5.12}$$

The dispersion of scalar gyration parameter (or gyration tensor component) was introduced by Arteaga *et al.* in [116, 117, 118]:

$$g_{ii}(\lambda) = G(\lambda) = \frac{\mathbb{A}_i \lambda^3}{\left(\lambda^2 - \mathbb{B}_i^2\right)^2}. \tag{5.13}$$

Its derivation is based on a quantum-mechanical model of rotatory power dispersion developed by Chandrasekar [119, 120]

$$\alpha_{\text{obs}} = \frac{\mathbb{A}_0 \lambda^2}{\left(\lambda^2 - \mathbb{B}^2\right)^2}, \tag{5.14}$$

which was experimentally validated many times. Considering Eq. (5.11), the dispersion model (5.13) is found easily from (5.14).

5.4 Ellipsometric measurements of saccharide solutions

To demonstrate the viability of proposed method, the measurements of basic and well-known chemical compounds were conducted. The simple saccharides – **glucose** (Glc), **fructose** (Fruf) and **sucrose** (Sach) – belong among the best explorated compounds in terms of optical activity and their specific rotatory powers (at $\lambda = 589\,\mathrm{nm}$) are commonly tabelated. This fact gives us a good reference frame, whether our measurements are valid or not.

Distilled water from Verkon, 99% D-(+)-Glucose, 99% D-(−)-Fructose and 99% D-(+)-Sucrose from Lachner were used for the experiment. For each sugar, concentration of $c = 0.25\,\mathrm{mol/dm^3} \equiv 0.25\,\mathrm{M}$ was chosen, as it is a good compromise between getting a reasonable optical response and avoiding the dispersion changes. The solutions were prepared according to fundamental equation

$$m = cMV, \tag{5.15}$$

where m is the mass of the saccharide, M is the saccharide molar mass, and V is the solution volume. Prepared solutions were measured after at least 4 hours from the preparation to ensure the termination of any eventual mutarotation effects. Note, that in practice, sugars are almost infinitely miscible with water, and such a solutions are very dense and inhomogenous – an example of such a natural solution is well known to everyone[20]. The high density could possibly lead to the inhomogenity of the solution, and the gyration parameter could not be obtained precisely.

From obtained Mueller matrix spectra, wavelength range from 350 nm to 1140 nm was treated. UV region is cut short due to glass absorption and NIR region due to molecular vibrations and signal losing. The calculations were performed on m_{23} and m_{32} elements only, because at given relatively small concentrations of solutions, the observed polarization rotation is not bigger then $\pm 5°$. Therefore, m_{22} and m_{33} cosine elements are at their extremas, and are insufficiently sensitive. On the contrary, m_{23} and m_{32} are at their inflex points and are therefore very sensitive. The typical experimental Mueller matrix of chiral solution is showed in Fig. 5.2. These experimental data are obtained from the measurements of extremely concentrated glucose solution.

The spectra of m_{23}, m_{32} elements were fitted by a dispersion model given by (5.11) and (5.13). The refractive index of water was taken tabelated (according to the laboratory temperature) from [121] in the form of four-term Sellmeier dispersion model. Fitted parameters of $G(\lambda)$ dispersion for each compound are summarized in Tab. 5.1. Strictly speaking, the dispersion of the water refractive index is changed with addition of the sugar regardless the chirality. It was shown [122], that those changes are below 1 % for solutions up to 5 % analyte to solvent mass ratio. The concentration of 0.25 M corresponds to approx. 4.5 % analyte to solvent mass ratio. Therefore, it is justifiable to use tabelated water dispersion. From the models, the corresponding values of $[\alpha]_\lambda^{22}$ were calculated using (5.9). Figure 5.3 shows the fitted dispersion of $G(\lambda)$ and calculated

[20] *"**Honey**, do you love me, huh?"* Hank Williams, Sr.

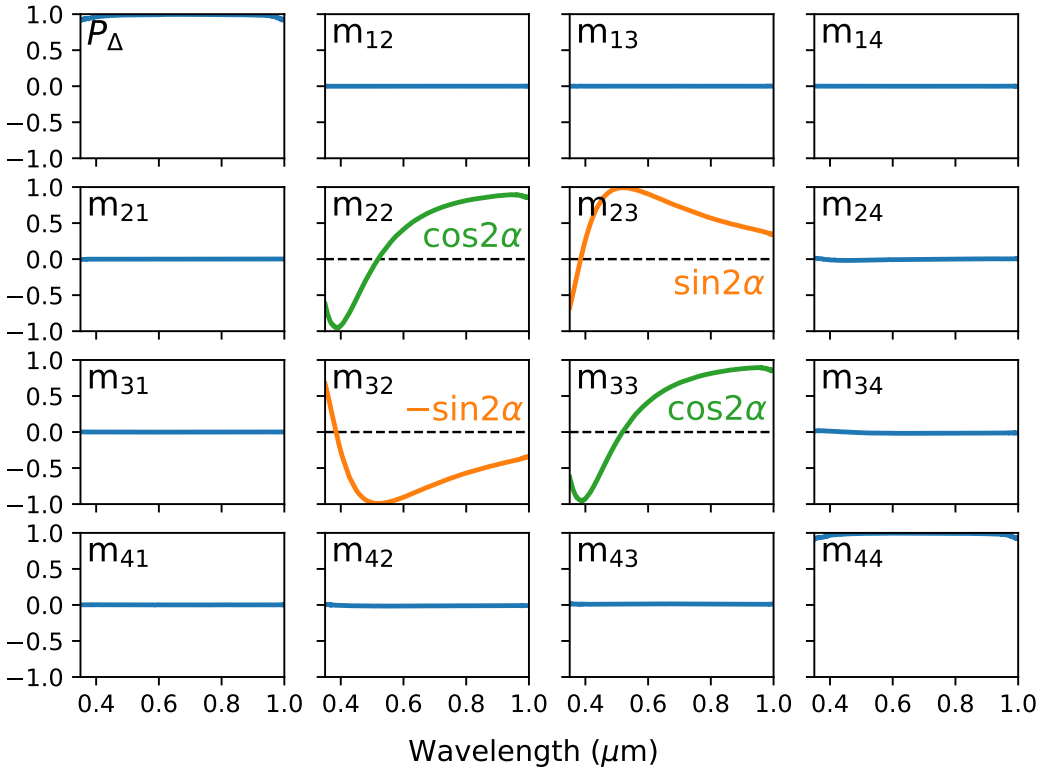

Figure 5.2: Typical experimental transmission Mueller matrix of highly concentraed chiral liquid.

Table 5.1: Fitted parameters of $G(\lambda)$ dispersion at 22°C with λ in nanometers.

Compound	$\mathbb{A}$	$\mathbb{B}$
D-(+)-Glc	0.01173	0.12310
D-(−)-Fruf	−0.01926	0.11140
D-(+)-Sach	0.02696	−0.11404

spefici rotatory powers $[\alpha]_{22}^{T}$ for each sugar. Note, that the dispersion curves $[\alpha]_{\lambda}^{22}$ (λ) for Glucose and Sucrose show similar values of specific rotation. However, corresponding dispersion curves of $G(\lambda)$ show, that the response of Sucrose is approximately *double* as the Glucose response. This is due to different M values of Glucose and Sucrose. To prepare 0.25 M solution of both the saccharides, *double ammount* of Sucrose must be dissolved in comparison with Glucose. The tabulated values of $[\alpha]_{\lambda}^{22}$ are usually given for $\lambda = 589\,\mathrm{nm}$, therefore, values $[\alpha]_{589}^{22}$ are highlighted and they are in a good match with the tabelated values, see Tab. 5.2. The slight missmatch between the experimental and tabulated values is due to: First, experimental and tabulated values were measured at mildly different temperatures. Second, the impact of an imperfect preparation of the solution – concentration deviations originating in approximate reading of the

volume values at volumetric flask together with the errors from weighing. We have already showed these basic Mueller matrix spectroscopic measurements published in [127].

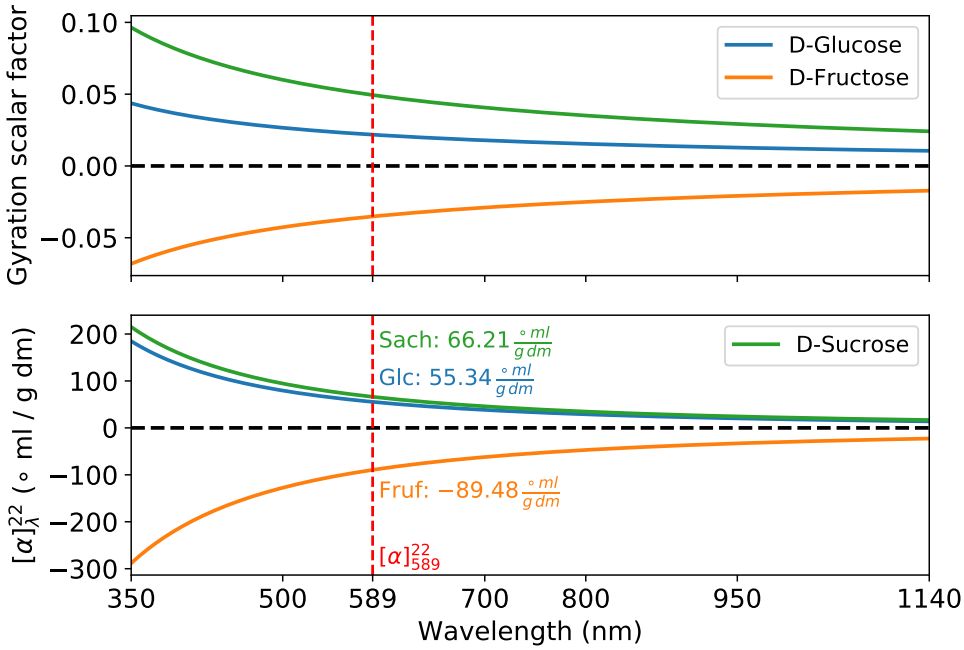

Figure 5.3: Modelled spectral dependencies of the specific rotatory power $[\alpha]^{22}_{\lambda}$ and scalar gyration parameter G of D-Glucose, D-Fructose, and D-Sucrose. To compare the fitted values with the literature, the values for $\lambda = 589\,\text{nm}$ are shown.

Table 5.2: Comparison of specific rotations obtained by our experiment with tabelated values.

Compound	Exp: $[\alpha]^{22}_{589}$	Tab: $[\alpha]^{20}_{589}$ [123]
D-(+)-Glc	55.34	52.70
D-(−)-Fruf	−89.48	−92.00
D-(+)-Sach	66.21	66.37

According to the CompleteEASE manual [128], the Mueller matrix element sensitivity is 0.001. Assuming that in theory, the value of $m_{ij} = 0.001$ is the lowest value, at which the signal can be distinguished from the noise, the theoretical minimal detectable concentration of chiral compound in solution can be determined. The precision of the analytical scales is $\pm 0.001\,\text{g}$, and the volumetric flask is calibrated to $25\,\text{ml} \pm 0.01\,\text{ml}$. The ultimate sensitivity and precision of proposed method for a particular chemical compound can be therefore determined. The minimal concentrations c_{min} and corresponding errors Δc caused by the preparation technique are given in Tab. 5.3.

Table 5.3: The theoretical ultimate sensitivity of the proposed method. Experimental errors are raised due to the solution preparation technique.

Solution	$c_{\min} \pm \Delta c$ (mmol/dm^3)
D-(+)-Glc	12.0 ± 2.5
D-(−)-Fruf	6.8 ± 2.5
D-(+)-Sach	5.0 ± 2.5

5.5 Mutarotation kinetics

The kinetics of a chemical reaction is usually computed for *concentrations* of reactants. Since we know, that the concentration c is proportional to specific rotatory power $[\alpha]$, the reaction kinetics can be expressed in terms of $[\alpha]$. Please make note, that for following purposes, the symbol $[\alpha]$ will stand for a specific rotatory power of α-D-Glucose, and $[\beta]$ for a specific rotatory power of β-D-Glucose.

The mutarotation rate equation is described by the reverse reaction in the form

$$\alpha\text{-D-Glucose} \underset{\mathrm{k}_{\Leftarrow}}{\overset{\mathrm{k}_{\Rightarrow}}{\rightleftharpoons}} \beta\text{-D-Glucose}, \tag{5.16}$$

where $k_{\Rightarrow}$ is the forward mutarotation rate constant and $k_{\Leftarrow}$ is the reverse mutarotation rate constant. The reaction kinetics is given by first-order differential equation [124, 125, 126]

$$\frac{\mathrm{d}\,[\alpha]}{\mathrm{d}t} = -\frac{\mathrm{d}\,[\beta]}{\mathrm{d}t} = k_{\Rightarrow}\,[\alpha] - k_{\Leftarrow}\,[\beta]\,, \tag{5.17}$$

with boundary conditions

$$[\beta]_{t=0} = 0, \tag{5.18a}$$

$$[\alpha]_{t=0} = [\alpha]_0\,. \tag{5.18b}$$

In any time t, $[\beta] = [\alpha]_0 - [\alpha]$ is satisfied. Substituting into (5.17), we get

$$\frac{\mathrm{d}\,[\alpha]}{\mathrm{d}t} = (k_{\Rightarrow} + k_{\Leftarrow})\,[\alpha] + k_{\Leftarrow}\,[\alpha]_0\,. \tag{5.19}$$

If we assume an equilibrium state of the reaction ($\mathrm{d}\,[\alpha]\,/\mathrm{d}t = 0$), the equilibrium rotatory power of α-anomer can be directly calculated:

$$[\alpha]_{\mathrm{eq}} = \frac{k_{\Leftarrow}}{k_{\Rightarrow} + k_{\Leftarrow}}\,[\alpha]_0\,. \tag{5.20}$$

Substituting back into (5.19), following equation is calculated straightforwardly:

$$\frac{\mathrm{d}\,[\alpha]}{[\alpha]-[\alpha]_{\mathrm{eq}}} = (k_{\Rightarrow}+k_{\Leftarrow})\,\mathrm{d}t. \tag{5.21}$$

After integration and performing exponentiation, we get

$$[\alpha] = C\mathrm{e}^{-(k_{\Rightarrow}+k_{\Leftarrow})t} + [\alpha]_{\mathrm{eq}}\,, \tag{5.22}$$

where the integration constant C can be directly determined from (5.18b), which provides us with the resulting formula

$$[\alpha] = [\alpha]_{\mathrm{eq}} + \Big([\alpha]_0 - [\alpha]_{\mathrm{eq}}\Big)\,\mathrm{e}^{-kt}, \tag{5.23}$$

where the total rate constant k

$$k \equiv k_{\Rightarrow} + k_{\Leftarrow}, \tag{5.24}$$

was introduced. By substituting (5.23) into (5.19) and assuming (5.24), relation between forward, reverse and total rate constants are derived as follows:

$$k_{\Leftarrow} = \frac{[\alpha]_{\mathrm{eq}}}{[\alpha]_0}k, \tag{5.25a}$$

$$k_{\Rightarrow} = k - k_{\Leftarrow} = \left(1 - \frac{[\alpha]_{\mathrm{eq}}}{[\alpha]_0}\right)k. \tag{5.25b}$$

Distilled water from Verkon and 96% α-D-Glucose from Sigma were used for the experiment. The chemicals were left intact in well-tempered laboratory ($t = 25\,^{\circ}\mathrm{C}$) to guarantee the temperature stability. 1.126 g of α-D-Glucose was dissolved in 25 ml of distilled water. The freshly prepared solution was poured into the 5.004 cm long glass cuvette with cap. The first measurement was conducted after 5 minutes from the solution preparation. For the first 70 minutes, the measurements were repeated within a 5 min span, and within a 10 min span after that. The last measurement was performed 160 min after the solution preparation.

The spectral dependencies of calculated specific rotatory powers were fitted all together using model given by Eq. (5.23). The comparison between data and model are showed in Fig. 5.4 for the wavelength $\lambda = 589\,\mathrm{nm}$. The mutarotation rate constants were calculated using equations (5.24) and (5.25). The obtained values are in a quite good agreement with literature [129, 130], see Tab. 5.4. Note, that in Ref. [129], the part of the discussion included the influence of wavelength used

Table 5.4: α-β Glucose mutarotation rate constant comparison.

Constant (s^{-1})	This work (25 °C)	Kendrew *et al.* (20 °C) [130]	Lin *et al.* (22 °C) [129]
k	$3.531 \cdot 10^{-4}$	$2.473 \cdot 10^{-4}$	$7.670 \cdot 10^{-5}$
$k_{\Rightarrow}$	$2.033 \cdot 10^{-4}$	$9.028 \cdot 10^{-5}$	$2.760 \cdot 10^{-5}$
$k_{\Leftarrow}$	$1.498 \cdot 10^{-4}$	$1.570 \cdot 10^{-4}$	$4.910 \cdot 10^{-5}$

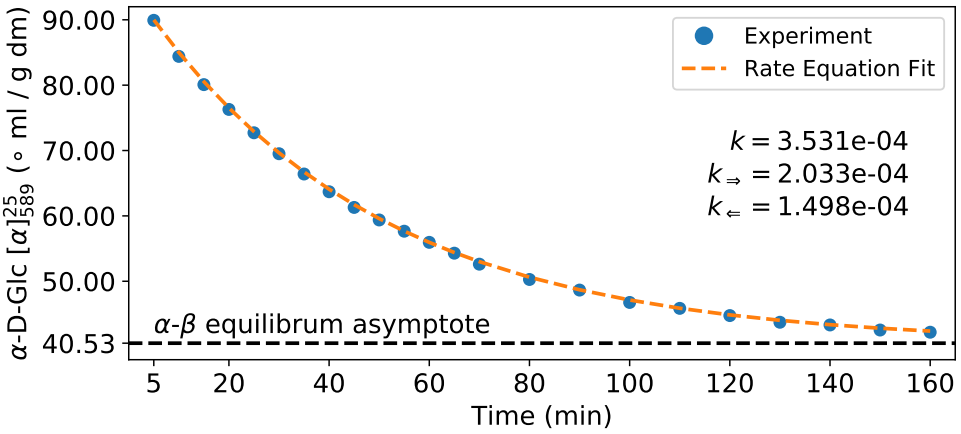

Figure 5.4: The change in the concentration of α Glucose anomer over time. The mutarotation rate constants are obtained from the exponential fit. The horizontal asymptote corresponds to the equilibrium state between α and β anomer.

for the analysis. We would like to emphasize, that it really does not matter, what wavelength of light (in non-absorbing region of the molecule) is chosed – the mutarotation kinetics must remain the same. This is a huge strength of our ellipsometric method of this measurement. The rate constants are calculated from a hundreds of spectral points and are therefore obtained with much better precision in a contrast with a single wavelength measurements, which are, to our knowledge, the only measurements, which have been conducted so far.

5.6 Temperature-dependent measurements

One important way of saccharide classification is whether they are *reducing* or *non-reducing*. The majority of saccharides contains an aldehyde group (CH-O) or a ketone group (C=O) in its structure. If those groups are present in an arbitrary chemical structure, it can be oxidized to carboxylic acid, while other reactant is being reduced. Saccharides, that contain the carbonyle group (aldehyde or ketone group) are called reducing, and sugars that does not contatin the carbonyle group are called non-reducing. The carbonyle group is giving a possibility to open the closed chain of the saccharide and thus the saccharide can switch between its α and β form (see and compare with Sec. 5.2). These saccharides therefore undergo mutarotation effects. An example of sucrose and lactose is given in Fig. 5.5.

For the temperature controlled measurements, we modified the sample holder of commercial Woollam RC2-DI Mueller matrix ellipsometer using our homemade, partly 3D-printed apparatus. The complete scheme is shown in Fig. 5.6 and the photography is shown in Fig. 5.7. The experimental setup is based on the heating control of the cuvette, which is placed between couple of Peltier devices. The heating power is controlled using 1 kW current generator with the current range of ±20 A. The actual temperature of the solution is detected by the Platinum temperature sensor PT100 connected to the digital thermometer with ±1 °C accuracy.

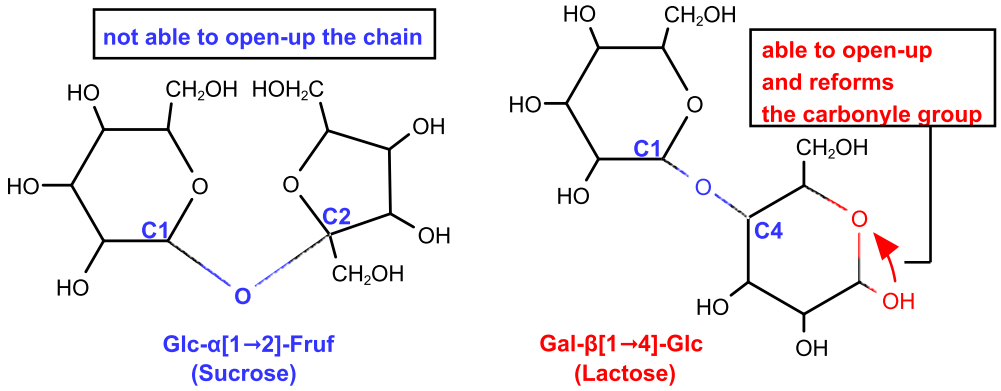

Figure 5.5: Sucrose is a disaccharide condensated from Glucose and Fructose. The glycosidic bond (–O–) attaches two rings together in such a manner, that there is no free hydroxyl OH group close enough to oxygen atom able to reforms a carbonyle group. Therefore, sucrose is a non-reducing sugar with no mutarotation. Lactose (Galactose-Glucose condensate) may exists in its α and β form due to oxidizing properties of the carbonyle group.

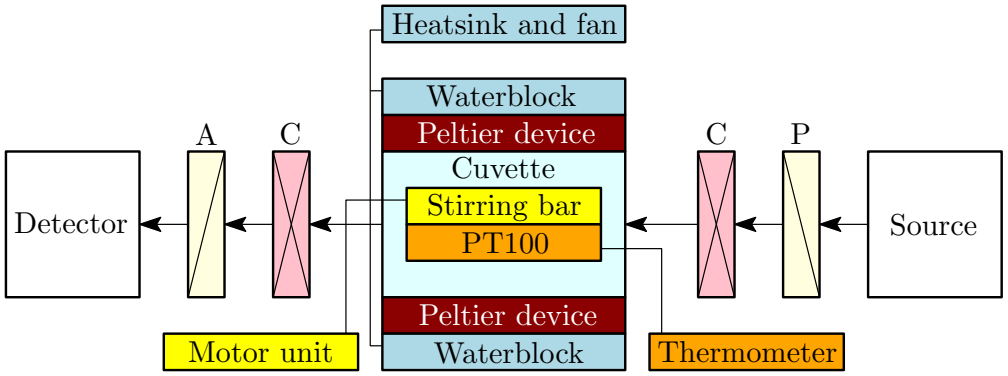

Figure 5.6: Mueller matrix ellipsometer experimental setup designed in our laboratoy for a temperature control measurements of optically active solutions.

To ensure the stability and viability of the experimental system, a test measurement on D-Sucrose was conducted. Sucrose is a non-reducing sugar with no mutarotation effects, therefore, the specific rotatory power of the sucrose solution must remain the same, if the temperature is changed. Concluding, the temperature-dependent measurements of the 0.25 M sucrose solution are very sensitive to any possible leakage of the vapours from the sealed cuvette, because if the concentration of the solution increases, specific rotatory power increases as well.

The temperature of the solution has been raising gradually with 5 A increment of the generator current. Figure 5.8 shows the spectral dependency of specific rotatory power over the temperature. For the estimation of the experimental errors, we have to redraw this figure into the special form. Figure 5.9 shows the Fig. 5.8 from the aerial view (bird's eye perspective). The values of $[\alpha]_\lambda^T$ are divided into a few equi-wavelength segments. The values of $[\alpha]_\lambda^T$ must remain the same as the temperature increases (dashed black verticals), however small deviations

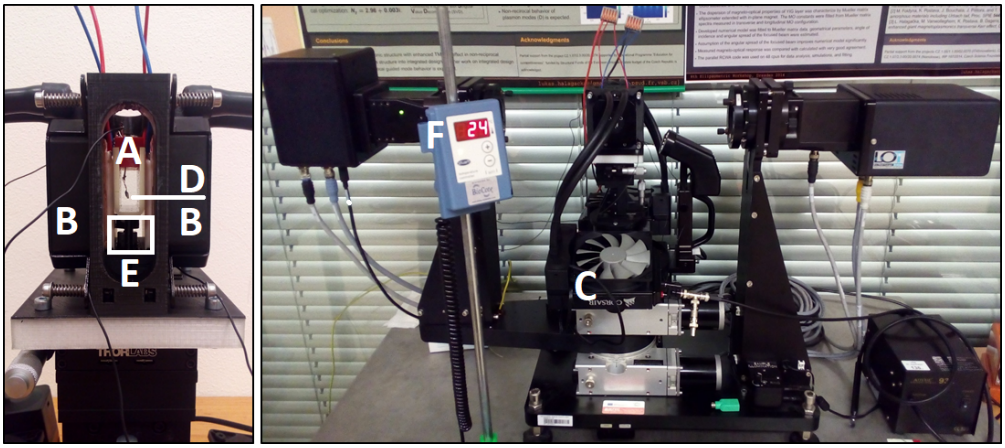

Figure 5.7: Photo of the homemade experimental setup. The cuvette (**A**) is placed between the couple of Peltier devices connected to the cooling waterblocks (**B**) to get rid of the junk heat through the heatsink with fan (**C**). To keep the solution homogenous (esp. at high temperatures and concentrations), the magnetic stirring bar is placed inside the cuvette and is rotated using the motor unit (**E**) with permanent magnet. The temperature is controlled using PT100 sensor (**D**) connected to digital thermometer (**F**).

are observed especially in the NIR region. This is due to a minor vapour leakage of the cuvette. Nevertheless, the maximum error in $[\alpha]_\lambda^T$ is less then 1 % and it was detected only for very high temperatures close to the solution boiling point (rapid evaporation).

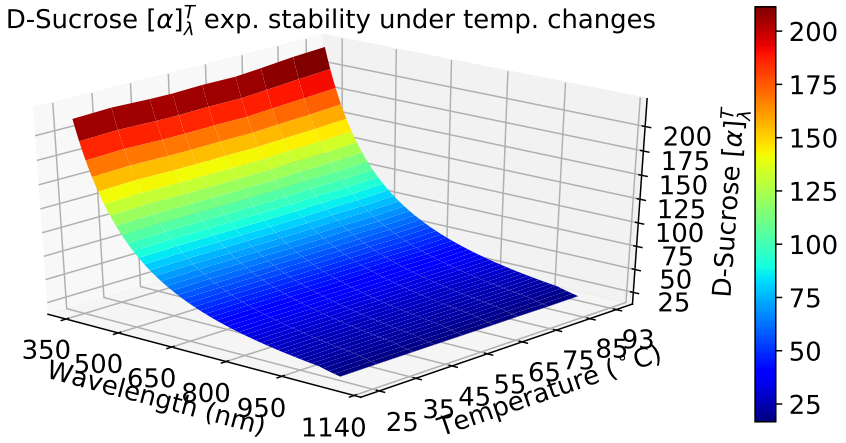

Figure 5.8: Specific rotatory power of non-reducing sucrose solution over the wavelength and the temperature.

The proposed method of the temperature-dependent specific rotatory power measurements seems to be a powerful and fast technique for the mutarotation kinetics determination. However, the apparatus hull is mainly composed of 3D-printed fragile plastics with low life excpectancy and together with the sealing imperfections, some experimental errors are raised. The manufacture of more rigid (e.g. duralumin) hull and more effective design of the cuvette sealing may be the

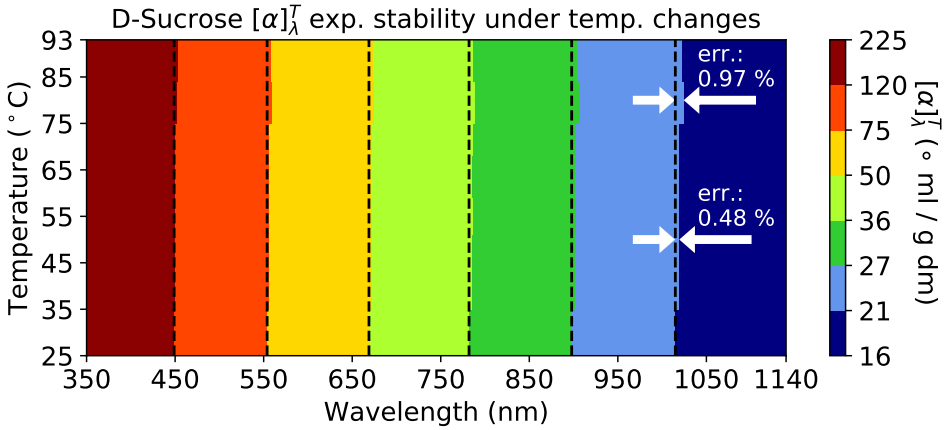

Figure 5.9: Specific rotatory power of non-reducing sucrose solution over the wavelength and the temperature. The vertical segments (dashed line) represent an ideal measurement without concentration changes. The experimental values of $[\alpha]^T_\lambda$ are not constant with increasing temperature especially within the NIR range, which indicates a vapour leakage from the cuvette. The maximum experimental error in $[\alpha]^T_\lambda$ is less then 1 %.

way, how to perform the chemical kinetics measurements reproducible way.

On the other hand, the proposed temperature control system offers unique and suitable way of temperature controlled measurements using temperature not too much close to the boiling point of used solution.

6 Chirality in non-absorbing media of the trigonal point group 32

The particular form of a dielectric tensor $\boldsymbol{\varepsilon}$ defines the principal axes of corresponding medium (crystal). The principal axes of a crystal are connected with the principal refraction indices. If those refraction indices are different ($n_{11} \neq n_{22} \neq n_{33}$), we call such a medium *biaxial*. If $n_{11} = n_{22} \neq n_{33}$, the crystal is *uniaxial*. Usually, the z axis of the unaxial crystal is called the *optic axis*, which is the unique direction in the crystal, in which no linear birefringence of propagating light occurs. Other directions leads to the linear birefringence effect, which causes the splitting of the incident monochromatic plane wave on the crystal boundary. Given a direction of the propagation in the medium, there exist two eigenwaves, each governed by a different index of refraction. In biaxial crystals, two optic axes are present.

From now on, we will discuss the uniaxial crystals only. Those crystals belong to tetragonal, trigonal and hexagonal crystal symmetries.

6.1 Propagating eigenmodes

The eigemodes propagating in uniaxial crystals must be evaluated with respect to the orientation of the crystal and the direction of propagating wave. Figure 6.1 shows two configurations, which will be evaluated next.

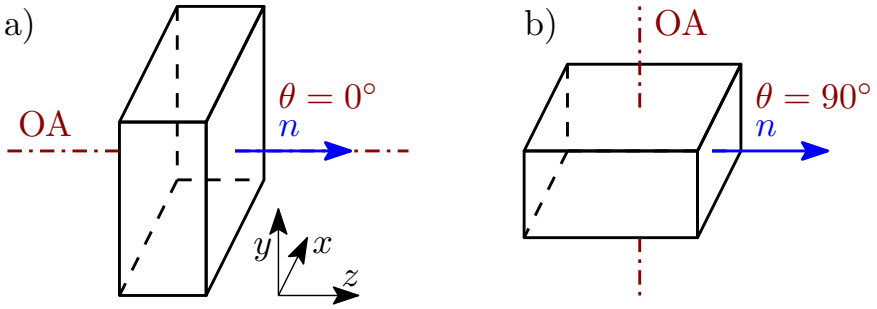

Figure 6.1: Two main configurations of the uniaxial crystal. The incident wave is given by the vector $\boldsymbol{n}$. The configuration **a)** shows the case, when light propagates parallel to the optic axis (OA). Case **b)** corresponds to the configuration, when the light passes perpendicular to the optic axis (angle between OA and $\boldsymbol{n}$ is given by $\theta = 90°$.)

6.1.1 Eigemnodes propagating parallel to optical axis

First, eigenmodes propagating parallel to optic axis will be derived. The material tensors for (non-magnetic) uniaxial crystal are (using Tab. 4.2)

$$\boldsymbol{\varepsilon} = \mathrm{diag}\left[\varepsilon_{11},\ \varepsilon_{11},\ \varepsilon_{33}\right],\ \boldsymbol{\alpha} = \mathrm{diag}\left[\alpha_{11},\ \alpha_{11},\ \alpha_{33}\right],\ \boldsymbol{\mu} = \mathrm{diag}\left[1,\ 1,\ 1\right]. \tag{6.1}$$

Eq. (4.24) with respect to (4.25) takes the form:

$$\left(\boldsymbol{\varepsilon} + \mathbf{m}^{\times}\mathbf{m}^{\times} + \mathrm{i}\,[\mathbf{g}\boldsymbol{m}]^{\times} - \boldsymbol{\alpha}\boldsymbol{\alpha}^{\mathrm{T}}\right)\boldsymbol{E}_0 = 0, \tag{6.2}$$

where

$$[\mathbf{g}\boldsymbol{m}]^{\times} = \left[\begin{bmatrix} \alpha_{11}+\alpha_{33} & 0 & 0 \\ 0 & \alpha_{11}+\alpha_{33} & 0 \\ 0 & 0 & 2\alpha_{11} \end{bmatrix}\begin{bmatrix} 0 \\ 0 \\ n \end{bmatrix}\right]^{\times} = \begin{bmatrix} 0 & -2n\alpha_{11} & 0 \\ 2n\alpha_{11} & 0 & 0 \\ 0 & 0 & 0 \end{bmatrix}. \tag{6.3}$$

Solving the determinant of (6.2) leads to the biquadratic equation

$$\left(\varepsilon_{33} - \alpha_{33}^2\right)\left[\left(\varepsilon_{11} - n^2 - \alpha_{11}^2\right)^2 - 4n^2\alpha_{11}^2\right] = 0, \tag{6.4}$$

from which the calculated eigenmodes ($k = \{1, 2, 3, 4\}$) propagating in the uniaxial crystal parallel to the optic axis $n_{k,\parallel}$ of the crystal are

$$n_{k,\parallel} = \pm n \pm \alpha_{11}. \tag{6.5}$$

Note, that if we turn off the optical activity ($\alpha_{11} = 0$), we get the solution for the isotropic medium, which is a correct solution, since the wave propagation coincide with the direction of the optic axis, and thus no birefringence occurs.

6.1.2 Eigenmodes propagating perpendicular to optical axis

The idea, how to calculate the eigenmodes propagating perpendicular to the optic axis is exactly the same, as in the case of the propagation parallel to the optic axis. Therefore, (6.2) can be applied. The normal incidence remains the same ($\boldsymbol{n} = [0,\ 0,\ n]^{\mathrm{T}}$), however, crystal orientation must be evaluated. Using the rotation matrix from (4.38) in the form

$$\mathbf{R}\,(\varphi = 0^{\circ}, \theta = 90^{\circ}, \psi = 0^{\circ}) = \begin{bmatrix} 1 & 0 & 0 \\ 0 & 0 & 1 \\ 0 & -1 & 0 \end{bmatrix}, \tag{6.6}$$

all tensors in (6.2) must be transformed. Note, that the transformation of $[\mathbf{g}\boldsymbol{m}]^{\times}$ must be evaluated properly. One possible way is to transform $\boldsymbol{\alpha}$ and $\mathbf{m}^{\times}$ first, and use (4.25) then. The other way is to use (4.2), so the transformation takes the form

$$\mathbf{R}\,(0^{\circ}, 90^{\circ}, 0^{\circ})\left[\mathrm{tr}\,(\boldsymbol{\alpha})\,\mathbf{I} - \boldsymbol{\alpha}^{\mathrm{T}}\right]\mathbf{R}^{\mathrm{T}}\,(0^{\circ}, 90^{\circ}, 0^{\circ}). \tag{6.7}$$

Either way is leading to the solution of determinant (6.2) and to biquadratic equation

$$\left(\varepsilon_{11} - n^2 - \alpha_{11}^2\right)\left(\varepsilon_{11} - \alpha_{11}^2\right)\left(\varepsilon_{33} - n^2 - \alpha_{33}^2\right) - 4n^2\alpha_{11}^2\left(\varepsilon_{11} - \alpha_{11}^2\right) = 0. \tag{6.8}$$

The analytical solution of the biquadratic equation evaluated up to the second-order in α takes the form

$$n_{k,\perp}^2 = \frac{1}{2}\left[\left(\varepsilon_{11} + \varepsilon_{33}\right) + \left(\alpha_{11}^2 - \alpha_{33}^2\right) \pm \sqrt{\left(\varepsilon_{11} - \varepsilon_{33}\right)^2 + \alpha_{11}^2\left(6\varepsilon_{11} + 10\varepsilon_{33}\right) + 2\alpha_{33}^2\left(\varepsilon_{11} - \varepsilon_{33}\right)}\right]. \tag{6.9}$$

If we turn off the optical activity (by setting $\alpha_{11} = \alpha_{33} = 0$), we get a standard set of eigenmodes for common anisotropic non-gyrotropic uniaxial crystal:

$$n_{1,3}\left(\boldsymbol{\alpha} = 0\right) = \sqrt{\varepsilon_{11}} = n_{\text{ordinary}}, \tag{6.10}$$

$$n_{2,4}\left(\boldsymbol{\alpha} = 0\right) = \sqrt{\varepsilon_{33}} = n_{\text{extraordinary}}. \tag{6.11}$$

6.2 Mueller matrix of gyrotropic uniaxial retarder

The most common uniaxial gyrotropic material is the quartz. The quartz crystals belong to the trigonal symmetry of point group 32. It is very common, that precisely grown quartz monocrystals are used for the retardation optical elements – waveplates. Waveplates are generally made from a slab of uniaxial optical materials of a certain thickness. Despite the fact, that the quartz is optically active material, it has usually no impact on the performance of the waveplate, because the optical axis of the quartz waveplate is oriented perpendicular to the direction of the wave propagation, and the effect of optical activity is very small. However, if this material is gyrotropic, this effect should be detectable and measurable anyway.

In the following text, we will reffer on our research, Equations, and Figures, which are shown in the attached article in Appendix C. The article was published by us [131]. In this work [131], see Appendix C, we studied quartz waveplates using spectral Mueller matrix ellipsometry in the transmission configuration in the wide spectral range from 193 to 1700 nm. The waveplates were analyzed in the configuration shown in Fig. 6.1b. In this study we have shown, that the effect of non-zero circular birefringence (CB) is present (Fig. C.5, Eqs. [C.6], [C.7]) (using the Lu-Chipman decomposition, Eq. [C.5]), which can be possible if and only if the material is gyrotropic. Moreover, we have proved, that the non-zero CB could not arise from various other effects as, for example, waveplate misalignement. The model of the studied waveplates was based on the Mueller matrix for a linear retarder (Eq. [B.3], [C.1]). To properly fit measured data, we modeled influence of the finite monochromator bandwidth, which in our case corresponds to the spectral resolution of dispersion grating and finite pixel size of the CCD detector. The model is based on an incoherent summation of the Mueller matrices with Gaussian spectral profile, see Eqs. (C.3), (C.4). The fit on the experimental data is shown in Fig. C.1, and the fit stability is demonstrated in Fig. C.3.

However, in this study, the phenomenon of the optical activity wasn't described using a rigorous model of the Mueller matrix. In the following text, we propose the derivation of the rigorous Mueller matrix model of uniaxial chiral media.

To derive the Mueller matrix of gyrotropic uniaxial retarder, related Jones matrix have to be calculated in the first place. The transmission Jones matrix, which describes an arbitrary non-depolarizing transmission optical system (A.15) is given as

$$\mathbf{T} = \frac{1}{\chi_{e1} - \chi_{e2}} \begin{bmatrix} \chi_{e1} V_{e2} - \chi_{e2} V_{e1} & V_{e1} - V_{e2} \\ -\chi_{e1}\chi_{e2} \left(V_{e1} - V_{e2}\right) & \chi_{e1} V_{e1} - \chi_{e2} V_{e2} \end{bmatrix}, \tag{6.12}$$

where $\chi_{e1,e2}$ are the eigenpolarizations of the optical system, and $V_{e1,e2}$ are the eigenvalues associated with the eigenpolarizations, and are related by Eq. (A.13)

$$\mathbf{T}\boldsymbol{J}_e = V_e \boldsymbol{J}_e, \tag{6.13}$$

where $\mathbf{T}$ is the transmission Jones matrix, and $\boldsymbol{J}_e$ is the eigenpolarization Jones vector. This equation shows, that if a pair of eigenpolarization is transmitted through an optical system described by $\mathbf{T}$, the eigenpolarizations remains the same except for the eigenvalue multiple. The detailed derivation is showed in Appendix A. The transmission Jones matrix of elliptical retarder is obtained by setting [2] $\chi_{e1} = \chi_{ef}$, $\chi_{e2} = \chi_{es}$, $V_{e1} = \mathrm{e}^{\mathrm{i}\Delta/2}$, and $V_{e2} = \mathrm{e}^{\mathrm{i}\Delta/2}$. The eigenpolarization χ_{e1} is phase-advanced by $\Delta/2$, therefore χ_{ef} represents the fast eigenpolarization, while the eigenpolarization χ_{e2} is phase-retarded by $\Delta/2$, and χ_{es} represents the slow eigenpolarization. The phase angle Δ represents the retardance of the elliptic retarder, and is given by the relation

$$\Delta = \frac{2\pi}{\lambda} \left(n_{\mathrm{EL}+} - n_{\mathrm{EL}-}\right) d, \tag{6.14}$$

where $n_{\mathrm{EL}+,\mathrm{EL}-}$ are the refractive indices of two mutually orthogonal elliptic eigenpolarizations, and d is the thickness of the material. The eigenpolarizations $\chi_{ef,es}$ are orthogonal, and are therefore related by the orthogonality condition

$$\chi_{ef}\chi_{es}^* = \chi_{ef}^*\chi_{es} = -1. \tag{6.15}$$

Therefore, the Jones matrix for an elliptic retarder can be obtained from (6.12) as

$$\mathbf{T} = \frac{1}{1+\chi\chi^*} \begin{bmatrix} \mathrm{e}^{\mathrm{i}\frac{\Delta}{2}} + \chi\chi^*\mathrm{e}^{-\mathrm{i}\frac{\Delta}{2}} & 2\mathrm{i}\chi^* \left(\mathrm{e}^{\mathrm{i}\frac{\Delta}{2}} - \mathrm{e}^{-\mathrm{i}\frac{\Delta}{2}}\right) \\ 2\mathrm{i}\chi^* \left(\mathrm{e}^{-\mathrm{i}\frac{\Delta}{2}} - \mathrm{e}^{\mathrm{i}\frac{\Delta}{2}}\right) & \chi\chi^*\mathrm{e}^{\mathrm{i}\frac{\Delta}{2}} + \mathrm{e}^{-\mathrm{i}\frac{\Delta}{2}} \end{bmatrix} = \frac{1}{1+\chi\chi^*} \begin{bmatrix} \mathrm{e}^{\mathrm{i}\frac{\Delta}{2}} + \chi\chi^*\mathrm{e}^{-\mathrm{i}\frac{\Delta}{2}} & 2\mathrm{i}\chi^* \sin\frac{\Delta}{2} \\ 2\mathrm{i}\chi \sin\frac{\Delta}{2} & \chi\chi^*\mathrm{e}^{\mathrm{i}\frac{\Delta}{2}} + \mathrm{e}^{-\mathrm{i}\frac{\Delta}{2}} \end{bmatrix}. \tag{6.16}$$

Every Jones vector can be represented by the complex polarization parameter χ as follows (see (A.2)):

$$\boldsymbol{J} = \begin{bmatrix} 1 \\ \chi \end{bmatrix}, \tag{6.17}$$

The complex polarization parameter completely defines the polarization ellipse of the polarized light. The Jones vector of elliptically polarized wave is

$$\boldsymbol{J} = \begin{bmatrix} \cos\epsilon \\ \mathrm{i}\sin\epsilon \end{bmatrix} = \begin{bmatrix} 1 \\ \mathrm{i}\tan\epsilon \end{bmatrix} \equiv \begin{bmatrix} 1 \\ \mathrm{i}\kappa \end{bmatrix}, \tag{6.18}$$

where $\tan\epsilon = \kappa$ and it determines the ellipticity (see Fig. 6.2), therefore it determines the polarization state of the wave.

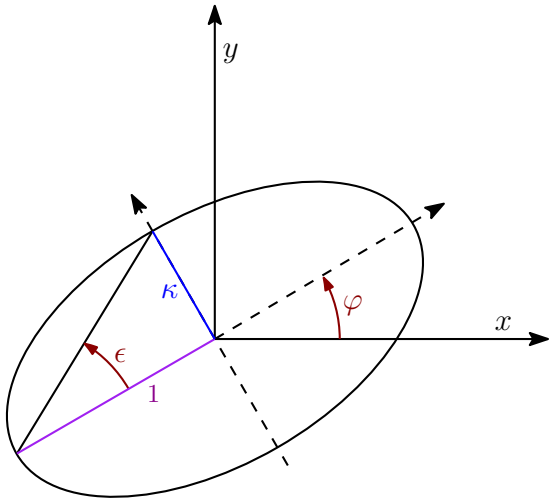

Figure 6.2: The polarization ellipse. Without loss of generality, we can set the length of the main half-axis to be unit. The ellipticity of the polarization ellipse can be defined using $\tan\epsilon = \frac{\kappa}{1}$.

The Jones matrix of elliptical retarder can be derived by setting $\chi = \mathrm{i}\kappa$:

$$\mathbf{T} = \frac{1}{1+\kappa^2}\begin{bmatrix} \mathrm{e}^{\mathrm{i}\frac{\Delta}{2}} + \kappa^2\mathrm{e}^{-\mathrm{i}\frac{\Delta}{2}} & 2\kappa\sin\frac{\Delta}{2} \\ -2\kappa\sin\frac{\Delta}{2} & \kappa^2\mathrm{e}^{\mathrm{i}\frac{\Delta}{2}} + \mathrm{e}^{-\mathrm{i}\frac{\Delta}{2}} \end{bmatrix}. \tag{6.19}$$

Now, the Mueller matrix of elliptical retarder can be derived using (2.16). We will show the Mueller matrix linearly approximated in κ:

$$\boldsymbol{M}_{\mathrm{R,EL}}(\Delta,\,\kappa) = \begin{bmatrix} 1 & 0 & 0 & 0 \\ 0 & 1 & 2\kappa\sin\Delta & 4\kappa\sin^2\frac{\Delta}{2} \\ 0 & -2\kappa\sin\Delta & \cos\Delta & \sin\Delta \\ 0 & 4\kappa\sin^2\frac{\Delta}{2} & -\sin\Delta & \cos\Delta \end{bmatrix} \tag{6.20}$$

Using the Mueller rotation matrix $\mathbf{R}$ from (B), the Mueller matrix of elliptical retarder at different azimuthal rotation φ is given by

$$\mathbf{M}_{\mathrm{R,EL}}(\varphi,\,\Delta,\,\kappa) = \mathbf{R}^{\mathrm{T}}(\varphi)\,\mathbf{M}_{\mathrm{R,EL}}(\Delta,\,\kappa)\,\mathbf{R}(\varphi). \tag{6.21}$$

The general expression of the matrix $\mathbf{M}_{\mathrm{R,EL}}(\varphi,\,\Delta,\,\kappa)$ can be separated into two parts as

$$\mathbf{M}_{\mathrm{R,EL}}(\varphi,\,\Delta,\,\kappa) = \mathbf{M}_{\mathrm{R,LIN}}(\varphi,\,\Delta) + \mathbf{N}_{\mathrm{OA}}(\varphi,\,\kappa), \tag{6.22}$$

where

$$\mathbf{M}_{\mathrm{R,LIN}}(\varphi,\,\Delta) = \begin{bmatrix} 1 & 0 & 0 & 0 \\ 0 & \cos^2 2\varphi + \cos\Delta \sin^2 2\varphi & (1-\cos\Delta)\sin 2\varphi \cos 2\varphi & -\sin 2\varphi \sin\Delta \\ 0 & (1-\cos\Delta)\sin 2\varphi \cos 2\varphi & \sin^2 2\varphi + \cos\Delta \cos^2 2\varphi & \cos 2\varphi \sin\Delta \\ 0 & \sin 2\varphi \sin\Delta & \cos 2\varphi \sin\Delta & \cos\Delta \end{bmatrix}, \tag{6.23}$$

is the Mueller matrix for a non-gyrotropic linear retarder, and

$$\mathbf{N}_{\mathrm{OA}}(\varphi,\,\kappa) = \begin{bmatrix} 0 & 0 & 0 & 0 \\ 0 & 0 & -2\kappa \sin\Delta & 4\kappa \cos 2\varphi \sin^2 \frac{\Delta}{2} \\ 0 & 2\kappa \sin\Delta & 0 & 4\kappa \sin 2\varphi \sin^2 \frac{\Delta}{2} \\ 0 & 4\kappa \cos 2\varphi \sin^2 \frac{\Delta}{2} & 4\kappa \sin 2\varphi \sin^2 \frac{\Delta}{2} & 0 \end{bmatrix}, \tag{6.24}$$

is the perturbation matrix describing the linear effect of the optical activity separately. Note, that the matrix $\mathbf{N}_{\mathrm{OA}}(\varphi,\,\kappa)$ is *not* the *Mueller* matrix, because it does not satisfy the physical conditions, which every Mueller matrix must fulfil. However, the separability of the gyrotropic and non-gyrotropic properties of the proposed Mueller matrix $\mathbf{M}_{\mathrm{R,EL}}(\varphi,\,\Delta,\,\kappa)$ will be advantageous in the understanding and in the physical interpretation of measured samples. Moreover, if we turn the optical activity off ($\kappa = 0$), we will obtain equality $\mathbf{M}_{\mathrm{R,EL}}(\varphi,\,\Delta,\,\kappa = 0) = \mathbf{M}_{\mathrm{R,LIN}}(\varphi,\,\Delta)$, and the resulting Mueller matrix will stand for a description of linear retarder, which is a correct limit exampple.

The only quantity, which must be evaluated now is the parameter κ describing the chirality. The quantity κ describes the polarization properties of the light. Therefore, it is convenient to use the displacement vector $\boldsymbol{D}$ instead of $\boldsymbol{E}$, because $\boldsymbol{D}$ is always perpendicular to the propagation direction. Also, it is convenient to use Born-Landau material constitutive relations (4.1) and to define the inverse permittivity tensor $\boldsymbol{\varepsilon}^{-1}$. The Eq. (4.1a) is then rewriten as

$$\boldsymbol{E} = \boldsymbol{\varepsilon}^{-1}\boldsymbol{D} + \mathrm{i}\boldsymbol{D} \times \boldsymbol{G}. \tag{6.25}$$

It can be shown [101, 111], that we can solve the eigenvalue problem (4.28) with respect to the particular form of the constitutive relation in the coordinate system $(D_1,\ D_2,\ z)$, so that $z \perp D_1 \wedge z \perp D_2$. If we solve the eigenvalue problem (4.28), the ellipticity of the eigenpolarizations can be calculated as the ratio between the polarizations $\boldsymbol{D_1}$ and $\boldsymbol{D_2}$. The ellipticity parameter κ is then defined as

$$\kappa = \frac{1}{2G}\left[\left(n_2^2 - n_1^2\right) - \sqrt{\left(n_2^2 - n_1^2\right)^2 + 4G^2}\right], \tag{6.26}$$

where $n_{1,2}$ are the eigenmodes of the uniaxial medium and G is the scalar gyration parameter. From (4.39) and using Tab. 4.2, the gyration scalar parameter for quartz crystal (of point group 32) is given as

$$G = g_{11} \sin^2 \theta + g_{33} \cos^2 \theta. \tag{6.27}$$

The gyration tensor components g_{11} and g_{33} can be modeled using the dispersion model (5.13), and the angle θ is known from the configuration of the experiment (see Fig. 6.1).

We hope, that the proposed method of modelling the Mueller matrix for chiral uniaxial media, will be a suitable tool for the rigorous description of the experimental data of a quartz waveplate, which will be a logic continuation of our work published in [131] and which is attached in Appendix C.

7 Conclusion and perspective

The original contribution of the author of the thesis:

- We have proposed a novel technique, how to measure the effect of the optical activity in the chiral liquids (glucose, fructose, sucrose solutions) using the spectroscopic Mueller matrix ellipsometry. The huge advantage of our method is the broad spectral range over which the values of specific rotatory power are calculated (Fig. 5.3).
- We are able to determine the angles of arbitrary polarization plane rotation absolutely, which is in a contrast with the single wavelength measurements [127]. The theoretical limits of the concentration detection and the measurement precision were determined (Tab. 5.4).
- The mutarotation rate constants for the mutarotation reaction of Glucose anomers were obtained (Fig. 5.4) with high precision (Tab. 5.3). The results, together with the mutarotation kinetics of fructose, lactose, and tartaric acid, are planned to be published.
- We developed an unique temperature control system (Figs. 5.6, 5.7) with high stability for the specific rotatory power measurements (Fig. 5.9).
- Optical activity of uniaxial quartz used for compensator plates was determined. We calculated a theoretical model of Mueller matrix (Eqs. [6.22]–[6.24]) for a quartz waveplate elliptic retarder assuming the effect of the optical activity.
- We discussed various effects arising in Mueller algebra and we connected them with the experiments. Those include mainly:
  - Experimental demonstration of the components of purity for Mueller matrix of wire-grid polarizer and composed quartz waveplate, Fig. 2.4, see Appendix C.
  - We discussed effects of the sum decomposition on the ideal thin film system designed for the SPR measurements, Fig. 2.2

Perspectives for future work:

- To gain a deep understanding of the theoretical Mueller algebra and connect the theoretical quantities with a proper experiment to demonstrate their meaning.
- To measure and model the temperature-dependent mutarotation kinetics of various chiral molecules (monosaccharides, lactose, tartaric acid) in order to obtain the hysteresis loop of the specific rotatory power.
- To validate the theoretical description of the elliptic retarder Mueller matrix including the chirality using the experimental data of quartz waveplate. In the next step, the model

will be fitted to the experimental data and the influence of the optical activity will be calculated.

- To extend the spectral range out of the scope of the RC2-DI Woollam Mueller matrix ellipsometer (193 nm to 1700 nm) to infrared and terahertz spectral range, and to model the chirality of the media within this range.

List of the publications:

- Koleják, P., D. Vala, K. Postava, P. Provazníková, and J. Pištora. *Mueller matrix ellipsometry of waveplates for control of their properties and alignment.* J. Vac. Sci. Technol. B. vol. 38(1), 2020

- Gryga, M., D. Vala, P. Koleják, L. Gembalová, D. Ciprian, and P. Hlubina. *One-dimensional photonic crystal for Bloch surface waves and radiation modes-based sensing.* Opt. Mat. Express. vol. 9, 2019,

- Vala, D., M. Mičica, K. Postava, and J. Pištora. *Optical activity temperature-dependent measurements of chiral solutions using Mueller matrix spectroscopic ellipsometry*, Proc. SPIE 10976, 21st Czech-Polish-Slovak Optical Conference on Wave and Quantum Aspects of Contemporary Optics, 2018, 109760A,

A Generalized Jones calculus

A.1 Polarization and Complex-Amplitude Transfer Functions

Equation (2.11) in arbitrary u, v coordinate system defined by unit vectors $\hat{\boldsymbol{u}}$, $\hat{\boldsymbol{v}}$ can be expressed as

$$\begin{bmatrix} E_u^o \\ E_v^o \end{bmatrix} = \begin{bmatrix} T_{11} & T_{12} \\ T_{21} & T_{22} \end{bmatrix} \begin{bmatrix} E_u^i \\ E_v^i \end{bmatrix}, \tag{A.1}$$

and represents the system of two linear equations. Introducing *complex polarization parameter* $\chi = f(\theta, \epsilon)$

$$\chi = \frac{E_v}{E_u}, \tag{A.2}$$

the system can be recasted into

$$\frac{E_v^o}{E_u^o} = \frac{T_{21} + T_{22}\,(E_v^i/E_u^i)}{T_{11} + T_{12}\,(E_v^i/E_u^i)}, \tag{A.3}$$

and using (A.2), into

$$\chi^o = \frac{T_{21} + T_{22}\chi^i}{T_{11} + T_{12}\chi^i} \equiv \mathrm{PTF}(\chi^i). \tag{A.4}$$

The Equation (A.4) is called *Polarization Transfer Function* and shows, that the polarization state of the wave is transformed independently of the wave amplitude and absolute phase. Substituting (A.2) into (2.9) and using (2.10), we get normalized Jones vectors

$$\boldsymbol{J}^{i,\,o} = \frac{1}{\sqrt{1 + \chi^{i,\,o}\,(\chi^{i,\,o})^*}} \begin{bmatrix} 1 \\ \chi^{i,\,o} \end{bmatrix}, \tag{A.5}$$

which can be further expressed as

$$\boldsymbol{J}^{i,\,o} = \frac{A_{\mathrm{c}}^{i,\,o}}{\sqrt{1 + \chi^{i,\,o}\,(\chi^{i,\,o})^*}} \begin{bmatrix} 1 \\ \chi^{i,\,o} \end{bmatrix}, \tag{A.6}$$

where $A_{\mathrm{c}}^{i,\,o}$ is a complex number with its amplitude and phase. $A_{\mathrm{c}}^{i,\,o}$ is in the particular form of

$$A_{\mathrm{c}}^{i,\,o} = E_u^{i,\,o}\sqrt{1 + \chi^{i,\,o}\,(\chi^{i,\,o})^*}, \tag{A.7}$$

in which it fulfills $\boldsymbol{J}^\dagger \boldsymbol{J} = A_c^* A_c$. Therefore, Jones vector introduced by Eq. (A.6) represents a form, in which the information of the polarization state is separated from the information about the wave amplitude and phase. Substituting (A.6) into (A.1), we obtain the *Complex-Amplitude*

Transfer Function representing the change in A_c upon transformation of $\mathbf{J}$,

$$A_\mathrm{c}^o = \left[\sqrt{\frac{1+\chi^o\left(\chi^o\right)^*}{1+\chi^i\left(\chi^i\right)^*}}\left(T_{11}+\chi^i T_{12}\right)\right] A_\mathrm{c}^i \equiv \mathrm{CATF}\left(\chi^i,\chi^o\right) A_\mathrm{c}^i. \tag{A.8}$$

A.2 Eigenpolarizations of transmission media, Jones matrix

Eigenpolarizations are particular polarization states of the wave, which are not changed during the propagation in medium characterized by defined Jones matrix. Therefore, $\chi^o = \chi^i$. Two cases may occur. First, from known transmission Jones matrix $\mathbf{T}$, the eigenstates can be calculated. Second, from known eigenstates, matrix $\mathbf{T}$ can be reconstructed.

- We obtain eigenpolarizations of matrix $\mathbf{T}$ by setting $\chi^o = \chi^i = \chi$. PTF (A.4) is then

$$\chi = \frac{T_{21}+T_{22}\chi}{T_{11}+T_{12}\chi}, \tag{A.9}$$

  which provides a quadratic equation in χ with the roots

$$\chi_{e1,\,e2} = \frac{1}{2T_{12}}\left[\left(T_{22}-T_{11}\right) \pm \sqrt{\left(T_{22}-T_{11}\right)^2 + 4T_{12}T_{21}}\right]. \tag{A.10}$$

  Similarly, by setting $\chi^o = \chi^i = \chi$ in CATF, we obtain a set of linear equations

$$\mathrm{CATF}\left(\chi_{e1,2}\right) = T_{11} + \chi_{e1,2}T_{12}, \tag{A.11}$$

  and substituting (A.10) into (A.11), we get the eigenvalues $V_{e1,2}$ associated with the eigenpolarizations $\chi_{e1,2}$

$$V_{e1,\,e2} = \frac{1}{2}\left[\left(T_{11}+T_{22}\right) \pm \sqrt{\left(T_{22}-T_{11}\right)^2 + 4T_{12}T_{21}}\right]. \tag{A.12}$$

  Therefore, the eigenstates of the system desribed with transmission Jones matrix $\mathbf{T}$ are fully characterized. Note, that the eigenpolarizations with associated eigenvalues are linked together via

$$\mathbf{T}\boldsymbol{J}_e = V_e\boldsymbol{J}_e. \tag{A.13}$$

- The solution of the inverse problem is rather straightforward. Using equations (A.11) and

(A.12), we obtain a system of four linear equations with variables T_{ij}:

$$V_{e1} = T_{12}\chi_{e1} + T_{11}, \tag{A.14a}$$

$$V_{e2} = T_{12}\chi_{e2} + T_{11}, \tag{A.14b}$$

$$V_{e1} = \frac{1}{2}\left[(T_{11} + T_{22}) + \sqrt{(T_{22} - T_{11})^2 + 4T_{12}T_{21}}\right], \tag{A.14c}$$

$$V_{e2} = \frac{1}{2}\left[(T_{11} + T_{22}) - \sqrt{(T_{22} - T_{11})^2 + 4T_{12}T_{21}}\right]. \tag{A.14d}$$

Sum of the later two equations gives $V_{e1} + V_{e2} = T_{11} + T_{22}$, what makes the solution of the rest trivial. Solved values of T_{ij} define the transmission Jones matrix $\mathbf{T}$, which describes *any* non-depolarizing transmission system with preset eigenstates, so the Eq. (A.13) is not violated:

$$\mathbf{T} = \frac{1}{\chi_{e1} - \chi_{e2}} \begin{bmatrix} \chi_{e1}V_{e2} - \chi_{e2}V_{e1} & V_{e1} - V_{e2} \\ -\chi_{e1}\chi_{e2}\left(V_{e1} - V_{e2}\right) & \chi_{e1}V_{e1} - \chi_{e2}V_{e2} \end{bmatrix}. \tag{A.15}$$

B Mueller matrices of basic polarizing components

- General anisotropic depolarizer: The anisotropic coefficients a, b, c affect the depolarization power of the system along S_1, S_2, S_3 components of the Stokes vector $\mathbf{S}$ (Eq. (2.13)). For $a = b = c = 0$, the matrix stands for an ideal depolarizer, which is independent of the input intensity, and any input polarization state of the light is totally depolarized [27].

$$\mathbf{M}_\Delta = \begin{bmatrix} 1 & 0 & 0 & 0 \\ 0 & a & 0 & 0 \\ 0 & 0 & b & 0 \\ 0 & 0 & 0 & c \end{bmatrix} \tag{B.1}$$

- Linear polarizer: The orientation of the polarizer axis is given by the angle φ.

$$\mathbf{M}_\mathrm{P}(\varphi) = \begin{bmatrix} 1 & \cos 2\varphi & \sin 2\varphi & 0 \\ \cos 2\varphi & \cos^2 2\varphi & \sin 2\varphi \cos 2\varphi & 0 \\ \sin 2\varphi & \sin 2\varphi \cos 2\varphi & \sin^2 2\varphi & 0 \\ 0 & 0 & 0 & 0 \end{bmatrix} \tag{B.2}$$

- Linear Retarder: The retarder fast axis orientation is given by the angle φ and the total retardation of the system is given by the retardation angle Δ.

$$\mathbf{M}_{\mathrm{R,LIN}}(\varphi,\, \Delta) = \begin{bmatrix} 1 & 0 & 0 & 0 \\ 0 & \cos^2 2\varphi + \cos\Delta \sin^2 2\varphi & (1-\cos\Delta)\sin 2\varphi \cos 2\varphi & -\sin 2\varphi \sin\Delta \\ 0 & (1-\cos\Delta)\sin 2\varphi \cos 2\varphi & \sin^2 2\varphi + \cos\Delta \cos^2 2\varphi & \cos 2\varphi \sin\Delta \\ 0 & \sin 2\varphi \sin\Delta & \cos 2\varphi \sin\Delta & \cos\Delta \end{bmatrix} \tag{B.3}$$

- Rotation matrix: The coordination system is rotated about the angle φ using the matrix

$$\mathbf{R}(\varphi) = \begin{bmatrix} 1 & 0 & 0 & 0 \\ 0 & \cos 2\varphi & \sin 2\varphi & 0 \\ 0 & -\sin 2\varphi & \cos 2\varphi & 0 \\ 0 & 0 & 0 & 1 \end{bmatrix}. \tag{B.4}$$

  The transformation of the arbitrary Mueller matrix $\mathbf{M}$ is given by

$$\mathbf{M}(\varphi) = \mathbf{R}^\mathrm{T}(\varphi)\, \mathbf{M}\, \mathbf{R}(\varphi). \tag{B.5}$$

C Full text Article: Mueller matrix ellipsometry of waveplates for control of their properties and alignment

The full text of the article starts on the following page. The connection with this thesis is given in Section 6.2.

Contribution of the author of this thesis to the article:

The full text of the paper is given in following pages. The article was written by Pierre Koleják and author of this thesis (Daniel Vala). I have written part of the Introduction and Chapter IV. I performed all experimental Mueller matrix ellipsometry measurements of studied samples. I also performed Lu-Chipman decomposition on the experimental data (Eq. [C.5]), and from the decomposed matrices, I obtained the effect of the circular birefrience (see Fig. C.5 and Eqs. [C.6], [C.7]). Further, I discussed the effects of the optical activity in the studied waveplates.

JVST B
Journal of Vacuum Science & Technology B

ARTICLE

avs.scitation.org/journal/jvb

Mueller matrix ellipsometry of waveplates for control of their properties and alignment

Cite as: J. Vac. Sci. Technol. B 38, 014006 (2020); doi: 10.1116/1.5129615
Submitted: 30 September 2019 · Accepted: 25 November 2019 ·
Published Online: 18 December 2019

Pierre Koleják,[1,a)] Daniel Vala,[1] Kamil Postava,[1,b)] Pavlína Provazníková,[2] and Jaromír Pištora[1]

AFFILIATIONS

[1]Nanotechnology Centre and IT4Innovations, VŠB-Technical University of Ostrava, 17. listopadu 15, 70800 Ostrava-Poruba, Czech Republic
[2]Meopta-Optika s.r.o., Kabelíkova 1, 750 02 Přerov, Czech Republic

Note: This paper is part of the Conference Collection: 8th International Conference on Spectroscopic Ellipsometry 2019, ICSE.
[a)]**Electronic mail:** pierre.kolejak@vsb.cz
[b)]**Electronic mail:** kamil.postava@vsb.cz

ABSTRACT

In this paper, the authors characterize high-order quartz waveplates in the wide spectral range (from 193 to 1700 nm) using a commercial Mueller matrix ellipsometer RC2-DI-Woollam. They demonstrate that Mueller matrix ellipsometry is a powerful tool to obtain the waveplate retardation in a wide spectral range together with azimuthal angles of optical axes with good accuracy. Moreover, they deal with depolarization caused by a finite monochromator bandwidth, which is included in the model using incoherent averaging of Mueller matrices. The application of Lu–Chipman Mueller matrix decomposition to extract depolarization from data is also demonstrated. Finally, Lu–Chipman decomposition is used to demonstrate the presence of the optical activity in quartz, which one may misinterpret with incorrect alignment of the waveplate azimuth angle.

I. INTRODUCTION

Waveplates are important optical polarization components used in polarimetry.[1–4] Waveplates are usually made from a slab of uniaxial optical materials of a certain thickness. The waveplate retardation is obtained as the difference between phases of modes polarized along two perpendicular directions. Waveplates of higher order that are designed for manufacturing exhibit high chromatic dispersion. Therefore, broadly used zero-order waveplates are composed by the higher order plates with crossed optical axes. High accuracy fabrication is crucial for waveplate applications in the semiconductor industry, particularly for operation with ultraviolet light. It requires advanced measurement and control of their parameters and fine adjustment.

Typical industrial inspection of waveplates uses a single-wavelength method based on two crossed polarizers, with the waveplate being placed between them. The method gives orientation of the waveplate axis and its single-wavelength retardation. Nevertheless, methods based on two crossed polarizers for only one wavelength seem to be insufficient for recent quality control requirements.

It is well known that, for the waveplate analysis, the Jones calculus[5,6] represents a convenient description to acquire an exact quantitative and a qualitative analysis of a waveplate, for example, by the meaning of the null ellipsometry measurements. However, the analysis based on the Jones calculus cannot offer proper treatment of various effects such as depolarizations. The Mueller calculus appears to be particularly favorable in the waveplate analysis,[7] since one obtains complete ellipsometric and polarimetric information about the sample, especially in a wide spectral range. It is a powerful tool for the characterization of anisotropic samples in a wide spectral range including the ultraviolet region,[8] which, furthermore, could include depolarization phenomena.[9,10]

In this paper, we apply the Mueller matrix transmission spectroscopic ellipsometry to investigate high-order quartz waveplates. We demonstrate that a correct data processing requires proper incorporation of depolarization effects. The correction can be directly added to the model rigorously, or the depolarization phenomena may be separated from the experimental Mueller matrix. For this purpose, Lu–Chipman polar decomposition seems to be a

suitable tool. We further demonstrate the numerical stability of obtained parameters.

The article is structured as follows: In Sec. II, the experimental setup and notation are introduced and the analytical form of the Mueller matrix is shown. Section III describes the experiments on single waveplates. The model description is divided into two parts: First, the rigorous solution including depolarization effects is given, and, second, a Lu–Chipman depolarization separated alternative is offered.

II. MUELLER MATRIX ELLIPSOMETRY

Mueller matrices describe complete polarization properties of the investigated sample also including depolarization in contrast with the coherent Jones description. We applied spectral ellipsometric measurements by the dual rotating compensator Mueller matrix ellipsometer RC2-DI from Woollam company, which measures a full Mueller matrix in the spectral range from 0.74 to 6.42 eV (wavelength ranging from 193 to 1700 nm). The waveplates are measured in the normal-incidence transmission geometry.

A. Single waveplate model

The reduced Mueller matrix of a single waveplate consisting of a uniaxial anisotropic material with the optical axis parallel to the waveplate surface at the normal incidence is used in this paper in the form[3,4]

$$\mathbf{M}(\delta,\alpha)=\begin{pmatrix}1 & 0 & 0 & 0\\ 0 & \cos^2 2\alpha+\cos\delta\sin^2 2\alpha & \cos 2\alpha\sin 2\alpha-\cos 2\alpha\sin 2\alpha\cos\delta & -\sin 2\alpha\sin\delta\\ 0 & \cos 2\alpha\sin 2\alpha-\cos 2\alpha\sin 2\alpha\cos\delta & \cos\delta\cos^2 2\alpha+\sin^2 2\alpha & \cos 2\alpha\sin\delta\\ 0 & \sin 2\alpha\sin\delta & -\cos 2\alpha\sin\delta & \cos\delta\end{pmatrix}, \tag{1}$$

where α is the azimuthal angle describing the optical axis direction with respect to the x-axis of the ellipsometer and δ is the waveplate retardation, which could be expressed as a function of wavelength,

$$\delta(\lambda)=\frac{2\pi}{\lambda}d\,[n_e(\lambda)-n_o(\lambda)], \tag{2}$$

where λ, d, n_e, and n_o are the wavelength, the waveplate thickness, the extraordinary refractive index, and the ordinary refractive index, respectively. Note that the reduced Mueller matrix is obtained by dividing all matrix elements by M_{11}. According to the structure of the matrix (1), we will be focused fully on the 3×3 submatrix $M_{22}\cdots M_{44}$. Note that element M_{44} includes only dependence on retardation (2), it can be directly recalculated to the retardation $\delta(\lambda)=\arccos(M_{44})$. In this paper, we investigate quartz waveplates, where refractive index spectra are taken from Refs. 11 and 12 described by Sellmeier terms.

III. SINGLE WAVEPLATE MEASUREMENTS

We have investigated c-cut right-handed synthetic α-quartz high-order waveplates measured in the normal incident transmission configuration for all azimuthal angles from 0° to 360° by an angle step of 5°. Figure 1 shows typical spectra (black curves) of the Mueller 3×3 submatrix (excluding the first row and the first column) for the waveplate of thickness around 0.5 mm. Rapid oscillations correspond to the wavelength dependence of retardation (2). The decreasing oscillation amplitude with increasing photon energy originates from the rising density of oscillations and its averaging due to the finite monochromator bandwidth. The decrease does not come from the absorption of the quartz waveplate, which was proved by transmission measurement, and does not show attenuation due to absorption. To properly fit measured data, we model influence of the finite monochromator bandwidth,[13,14] which in our case corresponds to the spectral resolution of dispersion grating and finite pixel size of the CCD detector. The equivalent monochromator bandwidth is critical, especially for high-order waveplates. The model is based on an incoherent summation of the Mueller matrices (1) with the Gaussian spectral profile[15] described by the averaging function G_n,

$$\bar{M}_{ij}(\lambda)=\frac{\sum_{n=-N}^{N}M_{ij}(\lambda+n\,\delta\lambda)G_n}{\sum_{n=-N}^{N}G_n}, \tag{3}$$

where

$$G_n=\exp\left[-\ln 2\left(\frac{n\,\delta\lambda}{\Delta\lambda}\right)^2\right], \tag{4}$$

where N, $\Delta\lambda$, and $\delta\lambda$ are the integer of points on the right and left side from the central wavelength included in the averaging, the monochromator bandwidth, and the spectral step in the averaging (we use $\delta\lambda=1$ nm), respectively.

The model including spectral averaging (3) is compared to the experimental data in Fig. 1. Waveplate properties obtained from the fit are the spectral retardation, the waveplate thickness, and the axis azimuth. Moreover, high-order waveplates are the ideal sample to fit and determine the monochromator bandwidth of the ellipsometer setup. The broad spectral range allows us to determine the waveplate order, and waveplate retardation in the whole spectral range is shown in Fig. 2. Note that the absolute retardation is obtained (including the waveplate order), in contrast to single-wavelength measurement. The fitted parameters of whole 360° rotation are $d=518.55\,\mu$m, $\alpha_0=224.766°$, and $\Delta\lambda=1.0534$ nm, where α_0 is the azimuthal angle of the initial position.

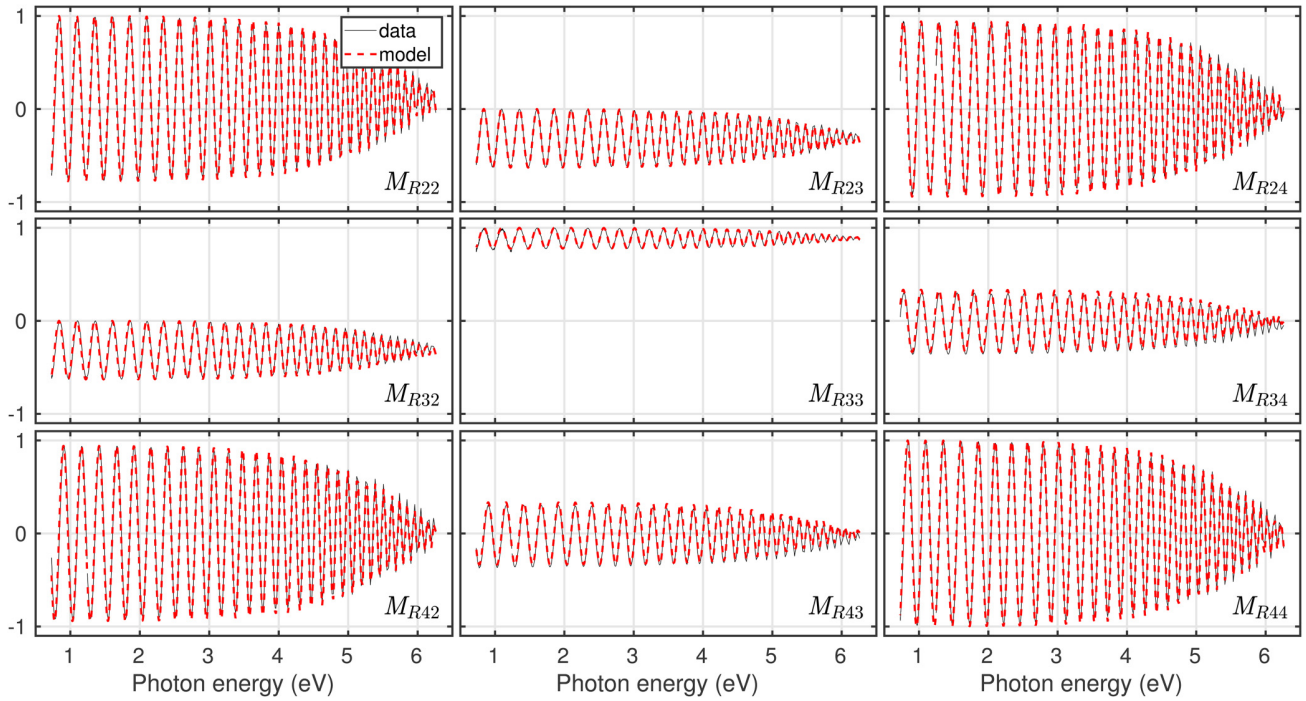

FIG. 1. Model and data Mueller submatrix of single high-order waveplates with an azimuthal angle of $\alpha = 234.766°$ are compared. Averaging of high density oscillations due to the finite monochromator bandwidth is visible as oscillation attenuation at higher frequencies.

Figure 3 demonstrates the fit stability. The Mueller matrices for arbitrary azimuthal rotation angle with a step of 5° were fitted separately with arbitrary initial parameters, where the monochromator bandwidth, the azimuthal angle, and the thickness are fitted together. Figure 3(a) demonstrates the thickness stability with accuracy better than one-tenth of a micrometer, which is less than

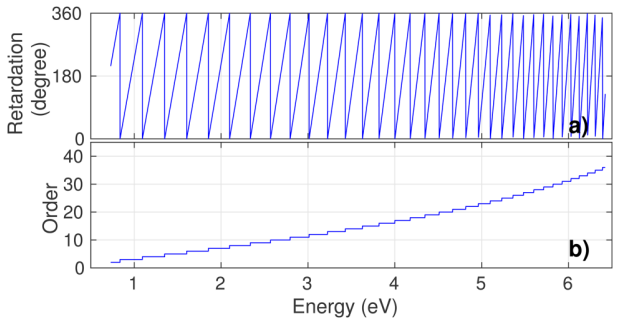

FIG. 2. Retardation of the high-order waveplate is plotted in (a). The dispersion of quartz causes increasing density of oscillations. Subplot (b) shows corresponding wavelength dependence of the waveplate order.

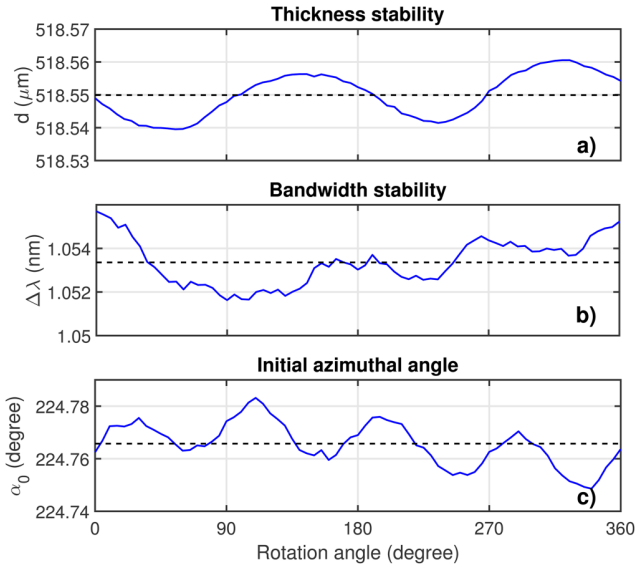

FIG. 3. Fit stability of achieved thickness (a), monochromator bandwidth (b), and initial azimuthal angle (c) for each waveplate rotation is demonstrated.

the common mechanical methods to determine the thickness. Figure 3(b) shows fitted values of the monochromator bandwidth, with respect to the azimuthal angle rotation, determined with precision less than one hundredth of a nanometer. This well established parameter can be used to model data affected by the depolarization influence. Figure 3(c) shows the initial azimuthal angle of waveplates obtained from the fitted waveplate azimuthal angle with subtracted the rotation angle. Despite the fit sensitivity to parameters depending on azimuthal angle of waveplate, we obtain stable and precise solution. Moreover, parameters achieved from full 360° rotation shown above converge to mean values of parameters in the stability test shown in Fig. 3.

IV. LU–CHIPMAN DECOMPOSITION

Another way to process experimental data without necessity to include the finite monochromator bandwidth is the application of the Lu–Chipman product decomposition, which deals with separating the main sample polarization effects accursed into the confused entirety of particular Mueller matrix. Each Mueller matrix contains information about its depolarizing properties $\mathbf{M}_\Delta$, diattenuation effects (dependence of transmission upon the incident polarization state) $\mathbf{M}_\mathrm{D}$, and the retardation properties of the sample $\mathbf{M}_\mathrm{R}$. Lu and Chipman have addressed[16,17] that, for an arbitrary Mueller matrix, there exists an equivalent product of another three Mueller matrices, each describing one of the mentioned properties,

$$\mathbf{M} = \mathbf{M}_\Delta \mathbf{M}_\mathrm{R} \mathbf{M}_\mathrm{D}. \tag{5}$$

The retardation matrix $\mathbf{M_R}$ obtained directly from the measured Mueller matrix of the high-order waveplate is purified from depolarization caused by the finite monochromator bandwidth. Figure 4 compares the retardation matrix $\mathbf{M}_\mathrm{R}$ of data shown in Fig. 1 with the model based on (1) and fitted with values $d = 518.63\,\mu$m and $\alpha_0 = 224.764°$, which agree well with previous results. Figure 4 shows components of the retardation matrix obtained by using (5) from Lu–Chipman decomposition. In general, the Mueller matrix of a linear retarder shows symmetry $M_{R23} = M_{R32}$ [see Eq. (1)]; however, for a circular retarder, it exhibits symmetry $M_{R23} = -M_{R32}$. In a case of the general retarder, the matrix is not symmetric in these elements. The matrix of our case ($M_{R23} \approx M_{R32}$) is close to a linear retarder as expected.

Figure 5(a) shows the M_{R32} (depolarization-free) elements of the retardation Mueller matrix obtained from (5) upon particular azimuthal rotations $\alpha = -0.7°$, $0.0°$, and $+0.7°$. For these cases, spectral oscillations are present, which are caused by the linear birefringence $n_e - n_o$ [see Eq. (1)] of the waveplate. In the case of the ideal linear retarder, the element M_{R23} corresponding to the waveplate with the optical axis aligned vertically ($\alpha = 0.0°$) should remain zero over the whole spectral range; however, minor

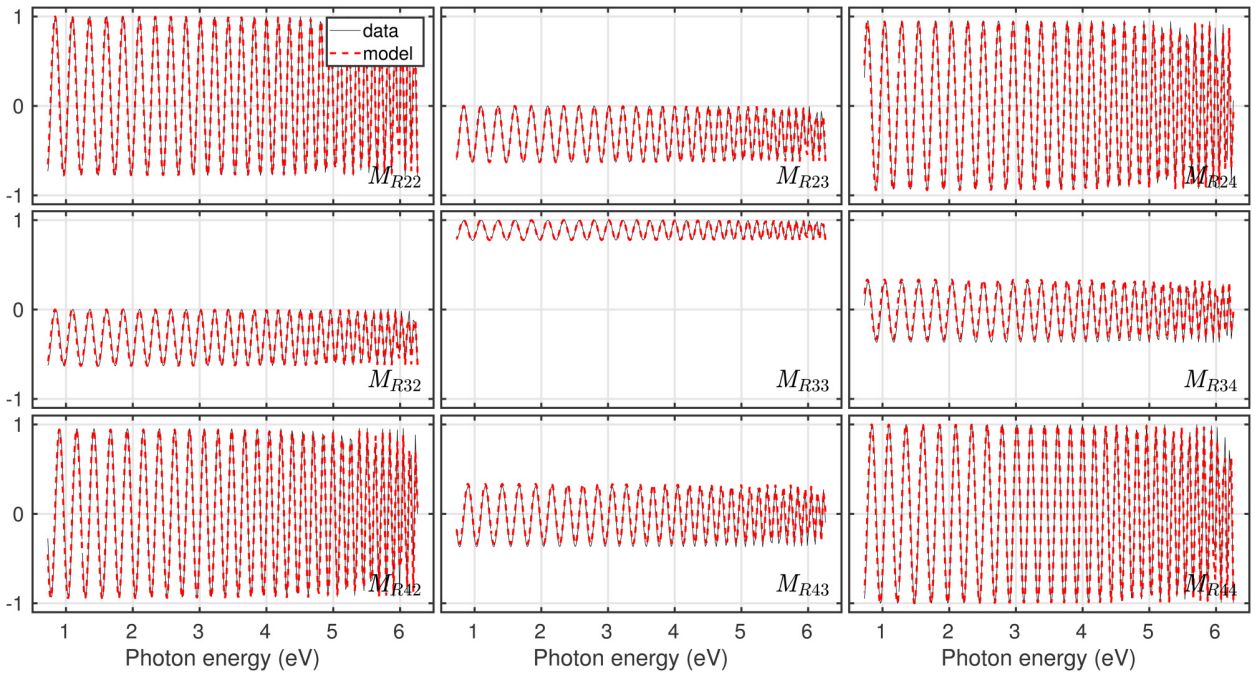

FIG. 4. Retardation Mueller matrix compounds (black curves) obtained using Lu–Chipman decomposition are compared with a single waveplate model (red dashed curves) introduced in (1).

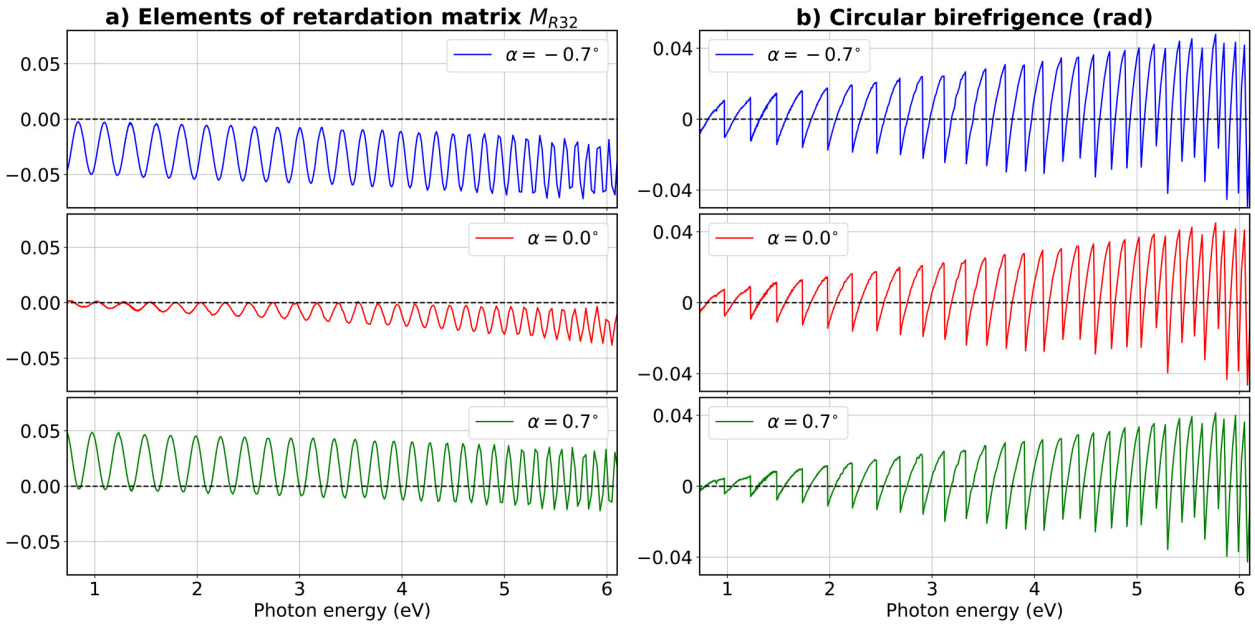

FIG. 5. Oscillations in M_{R32} general retardation matrix element (obtained using Lu–Chipman decomposition) are shown in (a). Subplot (b) describes corresponding nonzero circular birefringence obtained using (6) to the fact that the optical activity of the quartz waveplate is present.

oscillations are present. These oscillations could be explained with the optical activity phenomenon sufficiently. To exclude the effects of the waveplate misalignment or miscut, circular birefringence (CB) corresponding to each sample azimuthal rotation was calculated[18] using the formula

$$\mathrm{CB} = \frac{R}{2\sin R}(M_{R_{23}} - M_{R_{32}}), \tag{6}$$

where

$$R = \arccos\left[\frac{\mathrm{tr}(\mathbf{M_R})}{2} - 1\right], \tag{7}$$

and is shown in Fig. 5(b). For each azimuthal rotation, the CB exhibits the same spectral dependence, as the optical activity is affected by the thickness of the waveplate only. Note that a miscut or misalignment error would cause oscillations, which would change its amplitude as a function of the rotation angle α, and its effect would not be observed in CB. Further investigation of the optical activity effects will be the focus of our subsequent research.[19]

V. CONCLUSION

In summary, we studied waveplates using spectral Mueller matrix ellipsometry in the wide spectral range from 193 to 1700 nm. The measurements of single high-order waveplates affected by depolarization originating from the finite monochromator bandwidth have been shown. This depolarization influence was included in theoretical description in the form of incoherent summation of Mueller matrices. The Lu–Chipman decomposition of the experimental Mueller matrix was performed to eliminate the depolarization effects directly from the measured data. In this case, when $\alpha \approx 0°$, the measurement high sensitivity allows us to observe the second-order fine oscillations within particular Mueller matrix elements. These effects were explained with the optical activity phenomenon. Moreover, we have demonstrated the stability of the method to fit measured data for the arbitrary angle position. It was shown that the thickness, monochromator bandwidth, and azimuthal angle were determined with high precision.

ACKNOWLEDGMENTS

Partial support from the Czech Science Foundation (Project No. 18-22102S), SP2019/92 project, CZ 02.1.01/0.0/0.0/16013/0001791, EEA Grant (No. EHP-CZ-ICP-1-013), the Czech-French Mobility project (No. 8J19FR006), and the Scholarship of the City of Ostrava are acknowledged.

REFERENCES

[1]D. Aspnes, Thin Solid Films **571**, 334 (2014).
[2]E. Garcia-Caurel, R. Ossikovski, M. Foldyna, A. Pierangelo, B. Drvillon, and A. D. Martino, "Advanced mueller ellipsometry instrumentation and data analysis," in *Ellipsometry at the Nanoscale* (Springer, Berlin, 2013), pp. 31–143. doi:10.1007/978-3-642-33956-1_2
[3]H. Fujiwara, *Spectroscopic Ellipsometry: Principles and Applications*, 1st ed. (Wiley, New York, 2007).

[4]R. M. A. Azzam and N. M. Bashara, Ellipsometry and Polarized Light (North-Holland, Amsterdam, 1977).
[5]R. C. Jones, J. Opt. Soc. Am. **31**, 488 (1941).
[6]H. Hurwitz and R. C. Jones, J. Opt. Soc. Am. **31**, 493 (1941).
[7]H. Gu, X. Chen, C. Zhang, H. Jiang, and S. Liu, J. Opt. **20**, 015401 (2017).
[8]K. Postava, R. Sýkora, D. Legut, and J. Pištora, Proc. Mater. Sci. **12**, 118 (2016).
[9]L. Halagačka, K. Postava, and J. Pištora, Proc. Mater. Sci. **12**, 112 (2016).
[10]J. J. Gil Pérez and R. Ossikovski, *Polarized Light and the Mueller Matrix Approach*, Series in Optics and Optoelectronics (CRC, Boca Raton, 2016), p. 21.
[11]T. Radhakrishnan, Proc. Math. Sci. **33**, 22 (1951).
[12]T. Radhakrishnan, Proc. Math. Sci. **25**, 260 (1947).
[13]S.-M. F. Nee, J. Opt. Soc. Am. A **17**, 2067 (2000).
[14]W. Li, C. Zhang, H. Jiang, X. Chen, and S. Liu, J. Opt. **18**, 055701 (2016).
[15]T. A. Germer and H. J. Patrick, "Effect of bandwidth and numerical aperture in optical scatterometry," in *Metrology, Inspection, and Process Control for Microlithography XXIV*, edited by C. J. Raymond (SPIE, Bellingham, 2010). doi:10.1117/12.846776.
[16]S.-Y. Lu and R. A. Chipman, J. Opt. Soc. Am. A **13**, 1106 (1996).
[17]R. Ossikovski, M. Anastasiadou, S. B. Hatit, E. Garcia-Caurel, and A. D. Martino, Phys. Status Solidi (a) **205**, 720 (2008).
[18]O. Arteaga, "Mueller matrix polarimetry of anisotropic chiralmedia," Ph.D. thesis (School Universitat de Barcelona, 2010).
[19]D. Vala, P. Koleják, K. Postava, P. Provazníková, and J. Pištora, "Effects of optical activity to Mueller matrix ellipsometry of composed waveplates," Opt. Mater. Express (submitted).

References

[1] Garcia-Caurel, E., R. Ossikovski, M. Foldyna, A. Perangelo, B. Drévillon, and A. de Martino. *Advanced Mueller Ellipsometry Instrumentation and Data Analysis.* Losurdo, M., and K. Hingerl, ed. *Ellipsometry at the Nanoscale.* Berlin, Heidelberg: Springer Berlin Heidelberg, 2013, pp. 31–143, ISBN: 978-3-642-33955-4,

[2] Azzam, R. M. A., and N. M. Bashara. *Ellipsometry and polarized light.* New York: sole distributors for the USA and Canada, Elsevier North-Holland, 1977. ISBN: 978-0-720-40694-8,

[3] Halagačka, L., K. Postava, and J. Pištora. *Analysis and Modeling of Depolarization Effects in Mueller Matrix Spectroscopic Ellipsometry Data.* Proc. Mat. Sci. 2016, vol. 12, pp. 112–117,

[4] Jellison, G. E., L. A. Boatner, J. D. Budai, B.-S. Jeong, and D. P. Norto. *Spectroscopic ellipsometry of thin film and bulk anatase (TiO_2).* J. Appl. Phys. 2003, vol. 93(12), pp. 9537–9541,

[5] Postava, K., R. Sýkora, D. Legut, and J. Pištora. *Determination of Anisotropic Crystal Optical Properties Using Mueller Matrix Spectroscopic Ellipsometry.* Proc. Mat. Sci. 2016, vol. 12, pp. 118–123,

[6] Svensen, Ø., J. J. Stamnes, M. Kildemo, L. M. S. Aas, S. R. Erga, and Ø. Frette1. *Mueller matrix measurements of algae with different shape and size distributions.* App. Opt. 2011, vol. 50(26), pp. 5149–5157,

[7] Novikova, T., J. Rehbinder, S. Deby, H. Haddad, J. Vizet, A. Pierangelo, P. Validire, A. Benali, B. Gayet, B. Teig, A. Nazac, B. Drévillon, F. Moreau, and A. De Martino. *Multispectral Mueller Matrix Imaging Polarimetry for Studies of Human Tissue.* Elsevier, 2016,

[8] Dong, Y., J. Qi, H. He, Ch. He, S. Liu, J. Wu, D. S. Elson, and H. Ma. *Quantitatively characterizing the microstructural features of breast ductal carcinoma tissues in different progression stages by Mueller matrix microscope.* Biomed. Opt. Express. 2017, vol. 8(8), pp. 3643–3655,

[9] Rehbindera, J., S. Deby, H. Haddad, B. Teig, A. Nazac, A. Pierangelo, and F. Moreau. *Diagnosis of uterine cervix cancer using Müller polarimetry: a comparison with histopathology.* N. Biophot. Tech. App. III. 2015, SPIE-OSA conf. paper,

[10] Franks, M. E., G. R. Macpherson, and W. D. Figg. *Thalidomide.*, Lancet., vol. 363(9423), 2004, pp. 1802–1811,

[11] Toxvaerd, S. *Origin of Homochirality in Biosystems.* Int. J. Mol. Sci., vol. 10(3), 2009, pp. 1290–1299,

[12] Li, S., M. Wei, X. Feng, Q. Wang, Q. Xu, Y. Xu, L. Liu, Ch. Ouyang, W. Zhang, C. Hu, X. Zhang, J. Han, and W. Thang. *Polarization-insensitive tunable terahertz polarization rotator.* Opt. Express, vol. 27(12), 2019, pp. 16966–16974,

[13] Griffiths, D. J. *Introduction to Electrodynamics.* 4th ed., Pearson, 2013, ISBN: 978-0-321-85656-2,

[14] Halliday, D., R. Resnick, and J. Walker, Dub, P. (editor), *Fyzika 2. (Physics 2.)*, reworked ed. Translation: M. Černý. Brno: VUTIUM, 2013. University textbooks translations. ISBN 978-80-214-4123-1,

[15] Saleh, B. E. A., and M. C. Teich. Fundamentals of photonics. 2nd ed. Hoboken, N.J.: Wiley Interscience, 2007. ISBN: 978-0-471-35832-9,

[16] Jones, R. C. *A new calculus for the treatment of optical systems, I. Description and Discussion of the Calculus.* J. Opt. Soc. Am., vol. 31(7), 1941, pp. 488–493,

[17] Stokes, G. G. *On the composition and resolution of streams of polarized light from different sources.* Trans. Cambridge Phil. Soc., vol. 9(399), 1852, pp. 234–258,

[18] Peřina, J. *Coherence of Light.*, 2nd extended ed., D. Reidel, Dordrecht, Boston: 1985, ISBN: 978-90-277-2004-7,

[19] Müller, H. *Memorandum on the polarization optics of the photo-elastic Shutter.* OSRD Project OEMsr-576, Report No. 2, 1943,

[20] Arteaga, O. *Historical revision of the differential Stokes–Mueller formalism: discussion.* J. Opt. Soc. Am. A, vol. 34, 2017, pp. 410–414,

[21] Chipman, R. A. *Depolarization index and the average degree ofpolarization.* App. Opt. vol. 44(13), 2005, pp. 2490–2495,

[22] Gil Pérez, J. J., and E. Bernabeu. *A depolarization criterion in Mueller matrices.* Optica Acta, vol. 32(3), 1985, pp. 259–261,

[23] Cloude, S. R., *Group theory and polarisation algebra.* Optik (Stuttgart). 1986, vol. 75, pp. 26–36,

[24] Gryga, M., D. Vala, P. Koleják, L. Gembalová, D. Ciprian, and P. Hlubina. *One-dimensional photonic crystal for Bloch surface waves and radiation modes-based sensing.* Opt. Mat. Express, vol. 9, 2019, pp. 4009–4022,

[25] Arteaga, O. *Mueller matrix polarimetry of anisotropic chiral media.*, Ph.D. thesis, Universitat de Barcelona, 2010,

[26] Le Roy-Bréhonnet, F., and B. Le Jeune. *Utilization of Mueller matrix formalism to obtain optical targets depolarization and polarizatuon properties.* Prog. Quantum Electron., vol. 21, 1997, pp. 109–151,

[27] Lu, S-Y., and R. A. Chipman. *Interpretation of Mueller matrices based on polar decomposition.* J. Opt. Soc. Am. A, vol. 13(5), 1996, pp. 1106–1113,

[28] Ossikovski, R., J. J. Gil, and I. San José. *Poincaré sphere mapping by Mueller matrices.* J. Opt. Soc. Am. A, vol. 26, 2013, pp. 2291–2305,

[29] Ossikovski, R., A. de Martino, and S. Guyot. 2007. *Forward and reverse product decompositions of depolarizing Mueller matrices.* Optics Letters, vol. 32(6), 2007, pp. 689–691,

[30] Anastasiadou, M., S. B. Hatit, R. Ossikovski, S. Guyot, and A. de Martino. *Experimental validation of the reverse polar decomposition of depolarizing Mueller matrices.* J. Europ. Opt. Soc. – Rap. Pub., vol. 2, 2007, pp. 7018(1)–7018(7),

[31] Ossikovski, R. *Analysis of depolarizing Mueller matrices through a symmetric decomposition.* J. Opt. Soc. Am. A, vol. 26(5), 2009, pp. 1109–1118,

[32] Ossikovski, R. *Differential matrix formalism for depolarizing anisotropic media.* Optics Letters, vol. 36(12), 2011, pp. 2330–2332,

[33] Ossikovski, R., M. A. Kuntman, and O. Arteaga. *Anisotropic integral decomposition of depolarizing Mueller matrices.* OSA Continuum, vol. 2(6), 2019, pp. 1900–1907,

[34] Gil Pérez, J. J., and R. Ossikovski. *Polarized light and the Mueller matrix approach.*, Series in Optics and Optoelectronics, CRC Press, 2016, ISBN: 978-1-4822-5156-2,

[35] Rehbinder, J., H. Haddad, S. Deby, B. Teig, A. Nazac, T. Novikova, A. Pierangelo, and F. Moreau. *Ex vivo Mueller polarimetric imaging of the uterine cervix: A first statistical evaluation.* J. Biomed. Opt., vol. 21(7), 2016, pp. 2291–2305,

[36] Antonelli, M. R., A. Pierangelo, T. Novikova, P. Validire, A. Benali, B. Gayet, and A. De Martino. *Mueller matrix imaging of human colon tissue for cancer diagnostics: how Monte Carlo modeling can help in the interpretation of experimental data.* Optics Express. vol. 18(10), 2010, pp. 10200–10208,

[37] Antonelli, M. R., A. Pierangelo, T. Novikova, P. Validire, A. Benali, B. Gayet, and A. De Martino. *Impact of model parameters on Monte Carlo simulations of backscattering Mueller matrix images of colon tissue.* Biomed. Opt. Express. vol. 2(7), 2011, pp. 1836–1851,

[38] Gil Pérez, J. J., and E. Bernabeu. *Depolarization and polarization indices of an optical system.* Optica Acta, vol. 33(2), 1986, pp. 185–189,

[39] Gil Pérez, J. J. *Components of purity of a Mueller matrix.* J. Opt. Soc. Am. A, vol. 28(8), 2011, pp. 1578–1585,

[40] Foldyna, M., A. de Martino, R. Ossikovski, E. Garcia-Caurel, and C. Licitra. *Characterization of grating structures by Mueller polarimetry in presence of strong depolarization due to finite spot size and spectral resolution.* Opt. Commun. vol. 282, 2009, pp. 735–741,

[41] Fujiwara, H. *Spectroscopic ellipsometry: principles and applications.* Hoboken, NJ: John Wiley, 2007. ISBN: 978-0-470-06018-6,

[42] Wald, G. *The origin of optical activity.* Ann. NY Acad. Sci., vol. 69(2), 1957, pp. 352–368,

[43] Biot, J. B. *Phenomene de polarisation successive, observés dans des fluides homogenes. (Phenomenon of successive polarization, observed in homogeneous fluids).* Bulletin des Sci., 1815, pp. 190–192, [in french],

[44] Biot, J. B. *Molecular rotatory power.* Mém. Acad. Sci., vol. 15, 1836, pp. 93–279,

[45] Pasteur, L. *Recherches sur les relations qui peuvent exister entre la forme cristalline, la composition chimique et le sens de la polarisation rotatoire. (Research on the relations which can exist between the crystalline form, the chemical composition and the direction of the rotatory polarization).* Ann. Chim. Phys., vol. 3(24), 1848, pp. 442–459,

[46] IUPAC: International Union of Pure and Applied Chemistry: *Compendium of Chemical Terminology: Gold Book.* version 2.3.3 from 2014-04-24, cited 2020-04-01. Accesible from: https://goldbook.iupac.org/files/pdf/goldbook.pdf,

[47] Lowry, T. M. *Optical Rotatory Power.* Dover Publications: 1964. Reprinted ed. of: Longmans, Green and Co., London, 1935. ISBN: 9780486611976,

[48] Kim, J. H., and A. R. Scialli. *Thalidomide: the tragedy of birth defects and the effective treatment of disease.* Toxic. Sci., vol. 122(1), 2011, pp. 1–6,

[49] Mellin, G. W., and M. Katzenstein. *The saga of thalidomide: neuropathy to embryopathy, with case reports of congenital anomalies.* N. Engl. J. Med., vol. 267, 1962, pp. 1184–1192,

[50] Calabrese, L., and A. B. Fleischer. *Thalidomide: current and potential clinical applications.* Am. J. Med., vol. 108, 2000, pp. 487–495,

[51] Le Bel, J. A. *Sur les relations qui existent entre les formules atomiques des corps organiques et le pouvoir rotatoire de leurs dissolutions (On the relations which exist between the atomic formulas of organic compounds and the rotatory power of their solutions).* Bull. Soc. Chim. Fr. vol. 2(22), 1874, pp. 337–347,

[52] van't Hoff, J. H. *La chimie dans l'éspace. (Chemistry in space.)* Bazendijk: Rotterdam, 1875,

[53] Dodziuk, H. *Strained Hydrocarbons: Beyond the van't Hoff and Le Bel Hypothesis.* Wiley-VCH Verlag GmbH & Co. KGaA: 2008, ISBN: 978-3-527-31767-7,

[54] Fisher, E. *Berichte der deutschen chemischen Gesellschaft. (About the configuration of dextrose and its isomers).* vol. 24(1), Ber. dtsch. chem. Gesellschaft, 1891, pp. 2683–2687,

[55] Bentley, R. *Are Fischer Projection Formulas Really Necessary?* Biochem. Educ., vol. 25(4), 1997, pp. 216–220,

[56] Ernest, Z. *Introduction to Chirality and Chiral Centers.* SOCRATIC. Cupertino, CA: Apple Inc., 2014. URL: https://socratic.org/organic-chemistry-1/r-and-sconfigurations/introduction-to-chirality-and-chiral-centers,

[57] Cahn, R. S., C. K. Ingold, and V. Prelog. *Specification of Molecular Chirality.* Angewandte Chem. Int. Ed., vol. 5, 1966, pp. 385–415,

[58] *Orders of protein structure.* Khan Academy, 2020. URL: https://www.khanacademy.org/science/biology/macromolecules/proteins-and-amino-acids/a/orders-of-protein-structure,

[59] Chen, Y.-H., J. T. Yang, and H. M. Martinez. *Determination of the secondary structures of proteins by circular dichroism and optical rotatory dispersion.* Biochemistry, vol. 11(22), 1972, pp. 4120–4131,

[60] *DNA structure and function.* Khan Academy. URL: https://www.khanacademy.org/test-prep/mcat/biomolecules/dna/a/dna-structure-and-function,

[61] Mason, S. *Biomolecular homochirality.* Chem. Soc. Rev. vol. 17, 1988, pp. 347–359,

[62] Kojo, S. *Origin of Homochirality of Amino Acids in the Biosphere.* Symmetry. vol. 2, 2010, pp. 1022–1032,

[63] Inoue, Y. *Asymmetric Photochemical Reactions in Solution.* Chem. Rev. vol. 92, 1992, pp. 741–770,

[64] Bailey, J., A. Chrysostomou, J. H. Hough, T. M. Gledhill, A. McCall, S. Clark, F. Ménard, and M. Tamura. *Circular Polarization in Star- Formation Regions: Implications for Biomolecular Homochirality.* Science. vol. 281, 1998, pp. 672–674,

[65] Avalos, M., R. Babiano, P. Cintas, J. L. Jiménez, and J. C. Palacios. *Absolute Asymmetric Synthesis under Physical Fields: Facts and Fiction.* Chem. Rev. vol. 98(7), 1998, pp. 2391–2404,

[66] Pavlov, V. A., and E. I. Klabunovskii. *Homochirality Origin in Nature: Possible Versions.* Current Org. Chem. vol. 18, 2014, pp. 93–114,

[67] Konstantinova, A. F., T. G. Golovina, and K. K. Konstantinov. *Manifestation of Optical Activity in Different Materials.* Crystallograph. Rep. vol. 59(4), 2014, pp. 447–465,

[68] von Lang, V. *Zur Theorie der Circularpolarisation. (Theory of circular polarization.)* Pogg. Ann. Phys. Chem., vol. 119, 1863, p. 74,

[69] Drude, P. *The Theory of Optics.* Transl.: Mann, C. R., and R. A. Millikan. Dover Publications, Inc., New York, 1959 (ref. on page 413),

[70] Moffitt, W., and Yang, J. T. *The Optical Rotatory Dispersion of Simple Polypeptides. I.* Proc. N. A. S. vol. 42(9), 1956, pp. 596–603,

[71] Jirgensons, B. *Optical Activity of Proteins and Other Macromolecules.* 2nd ed. Springer-Verlag, New York, 1973, ISBN: 978-3-642-87713-1,

[72] Parchaňský, V., J. Kapitán, and P. Bouř. *Inspecting chiral molecules by Raman optical activity spectroscopy.* RSC Adv. vol. 4, 2014, pp. 57125–57136,

[73] Kapitán, J., V. Baumruk, and P. Bouř. *Demonstration of the Ring Conformation in Polyproline by theRaman Optical Activity.* J. Am. Chem. Soc. vol. 128, 2006, pp. 2438–2443,

[74] Kapitán, J., F. Zhu, L. Hecht, J. Gardiner, D. Seebach, and L. D. Barron. *Solution Structures of β Peptides from Raman Optical Activity.* Ang. Chem. vol. 11, 2008, pp. 6392–6394,

[75] Wu, T., J. Kapitán, V. Mašek, and P. Bouř. *Detection of Circularly Polarized Luminescence of a Cs-Eu^{III} Complex in Raman Optical Activity Experiments.* Ang. Chem. vol. 54(49), 2014, pp. 14933–14936,

[76] Nafie, L. W. *Vibrational Optical Activity: Principles and Applications.* John Wiley, 2011, ISBN: 978-0-470-03248-0,

[77] Barron, L. D. *Molecular Light Scattering and Optical Activity.* Cambridge University Press: New York, 2004. ISBN: 978-0-511-23121-6,

[78] Zhang X.-C., and J. Xu, *Introduction to THz wave photonics.* Springer: New York, 2010,

[79] Miles, R. *Terahertz frequency detection and identification of materials and objects.*, 1. Ed. Springer: Dordrecht, 2007. ISBN: 978-1-402-06502-6,

[80] Chan, W. L., J. Deibel, and D. M. Mittleman, *Imaging with terahertz radiation*, Rep. Prog. Phys. vol. 70(8), 2007, pp. 1325–1379,

[81] Diels, J.-C., and W. Rudolph. *Ultrashort laser pulse phenomena, Fundamentals, techniques, and applications on a femtosecond time scale.* 2nd Ed. Academic Press: Boston, 2006,

[82] Kenanakis, G., E. N. Economou, C. M. Soukoulis, and M. Kafesaki. *Controlling THz and far-IR waves with chiral and bianisotropic metamaterials.* EPJ Appl. Metamat. vol. 2(15), 2015, pp. 1–12,

[83] Veselago, V. G. *The electrodynamics of substances with simultaneously negative values of ε and μ.* Sov. Phys. Usp. vol. 10, 1968, pp. 509–514,

[84] Boardman, A. *Pioneers in metamaterials: John Pendry and Victor Veselago.* J. Opt. vol. 13(2), 2011, pp. 1–6,

[85] Choi, W. J., G. Cheng, Z. Huang, S. Zhang, T. B. Norris, and N. A. Kotov. *Terahertz circular dichroism spectroscopy of biomaterials enabled by kirigami polarization modulators.* Nature Materials. vol. 18, 2019, pp. 820–826

[86] Liu, X., S. MacNaughton, D. B. Shrekenhamer, H. Tao, and S. Selvarasah. *Metamaterials on parylene thin film substrates: Design, fabrication, and characterization at terahertz frequency.* App. Phys. Letters. vol. 96, 2010,

[87] Masyukov, M., A. V. Vozianova, A. Grebenchukov, K. Gubaidullina, A. Zaitsev, and M. Khodzitsky. *Optically tunable terahertz chiral metasurface based on multi-layered graphene.* Sci. Rep. vol. 10(3157), 2020, pp. 1–10,

[88] Masyukov, M., A. V. Vozianova, K. V. Gubaidullina, A. N. Grebenchukov, and M. K. Khodzitsky. *Optical Activity of Graphene-Based Chiral Metasurface in THz Frequency Range.* IEEE Explore. 2019,

[89] Minerbi, E., S. Keren-Zur, and T. Ellenbogen. *Nonlinear Metasurface Fresnel Zone Plates for Terahertz Generation and Manipulation.* Nano Lett. vol. 19, 2019, pp. 6072–6077,

[90] Cole, M. A., W. Chen, M. Liu, S. S. Kruk, W. J. Padilla, I. V. Shadrivov, and D. A. Powell. *Strong Broadband Terahertz Optical Activity through Control of the Blaschke Phase with Chiral Metasurfaces.* Phys. Rev. App. vol. 8, 2017,

[91] Lindell, I. V., A. H. Sihvola, S. A. Tretyakov, and A. J. Viitanen. *Electromagnetic Waves in Chiral and Bi-Isotropic Media.* Artech House: Boston, London. 1994. ISBN: 0-89006-684-1

[92] Landau, L. D., and E. M. Lifshitz. *Course of Theoretical Physics, Vol. 8: Electrodynamics of Continuous Media.* Pergamon: New York, 1984, ISBN: 978-0-75062-634-7,

[93] Berreman, D. W. *Optics in Stratified and Anisotropic Media:* 4×4*-Matrix formulation.* J. Opt. Soc. Am., vol. 62(4), 1972, pp. 502–510,

[94] Condon, E. U. *Theories of Optical Rotatory Power.* Rev. Mod. Phys. vol. 9, 1937, pp. 432–457,

[95] Федоров, Ф. И. Теория гиротропии. (Fedorov, F. I. *Theory of gyrotropy.*) Минск: Издательство Наука и Техника: 1964,

[96] Tellegen, B. D. H. *The Gyrator: A New Electric Network Element.* Phillips Res. Rept. vol. 3, 1948, pp. 81–101,

[97] Onsager, L. *Reciprocal Relations in Irreversible Processes. I.* Phys. Rev. vol. 37(405), 1931, pp. 2265–2279,

[98] Onsager, L. *Reciprocal Relations in Irreversible Processes. II.* Phys. Rev. vol. 38(405), 1931, pp. 2265–2279,

[99] Hemmer, P. C., H. Holden, and S. K. Ratkje. *The collected works of Lars Onsager.* World Scientific Series in 20th Century Physics. vol. 17, 1996, pp. 10–156,

[100] Casimir, H. B. G. *On Onsager's Principle of Microscopic Reversibility.* Rev. Mod. Phys. vol. 17(343), 1945, pp. 343–350,

[101] Константинова, А. Ф., Б. Н. Гречушников, Б. В. Бокуть, Е. Г. Валяшко. Оптические свойства кристаллов. (Konstantinova, A. F., B. N. Grečušnikov, B. V. Bokuť, E. G. Valjaško. *Optical properties of Crystals.*) Минск: Наука и Техника: 1995,

[102] Barkovsky, L. M., and G. N. Borzdov. *V. A. Shamburov's Validity Criteria for the Gyrotropy Theory.* Phys. Quant. Opt. vol. 95(1), 2005, pp. 131–138,

[103] Ossikovski, R., and O. Arteaga. *Extended Yeh's method for optically active anisotropic layered media.* Optics Letters, vol. 42(18), 2017, pp. 3690–3693,

[104] Zamarský, V., H. Raclavská, and D. Matýsek. *Mineralogie a krystalografie pro FMMI. (Mineralogy and Crystallography for Faculty of Materials, Science and Technology.)* Ostrava, VSB-TUO, 2008. ISBN: 978-80-248-1904-4,

[105] Mirman, R. *Point groups, space groups, crystals, molecules.* London, World SCientific, 1999. ISBN: 978-981-02-3732-5,

[106] Neumann, F. E., and O. E. Meyer (ed.) *Vorlesungen über die Theorie der Elastizität der festen Körper und des Lichtäthers. (Lectures on the Theory of Elasticity of Solids.)* B. G. Teubner-Verlag, Leipzig, 1885,

[107] Nye, J. F. *Physical Properties of Crystals: Their Representation by Tensors and Matrices.* Clarendon Press: Oxford, 1985, ISBN: 0-19-851165-5,

[108] Fumi, F. G. *Physical properties of crystals: the direct-inspection method.* Acta Cryst. vol. 5, 1952, pp. 44–48,

[109] Goldstein, H., Ch. Poole, and J. Safko. *Classical Mechanics.* 3rd Ed. Addison Wesley, 1950. ISBN: 978-0-201-65702-9,

[110] Sihvola, A. H., and I. V. Lindell. *Bi-Isotropic Constitutive Relations.* Mic. Opt. Tech. Letters. vol. 4(8), 1991, pp. 295–297,

[111] Yariv, A., and P. Yeh. *Optical Waves in Crystals: Propagation and Control of Laser Radiation.* John Wiley & Sons: New York, 1984, ISBN: 0-471-09142-1,

[112] Vollhardt, P., and N. Schore. *Organic Chemistry: Structure and Function.* 6th Ed.: W. H. Freeman and Company, New York, 2011. ISBN: 978-1-4292-0494-1,

[113] McMurry, J. *Organic chemistry.* 8th ed., Belmont: Brooks/Cole, 2012. ISBN: 978-0-840-05444-9,

[114] Dubrunfaut, A. P. *Note sur quelques phénomènes rotatoires et sur quelques propriétés des sucres. (Note on some rotatory phenomena and on some properties of sugars.)* Comptes Rendus, vol. 23, 1846, pp. 38–44,

[115] Wlodarczyk, P., K. Kaminski, M. Paluch, and J. Ziolo. *Mutarotation in D-Fructose Melt Monitored by Dielectric Spectroscopy.* J. Phys. Chem. B, vol. 113, 2009, pp. 4379–4383,

[116] Arteaga, O., A. Canillas, and G. E. Jelisson, Jr. *Determination of the components of the gyration tensor of quartz by oblique incidence transmission two-modulator generalized ellipsometry.* App. Opt. vol. 48(28), 2009, pp. 5307–5317,

[117] Arteaga, O. *Mueller matrix polarimetry of anisotropic chiral media.* PhD thesis, Universitat de Barcelona, 2010,

[118] Arteaga, O., J. Freudenthal, and B. Kahr. *Reckoning electromagnetic principles with poalrimetric measurements of anisotropic optically active crystals.* J. App. Crystallography. vol. 45, 2012, pp. 279–291,

[119] Chandrasekhar, S. *Simple model for optical activity.* Am. J. Phys. vol. 24, 1956, pp. 503–506,

[120] Chandrasekhar, S. *Optical Rotatory Dispersion of Crystals.* Proc. Rol. Soc. London, Series A: Mat. Phys. Sci. vol. 259, 1961, pp. 531–553,

[121] Daimon, M., and A. Masumura. *Measurement of the refractive index of distilled water from the near-infrared region to the ultraviolet region.* Appl. Opt. vol. 46, 2007, pp. 3811–3820,

[122] Belay, A. and G. Assefa. *Concentration, Wavelength and Temperature Dependent Refractive Index of Sugar Solutions and Methods of Determination Contents of Sugar in Soft Drink Beverages using Laser Lights.* J. Laser Opt. Photonics. vol. 5(2), 2018,

[123] Rumble, J. R. *CRC Handbook of Chemistry and Physics.* 101st Ed., 2018, ISBN: 978-0-367-41724-6,

[124] Atkins, P. W., and Julio de Paula. *Fyzikální chemie. (Physical Chemistry.)* Praha: Vysoká škola chemicko-technologická v Praze, 2013. ISBN 978-80-7080-830-6,

[125] Brdička, R., M. Kalousek, and A. Schütz. *Úvod do fyzikální chemie. (Introduction to Physical Chemistry.)* 2nd ed., SNTL: ALFA n. p. Bratislava, 1972,

[126] Belitz, H. D., W. Grosch, and P. Schieberle. *Food Chemistry.* 4th Ed. Springer, 2009. ISBN: 978-3-540-69933-0,

[127] Vala, D., M. Mičica, K. Postava, and J. Pištora. *Optical activity temperature-dependent measurements of chiral solutions using Mueller matrix spectroscopic ellipsometry.* Proc. SPIE 10976, 21st Czech-Polish-Slovak Optical Conference on Wave and Quantum Aspects of Contemporary Optics, 2018,

[128] J.A. Woollam Co., Inc. *CompleteEASE Software Manual.* Lincoln, NE, 2011,

[129] Lin, Ch.-E., Ch.-J. Yu, Ch.-L. Chen, L.-D. Chou, and Ch. Chou. *Kinetics of Glucose Mutarotation Assesed by an Equal-Amplitude Paired Polarized Heterodyne Polarimeter.* J. Phys. Chem. A. vol. 114, 2010, pp. 1665–1669,

[130] Kendrew, J. C., and E. A. Moelwyn-Hughes. *The Kinetics of Mutarotation in Solution.* Proc. Rol. Soc. London, Series A. vol. 176(966), 1940, pp. 352–367,

[131] Koleják, P., D. Vala, K. Postava, P. Provazníková, and J. Pišotra. *Mueller matrix ellipsometry of waveplates for control of their properties and alignment.*, J. Vac. Sci. Technol. B. vol. 38(1), 2020.